The fatigue characteristics of SUH660 steel in air and hydrogen gaseous environment

呉, 昊

https://doi.org/10.15017/1441227

出版情報：九州大学, 2013, 博士（工学）, 課程博士
バージョン：
権利関係：全文ファイル公表済

The fatigue characteristics of SUH660 steel in air and hydrogen gaseous environment

Hao WU

The fatigue characteristics of SUH660 steel in air and hydrogen gaseous environment

January 2014

By

Hao WU

Submitted to Faculty of Engineering

Graduate School, Kyushu University, Japan

For the Degree of Doctor of Philosophy

TABLE OF CONTENTS

CHAPTER 1 GENERAL INTRODUCTION

1.1 Background of this study

In recent years, because of continuous increment in global warming and other environmental issues, hydrogen-based energy systems may play a more important role in the future [1], and more and more researches have been conducted for hydrogen fuel cells [2−5]. As hydrogen vessels of hydrogen fuel cells, the characteristics of the resistances to high temperature, high pressure and hydrogen embrittlement are required. SUH660 (A286) steel as an austenitic precipitation-hardened heat-resistant stainless steel with high strength and excellent hydrogen embrittlement resistance [6], is a candidate material for equipment exposed to high-pressure hydrogen, such as hydrogen vessels.

Many researches regarding the fatigue strength characteristics and fatigue crack propagation have been conducted for SUH660 steel in air and hydrogen gas environments [7−10]. Coffin et al. [7] reported that SUH660 steel that underwent planar slip also underwent crack nucleation owing to slip band extrusion in room-temperature air, a room-temperature vacuum, and a high-temperature vacuum. Kobayashi et al. [8] reported that the high-cycle fatigue strength of SUH660 steel depended on its austenitic grain size and tensile strength, which is because the high-cycle fatigue strength depends on the facet size of the crystallographic features in the crack initiation area on the fracture surface. Kubota et al. [9] reported that, in the hydrogen gas environment, the fretting fatigue limit of SUH660 steel decreased in the hydrogen gas when compared to that in air. Nakamura et al. [10] reported that the grains of SUH660 steel can localize slip, thus causing secondary cracking across the main slip. Furthermore, the η-phase (Ni_3Ti) is precipitated along the grain boundaries, resulting in intergranular fatigue degradation. However, as one of the most important characteristics of the fatigue strength, the fatigue limit of SUH660 steel has not been investigated.

Many researchers [11−15] used the two following empirical equations to predict the fatigue limit of the metal by hardness and tensile strength:

$$\sigma_{w0} \approx 1.6HV \pm 0.1HV \quad (1)$$

$$\sigma_{w0} \approx 0.5\sigma_U \quad (2)$$

where σ_{w0} (MPa) is the fatigue limit, σ_U (MPa) is the ultimate tensile strength, and HV (kgf/mm^2) is the Vickers hardness. Moreover, Murakami et al. [15, 16] proposed the following equation to predict the fatigue limit of metal that has a defect:

$$\sigma_w = \frac{1.43(HV + 120)}{(\sqrt{area})^{1/6}} \quad (3)$$

where $\sqrt{area}$ (μm) is the square root of the defect area projected onto the plane perpendicular to the first principal stress. In the three equations, the equation (3) is well suited for the general steel such as carbon steel, but three equations have a large deviation in the predicted results for stainless steel [15]. In other words, the three equations cannot be directly used for fatigue limit prediction of SUH660 steel.

Pre-strain treatment as a method to enhance its strength and fatigue life has been commonly used in the machinery manufacturing industry sector. In the pressure vessels making, autofrettage treatment also be used to enhance its pressure fatigue life [17]. Many researches [18−20] indicated that the beneficial effect of work hardening on fatigue life and fatigue limit for general steel (such as carbon steel). However, for aluminum alloys those are precipitation-strengthened, such as the 6xxx and 7xxx series, the results of the fatigue life reduction with the level of pre-strain were reported [21, 22]. Ikematsu et al. [22] believed that this phenomenon is related to precipitate cutting; for the precipitation-strengthened 6061-T6 aluminum alloy, precipitate cutting due to pre-strain reduces the slip resistance of slip band, and accelerates Mode II crack growth rate because of Mode II crack propagation along slip bands. Therefore, SUH660 steel as an iron-based precipitation-strengthened

alloy which is strengthened by the precipitated γ'-phase (Ni_3 (Al, Ti)) [23, 24], when used for hydrogen vessels making, pre-strain treatment is not necessarily increase its fatigue strength.

Several researches [10, 25] were conducted about the effect of hydrogen on the fatigue life of SUH660 steel. Nakamura et al. [10] used the pre-cracked and smooth specimens to clarify the changes in fatigue life of 10^5 cycles in high pressure gaseous hydrogen environment. Shishime et al. [25] took the fatigue life of 10^6 cycles as the fatigue limit to investigate the hydrogen influence on the fatigue life and threshold of crack growth. However, the effect of hydrogen on fatigue life at the fatigue strength over 10^7 cycles has not been evaluated. This is not conducive to use of SUH660 steel for the long-term reliability in high-pressure hydrogen gaseous environment.

1.2 Purpose of this study

In this paper, the crack propagation behavior was focused to investigate the fatigue limit of SUH660 steel in air environment. And the method of fatigue limit prediction is evaluated according to its fundamental fatigue characteristics. Based on work hardening and precipitate cutting, the effect of pre-strain treatment on the fatigue life is explored. For the long-term reliability in high-pressure hydrogen environment, the effect of hydrogen on the change trend of fatigue life at the fatigue strength over 10^7 cycles is discussed.

1.3 Outline of this study

This paper is composed of 4 chapters. In chapter 1, the background and outline of this study are described.

Chapter 2 is divided into three parts to describe the fundamental fatigue characteristics of SUH660 steel in air environment.

In chapter 2.1, the crack propagation properties were clarified using the plain specimen and the specimen with artificial hole. According to the crack re-propagation behavior at the fatigue strength at 10^7 cycles, an *S*-*N* diagram with two 'fatigue limits' was proposed for SUH660 steel.

In chapter 2.2, a large hardness variation was clarified by Vickers hardness (*HV*) test in multiple zones. A method of obtaining the hardness distribution by using the *HV* distributions of multiple zones is proposed to predict the mean *HV* value of the softest zone for fatigue strength prediction.

In chapter 2.3, the fatigue test was conducted using the pre-strained and buff-polished specimens to clarify the effect of precipitate cutting on crack propagation. And based on the results, a dislocation accumulation model for the fatigue crack tip in the precipitation-strengthened material was proposed.

In chapter 3, the fatigue characteristics of SUH660 steel in hydrogen environment was described. A method was proposed to investigate the effect of hydrogen on crack initiation, and thereby predicting the change trend of fatigue life below the fatigue strength at 10^7 cycles after hydrogen-changing.

In chapter 4, general conclusions of the results obtained by the present studies were summarized.

References

[1] Derwent R, Simmonds P, O'Doherty S, Manning A, Collions W, Stevenson D. Global environmental impacts of the hydrogen economy. *Int. J. Nuclear Hydrogen Production and Application*, **1**; 2006, p. 57−67

[2] Lopes VV, Rangel CM, Novais AQ. Modelling and identification of the dominant phenomena in hydrogen fuel-cells by the application of DRT Analysis. *Computer Aided Chemical Engineering*, **32**; 2013, p. 283−8

[3] Zubaryeva A, Thiel C. Analyzing potential lead markets for hydrogen fuel cell vehicles in Europe: Expert views and spatial perspective. *International Journal of Hydrogen Energy*, **38**; 2013, p. 15878–86

[4] Mehmood A, Ha HY. Performance restoration of direct methanol fuel cells in long-term operation using a hydrogen evolution method. *Applied Energy*, **114**; 2014, p. 164–71

[5] Mousa G, Golnaraghi F, DeVaal J, Young A. Detecting proton exchange membrane fuel cell hydrogen leak using electrochemical impedance spectroscopy method. *Journal of Power Sources*, **246**; 2014, p. 110–6

[6] Thompson WA, Brooks AJ. Hydrogen performance of precipitation strengthened stainless steels based on A-286. *Metall Trans A*, **6A**; 1975, p. 1431−42

[7] Coffin LF. The effect of high vacuum on the cycle fatigue law. *Metall Trans*, **3**; 1972, p. 1777−87

[8] Kobayashi K, Yamaguchi K, Hayakawa M, Kimura M. High-temperature fatigue properties of austenitic superalloys 718, A286 and 304L. *Intl J Fatigue*, **30**; 2008, p. 1978−84

[9] Kubota M, Tanaka Y, Kondo Y. The effect of hydrogen gas environment on fretting fatigue strength of materials used for hydrogen utilization machines. *Tribology Int*, **42**; 2009, p. 1352−59

[10] Nakamura J, Miyahara M, Omura T, Semba H, Wakita M, Otome Y. Degradation of fatigue properties in high pressure gaseous hydrogen environment evaluated by cyclic pressurization tests.

Procedia Eng, **2**; 2010, p. 1235−41

[11] Garwood FM, Zurburg HH, Erickson AM. Correlation of laboratory tests and service performance: interpretation of tests and correlation with service. *American Society for Metals*; 1951, p. 1−77

[12] Morrow J, Halford RG, Millan FJ. Optimum hardness for maximum fatigue strength of steel. Proc. 1st Int. Conf. Fracture, Sendai, 2; 1966, p. 1611−35

[13] Aoyama S. Strength of hardened and tempered steels for machine structural use (Part 1). *Review of Toyota RD Center*, **5(2)**; 1968, p. 1-30. (Part 2), *ibid*, **5**(4); 1968, p. 1−35

[14] Nishijima S. Statistical analysis of fatigue test data (in Japanese). *J. Soc. Mater. Sci., Japan*, **29**; 1980, p. 24−9

[15] Murakami Y. Metal fatigue: Effects of small defects and non-metallic inclusions. UK: Elsevier; 2002

[16] Murakami Y, Endo M. Effects of hardness and crack geometries on ΔKth of small cracks emanating from small defects, in: Miller JK, Rios LDRE. *The Behaviour of Short Fatigue Cracks*. Mechanical Engineering Publications, 1986, p. 275−93

[17] Koh S. Elastic-plastic stress analysis and fatigue lifetime prediction of cross-bores in autofrettaged pressure vessels. *KSME International Journal*, **14**; 2000, p. 935−46

[18] Frost NE. The Effect of cold work on the fatigue properties of two steels. *Metallurgia*, **62**; 1960, p. 85−90

[19] Kage M, Nisitani H. The effect of tensile prestrain on the fatigue strength of strength-anisotropic rolled steel. *Bulletin of JSME*, **20**; 1977, p. 1359−66

[20] Kang M, Aono Y, Noguchi H. Effect of prestrain on and prediction of fatigue limit in carbon steel. *International Journal of Fatigue*, **29**; 2007, p. 1855−62

[21] Al-Rubaie KS, Del Grande MA, Travessa DN, Cardoso KR. Effect of pre-strain on the fatigue

life of 7050-T7451 aluminium alloy. *Materials Science and Engineering A*, **464**; 2007, p. 141−50

[22] Ikematsu K, Mishima T, Kang M, Aono Y, Noguchi H. Effect of prestrain on fatigue crack growth of age-hardened Al 6061-T6. ASTM STP 1508: *Fatigue and Fracture Mechanics*, **36**; 2009, p.561−73

[23] Brooks AJ, Thompson WA. Microstructure and hydrogen effects on fracture in the alloy A286. *Metall Trans A*, **24A**; 1993, p. 1983−91

[24] Cicco DH, Luppo IM, Gribaudo ML, Ovejero-García J. Microstructural development and creep behaviour in A286 superalloy. *Materials Characterization*, **52**; 2004, p. 85−92

[25] Shishime K, Kubota M, Kondo Y. Effect of absorbed hydrogen on the near threshold fatigue crack growth behavior of short crack. *Materials Science Forum*, **567 – 568**; 2013, p. 409−12

CHAPTER 2 THE FUNDAMENTAL FATIGUE CHARACTERISTICS IN AIR

Chapter 2.1 Fatigue strength characteristics evaluation considering small fatigue crack propagation behavior and hardness distribution

2.1.1 Introduction

SUH660 steel as an iron-based precipitation-hardened alloy, and the precipitates may be cut by dislocation in the plastic zone near a crack tip owing to stress concentration and cyclic deformation [1−3]. Such dislocations may lead to crack initiation near the crack tip after the crack is arrested, which affects the fatigue characteristics such as fatigue limit. Therefore, to guarantee safe and long-term use of SUH660 steel, its fatigue limit and hardness characteristics is investigated, and the behavior of the microscopic fatigue cracks is focused during the fatigue tests.

2.1.2 Experimental methods

Table 1 summarizes the chemical composition of the SUH660 steel samples used in this chapter. These samples were solution treated (ST) for 1 h at 980 °C, air cooled, aged (A) 16 h at 720 °C, and air cooled again.

The author performed tensile tests, fatigue tests, and Vickers hardness tests in this chapter. For the tensile tests, an AUTO GRAPH AG-5000 (Shimadzu Corporation) was used. For the fatigue tests, the author used an Ono-type rotating-bending fatigue test machine in air, at room temperature, at a testing frequency of 55 Hz. The microscopic fatigue crack behaviors were observed by using the replica method. For the high stress amplitudes, one fatigue specimen was analyzed at each stress level. For the low stress amplitudes, because of the fatigue life variability that resulted from the crack arrest, multiple fatigue specimens were prepared to determine the fatigue strength at 10^7 cycles. However, the threshold point of the fatigue strength at 10^7 cycles appeared after using three specimens. Figure 1 shows the shapes and dimensions of the tensile and fatigue test specimens. To determine the behavior of the fatigue crack originating from the initial crack, the author prepared a smooth fatigue specimen with a small artificial hole as shown in Fig. 1(c). According to the crack initiation behavior of SUH660 steel, which will be discussed in Section 2.1.4.1, the crack was initiated in a grain. Hence, the diameter and depth of the artificial hole that was used to simulate the initial crack with the longest length were comparable to the length of the maximum grain on the specimen surface, which was approximately 200 μm according to the microstructure of the specimen surface shown in Fig. 2. The test specimen surfaces were buff-polished after machining and then electro-polished at 50 °C to remove the damaged surface layer, which was 10−20 μm. To clearly describe the fatigue characteristics of SUH660 steel, its fatigue characteristics were compared with those of general steel such as carbon steel, which has a clear fatigue limit that can be predicted using Murakami's equation [4].

A Vickers hardness test was performed to determine the relationship between the hardness and fatigue life of the material. The indentation load was 0.49 N, and the indentations were made at the grain centers to avoid grain boundary effects.

2.1.3 Experimental results

Figure 3 shows the results of the tensile tests conducted on SUH660 steel. From Fig. 3(a), the tensile strength (σ_B) was 1065 MPa, the 0.2% proof stress ($\sigma_{0.2}$) was 664 MPa, and the elongation (δ) was 27.6%. The fractured tensile specimen shown in Fig. 3(b) has a cup-and-cone fracture, which is a type of fracture in common ductile steel such as general steel.

Figure 4 shows the *S-N* diagram of SUH660 steel. The fatigue life increased as the stress amplitude decreased from 400 MPa to 280 MPa, and the fatigue life did not exceed 10^7 cycles. However, when the stress amplitude decreased from 280 MPa to 260 MPa, the increase in the fatigue life was considerably greater than expected, and fatigue failures occurred even after the number of cycles (*N*) reached 10^7. Therefore, the fatigue strength at 10^7 cycles is approximately 270 MPa.

Figure 5 shows the Vickers hardness distribution on the SUH660 specimen surface. In the Vickers hardness test, approximately the same value was obtained within a distance of several crystal grain sizes from the first measured position. Significantly different *HV* values were obtained at measured positions separated by a distance of 1 mm or more. The surface hardness of SUH660 steel varied, whereas general steel has constant hardness. To discuss the hardness scatter, which depends on the measured positions, a 600 μm × 450 μm region was defined as a zone, which is equal to the field of view of the ×200 microscope used in this chapter. Zones A and B were the test zones on the specimen surface before the fatigue test. The author performed the Vickers hardness test on grains within a distance of several crystal grain sizes, and the Vickers hardness (*HV)* values of the grains in Zone B were clearly higher than those of the grains in Zone A. Therefore, in this chapter, zones with low Vickers hardness such as that of Zone A were regarded as low hardness zones, whereas those with high Vickers hardness such as that of Zone B were regarded as high hardness zones.

2.1.4 Discussion

2.1.4.1 Crack initiation mechanism and crack propagation behavior

According to the *S-N* diagram of SUH660 steel shown in Fig. 4, the fatigue failure mechanism at high stress amplitudes (> 270 MPa) was expected to be different from that at low stress amplitudes (< 270 MPa). Therefore, to clarify the difference between the fatigue failure mechanisms at high and low stress amplitudes, the fatigue crack propagation behaviors at σ_a values of 400 and 230 MPa are discussed. Figure 6 shows the crack growth behaviors of the specimen with a 200-μm-diameter artificial hole and that without an artificial hole for a σ_a value of 400 MPa. Figure 6(a) shows the relationships between the crack length and the number of cycles for the three types of fatigue cracks: a crack initiated from the artificial hole, a crack initiated from the smooth surface of the specimen with an artificial hole, and a crack initiated from the smooth surface of the specimen without an artificial hole. Figures 6(b) and (c) show the crack growth rates of the three types of fatigue cracks at σ_a = 400 MPa. For the cracks initiated from the smooth surface in both specimens, the crack growth rate accelerated with the number of cycles until the fatigue failure. For the crack initiated from the artificial hole, although the crack growth rate was high in the early stage because of the stress concentration at the edge of the hole, the crack growth rate became similar to that of the crack initiated from the smooth surface after a number of cycles, and accelerated until the fatigue failure. Therefore, the cracks in both specimens exhibited the same crack growth behaviour; i.e., monotonously growth without arrest at σ_a = 400 MPa. Notably, the fatigue failure of the specimen with an artificial hole was not because of the crack initiated from the artificial hole, but because of the crack that was initiated and propagated from the smooth surface. This behavior is different from that of general steel, wherein catastrophic fatigue failure results from a crack initiated at a 200-μm-diameter hole, which acts as a defect and is propagated further. Therefore, a 200-μm-diameter hole does not affect the fatigue strength of SUH660 steel, which is considered to

be related to its hardness variability as explained in Section 2.1.4.3.

Figure 7 shows the distribution map of the crack length at σ_a = 230 MPa. Many fatigue cracks could be observed on the surface during the fatigue test. Furthermore, because fatigue failure did not occur after N of 7.5×10^7 cycles at σ_a = 230 MPa, the longest fatigue crack shown in Fig. 8 is discussed. Figure 9 shows the crack propagation behavior of the longest fatigue crack at σ_a = 230 MPa. As can be seen from Fig. 9(a), the longest fatigue crack propagated intermittently; the longest crack was arrested after growing to a certain length, and re-propagated after some millions of cycles. Hence, the crack length increased even after N of 10^7 cycles. Figure 9(b) shows the crack growth rate at σ_a = 230 MPa. The crack growth rate decelerated with the number of cycles in the early stage of the crack growth. However, the decelerating crack growth rate did not re-accelerate but continued to decelerate to zero. Throughout the crack re-propagation, the crack growth rate instantaneously increased to a higher value and then decreased to zero. Figure 10 shows the crack re-propagation behavior of the longest crack in the specimen. After the last crack re-propagation, the fatigue crack was arrested between N of 4.8×10^7 cycles (Fig. 10(a)) and N of 5.8×10^7 cycles (Fig. 10(b)), which means that the crack length did not change over ten millions cycles. However, between N of 5.8×10^7 cycles (Fig. 10(b)) and N of 5.9×10^7 cycles (Fig. 10(c)), the arrested crack re-propagated and the crack length increased by 86 μm over one million cycles. However, the crack re-propagation occurred between the replication so that its mechanism could not be observed in the longest crack. Therefore, to clarify the reason for crack re-propagation, another temporarily arrested crack in the same specimen as the longest crack is shown in Fig. 11. The crack was arrested over three million cycles between N of 6.0×10^7 cycles (Fig. 11(a)) and N of 6.3×10^7 cycles (Fig. 11(b)). However, at N of 6.4×10^7 cycles (Fig. 11(c)), a new crack was initiated near the tip of the temporarily arrested crack. Over the next one million cycles, the temporarily arrested crack coalesced with the neighboring new crack and the crack length was increased. The intermittent crack propagation is

therefore considered to be related to the new crack initiation near the tip of the temporarily arrested crack.

To clarify the effect of the crack initiation on the fatigue strength of SUH660 steel, the crack initiation behaviors on a smooth surface and in the region near the tip of the temporarily arrested crack are discussed. Figure 12 shows the crack initiation behavior at σ_a = 230 MPa. A thin line appeared in the grain and its length increased until a crack was initiated and began to propagate. It has been severally reported that fatigue crack initiation in FCC metals results from persistent slip bands (PSBs) [5−7]. Miao et al. [8] showed that microcracks on the surface of an FCC specimen were as long as the crystal grain size and propagated through the grain boundary. Rasmussen et al. [9] reported that PSBs could not propagate across grain boundaries. Therefore, the line, the length of which is no longer than the grain size before it becomes crack, is considered to be produced by cyclic strain localization within the PSBs. This means that the crack initiation in SUH660 steel is due to slip generation and accumulation in the crystalline structure, which we refer to here as a PSB crack. To investigate the initiation origin of the longest crack in Fig. 8 on its fracture surface, a stress amplitude of 280 MPa instead of 230 MPa was applied to induce fatigue failure. Figure 13 shows the correlation between the surface crack and the fractured specimen surface; corresponding points are identified by dotted lines. As indicated in Fig. 13, two small cracks coalesced to form the longest crack. Hence, there are two crack initiation sites. At the two crack initiation sites, no defects such as inclusions, but only flat areas produced by cyclic strain localization can be observed. In addition, at the new crack initiation site near the tip of the temporarily arrested longest crack, a flat area without any defects can be observed. Therefore, as in crack initiation on a smooth surface, it is considered that slip concentration actually occurs in the crystalline structure near the tip of the temporarily arrested crack, which initiates a new crack.

The fatigue crack behavior of SUH660 steel can be summarized as follows. At high stress

amplitudes, the crack propagates monotonically as is general steel. At low stress amplitudes, the crack propagates intermittently. The crack is temporarily arrested, and after a large number of cycles, a new crack is initiated near the tip of the arrested crack. The two cracks then coalesce, resulting in the re-propagation of the temporarily arrested crack.

2.1.4.2 *S-N* diagram of SUH660 steel with two "fatigue limits"

In Section 2.1.4.1, different fatigue failure mechanisms of SUH660 steel for high and low stress amplitudes were discussed. Because a fatigue crack grows monotonously without arrest at high stress amplitudes, the fatigue life is considered to be dominated by the crack growth rate. The fatigue life increases linearly on a log scale with decreasing stress amplitude. At low stress amplitudes, because a fatigue crack propagates with intermittent arrests, the fatigue life is considered to be dominated by the temporarily arrested crack behavior. Thus, the fatigue life increases nonlinearly on a log scale in the region of the fatigue strength at 10^7 cycles. Therefore, the fatigue failure mechanism of SUH660 steel is different from those of general steel (wherein the crack is non-propagated at the fatigue limit) and aluminum alloy (wherein the cracks propagates slowly after more than 10^7 cycles until the fatigue failure). The *S-N* curve with the fatigue limit of general steel and the *S-N* gentle curve without the fatigue limit of aluminum alloys cannot be used for SUH660 steel. Therefore, based on the crack propagation behavior, a new *S-N* diagram with two "fatigue limits" as shown in Fig. 14 is suggested for SUH660 steel. The new *S-N* diagram with two "fatigue limits" was referred from the paper by Mughrabi et al. [10], who used the *S-N* curve with multiple fatigue limits to express the surface and internal fatigue limits. However, in this chapter, different meanings are given to the two "fatigue limits".

The new *S-N* diagram of SUH660 steel with two "fatigue limits" consists of four parts. Part 1of the *S-N* diagram is a sloping straight line, which indicates that a fatigue crack propagates monotonically and the fatigue life increases linearly on a log scale at high stress amplitudes, as in general steel.

Part 2 of the *S-N* diagram is a horizontal line that represents Fatigue Limit I. In this chapter, Fatigue Limit I is the threshold of the temporary crack arrest. At Fatigue Limit I, although the temporarily arrested crack behavior causes the fatigue life to exceed *N* of 10^7 cycles, fatigue failure

also occurs. Hence, Fatigue Limit I is not the true fatigue limit and could be considered to be the fatigue strength at 10^7 cycles. Based on the specimen and the fracture surfaces of the longest temporarily arrested crack shown in Fig. 13, a crack propagates at nearly 45° to the direction of the stress amplitude on the specimen surface. Besides the flat areas at the crack initiation sites and the region near the tip of the temporarily arrested crack on the fracture surface, more flat areas could be observed around the crack initiation site. Therefore, on the specimen surface, a fatigue crack easily grows via Mode II. Inside the specimen, a fatigue crack grows via Mode II in the early stages of the crack growth, but the growth changes to Mode I as the propagation continues. Before the temporary crack arrest, the Mode I crack propagates over larger area than the Mode II crack inside the specimen. Thus, the author considered that, in SUH660 steel, besides the plasticity-induced crack closure, the roughness-induces crack closure may affect the temporary crack arrest. Suresh and Ritchie [11] reported that a predominantly Mode I characteristic resulted in a marked reduction in roughness-induced closure at higher crack growth rates. Therefore, for SUH660 steel, the plasticity-induced crack closure is considered to be the primary cause of the temporary crack arrest. Moreover, Murakami's equation [4], which can be used for predicting the fatigue limit of the general steel caused by plasticity-induced crack closure, may be applicable to predicting the fatigue strength at 10^7 cycles of SUH660 steel. The method for predicting the fatigue strength at 10^7 cycles for SUH660 steel will be presented in Chapter 2.2.

Part 3 of the *S-N* diagram is a sloping line, which indicates that the crack intermittently propagates as a result of a new crack initiation near the tip of the temporarily arrested crack. Because the temporarily arrested crack behavior dominates the fatigue life, the data scatter region for low stress amplitudes is considered to be much larger than that for high stress amplitudes. Therefore, existing data obtained from fatigue tests do not express the increasing trend of the fatigue life at low stress amplitudes. In this chapter, a sloping straight line was temporarily used to depict Part 3 for

easy comparison with the horizontal line that represents the fatigue limit. Some studies on precipitation-hardened materials found that dislocation movements were initiated at a crack tip as a result of stress concentration, which cut the precipitates in the plastic region near the crack tip [1−3]. Therefore, SUH660 steel behaves like a precipitation-hardened material, wherein the grains are strengthened by the precipitated γ′-phase (Ni_3(Al, Ti)) [12, 13]. Thompson et al. [14] investigated the relationship between γ′-phase particles size and aging time at 720 °C in SUH660 steel, thus the diameter of γ′-phase particles of the material used in this paper can be estimated to be approximately 10 nm after aged 16 h. Many studies [15−18] reported that, the ordered nano-sized γ′-phase particles is easy to be cut by dislocations during plastic deformation in Fe−Ni based austenitic alloy and nickel superalloy. Therefore, the γ′-phase particle in SUH660 steel is considered to be cut in the plastic region around fatigue crack. Because the sheared precipitate particles lose some of their resistance to dislocation motion [19], in the grains of plastic region, the resistance to slip becomes lower and then promotes slip generation and accumulation. The new crack initiation near a crack tip is considered to be related to precipitate cutting. Accordingly, the author suggests a model that describes the relationship between the precipitate and the new crack initiation near the tip of the temporarily arrested crack. Schematic diagrams of the new crack initiation model near the tip of the temporarily arrested crack at low stress amplitudes are shown in Fig. 15. Figure 15(a) shows a crack is initiated in the soft grain. Because the slip direction in the soft grain is close to the direction of the maximum shear stress, large numbers of dislocations generate and pile up at the precipitates. With the accumulation of dislocations, the dislocations shear the precipitates, and cause slipping in the grain. Thus, the crack is initiated in the soft grain owing to local accumulation of slip. For the other grains, because their slip directions are not close to the direction of the maximum shear stress, the shear stress loaded on their slip plane is lower than the soft grains. Thus, precipitate shearing and slip accumulation requires more cycles owing to their inefficient dislocation generation and

accumulation. Even for some hard grains, because of too low shear stress on their slip plane, the dislocations could not generate nor shear the precipitate. Thereafter, the crack propagates, plastic deformation occurs around the crack tip owing to stress concentration, and the precipitates are cut in plastic region. In the plastic region, plastic deformation increases the critical shear stress of dislocation generation, precipitate cutting decreases the slip resistance, respectively. Fig. 15(b) shows the crack temporarily arrest. In the plastic region around the temporarily arrested crack, because stress concentration decreases far from crack tip, the level of plastic deformation and precipitate cutting also decreases far from crack. Thus, in somewhere of plastic region, which is a little far from crack, the slip generation is considered to be promoted. Moreover, because of stress concentration near the tip of temporarily arrested crack, the new crack is considered to be easy initiated in the plastic region around crack tip than others. Thereafter, in Fig. 15(c), after some millions cycles, slips concentrate in the weakened grains near the tip of the temporarily arrested crack, resulting in a new crack initiation. In Fig. 15(d), the temporarily arrested crack coalesces with the new crack and re-propagates. Therefore, precipitate cutting, which reduces the slip resistance in the region near the temporarily arrested crack tip, is considered to be the fundamental cause of the intermittent crack propagation.

Part 4 of the *S-N* diagram is a horizontal line that represents Fatigue Limit II. Because the plastic zone near the tip of the temporarily arrested crack is soft owing to precipitate cutting, loading by the fatigue test stress initiated new cracks more easily near the tip of the temporarily arrested cracks than in other fields. The author assumes that when the fatigue test stress is sufficiently low, there are two possibilities: (1) the PSB crack is initiated in a grain but cannot propagate; (2) the PSB crack cannot be initiated in a grain. In Case 1, because the PSBs cannot propagate across the grain boundaries [9], a plastic region is not formed near the PSB crack tip, which means that there is no precipitate cutting and a new crack initiation is not promoted near the PSB crack tip. Consequently,

if a PSB crack cannot propagate after its initiation in a grain, the fatigue crack cannot grow and fatigue fracture cannot occur. The author regards Case 1 as the threshold of PSB crack propagation. In Case 2, no PSB crack is initiated on the specimen surface. Hence, no fatigue crack is initiated and fatigue fracture does not occur. The author regards Case 2 as the threshold of PSB crack initiation. If the fatigue behaviors are continuously observed under decreasing fatigue stress, Fatigue Limit II can be determined to be caused by the threshold of PSB crack propagation or the threshold of PSB crack initiation. However, because of the significant time required and the variability of the fatigue strength, it is very difficult to determine Fatigue Limit II by an actual experiment. Therefore, the safe side of Fatigue Limit II, which is based on the threshold theory of PSB crack behavior, is suggested for the prediction. In this chapter, $\sigma_{w,II}$ was used as the safe side of Fatigue Limit II, and it is equal to or lower than the true value to enable safe use for actual production. Because there have been few studies on PSB crack initiation, the author predicted the safe value based on the dislocation behavior at the threshold of PSB crack propagation.

The author initially assumed a fatigue test stress value close to the threshold of PSB crack propagation to ensure that there was a PSB crack in a grain and that it started propagating. When the specimen was tensile-loaded for the first time, the stress concentration caused the stress in the region of the crack tip to exceed the positive direction elastic limit, leading to dislocation emission from the crack tip. This resulted in plastic deformation and subsequent blunting of the crack tip. When the tensile stress was unloaded, part of the plastic deformation in the region of the crack tip was recovered. When the compressive stress was loaded, the low-level stress concentration at the blunted crack tip prevented the stress loaded in the region of the crack tip from exceeding the elastic limit in the opposite direction. In addition, there was no plastic deformation, and the blunted crack tip could therefore not regain its sharpness. Thereafter, when the cyclic stress was loaded, the stress in the region of the crack tip did not exceed the elastic limit in the positive and opposite directions.

Dislocation emission could therefore not occur from the crack tip, and the PSB crack did not propagate in either Mode I or Mode II. Therefore, the critical stress intensity factor for dislocation emission, K_e, can be used for predicting the safe side value of Fatigue Limit II. Based on the stress in the region of the crack tip within the elastic limit in the positive and opposite directions, up to the safe side of Fatigue Limit II, the threshold stress intensity range for the safe side value of Fatigue Limit II is given by $\Delta K_{eff,th} = +K_e - (-K_e) = 2K_e$. In his study of dislocation formation conditions, Weertman [20] found that the threshold stress intensity factor for dislocation formation was given by K_{th} = 1.1–1.8 MPa$\sqrt{m}$ for iron-based alloys. Many researchers [21−24] have obtained the threshold effective stress intensity factor range for non-propagating cracks in iron-based alloys as $\Delta K_{eff,th}$ = 2–4 MPa$\sqrt{m}$. The large significant discrepancy between these results is ascribed to the use of different experimental methods. Moreover, the plastic zone near the non-propagating crack affects the dislocation formation limit. Therefore, the value of $\Delta K_{eff,th}$ for a non-propagating crack cannot be used to predict the safe side value of Fatigue Limit II. Murakami [4] measured the critical value of annealed 0.46% C steel to be approximately 1.8 MPa$\sqrt{m}$ under a stress ratio = −1, $K_{max,th}$. For this ratio, no crack is initiated from the initial crack. Because annealing treatment remove plastic deformation around the initial crack, no residual stress affect fatigue crack initiation and propagation, thus the initial crack can be approximately regarded as the PSB crack. At the critical stress intensity factor, after the cycle stress of first time, the blunted crack tip decreased the stress concentration and prevented dislocation emission. Thereafter, plastic deformation could not occur around crack tip, fatigue crack could not be initiated from the tip of initial crack. Therefore, for annealed 0.46% C steel, its critical value of crack initiation from initial crack, $K_{max,th}$, can be considered as its critical stress intensity factor for dislocation emission, K_e. For alloy materials, the solute atom, precipitate and inclusion only offer resistance to dislocation motion, cannot affect the dislocation generation and emission from crack tip. Ohr [25] indicated that, the value of K_e is only dependent on the core radius

of the dislocation, which means the matrix dominate the critical stress intensity factor for dislocation emission. Thus, as an iron-based alloy, SUH660 steel has the same value of K_e as 0.46% C steel. Therefore, for a PSB crack in SUH660 steel, $\sigma_{w,II}$ is used as the safe side value of Fatigue Limit II, $\Delta K_{eff,th} = 0.65[+\sigma_{w,II} - (-\sigma_{w,II})]\sqrt{\pi(\sqrt{area})} = 2K_e = 2 \times 1.8 = 3.6$ MPa$\sqrt{\text{m}}$. For a plain specimen, because the PSB crack size depends on the grain size, the maximum grain size is used to predict the safe side value of Fatigue Limit II. According to Fig. 2, the maximum grain size is approximately 200 μm. If the shape of the PSB crack is considered to be semicircular, the radius of the semicircle would be 100 μm and its area would be 15700 μm^2. Hence, $\sqrt{area}_{\max} = 125$ μm. The safe side value of Fatigue Limit II, $\sigma_{w,II}$, is approximately 140 MPa.

The properties of the SUH660 steel *S-N* diagram with two "fatigue limits" can be summarized as follows. Fatigue Limit I is the fatigue strength at 10^7 cycles, and although it is predicted using Murakami's equation, it is not the true fatigue limit. Fatigue Limit II is considered as the threshold of either PSB crack propagation or PSB crack initiation. Because it is difficult to be determined by an actual experiment, the safe side of Fatigue Limit II, which based on the threshold theory of PSB crack behavior, is suggested for the prediction.

2.1.4.3 Effect of hardness variability on fatigue strength of SUH660 steel

If the fatigue strength at 10^7 cycles of SUH660 steel is substituted for the fatigue limit, the fatigue strength ratio σ_w/σ_B (where σ_w is the fatigue limit and σ_B is the tensile strength) would be 0.25, which is lower than 0.5, the ratio for general steel. This indicates that the fatigue strength of SUH660 steel is lower than its tensile strength. In Fig. 16, the *HV* values of the grains in the low and high hardness zones shown in Fig. 5 are plotted on a normal probability paper. The Vickers hardness distribution in each test zone follows a normal distribution, and the tilt degrees of the fit lines for the low and high hardness zones are almost similar. This is because the crystal orientation varies randomly from grain to grain, which causes the zones to have similar Vickers hardness variability. The line spacing between the low hardness zone and high hardness zones represents different hardness levels, which indicates the existence of hardness variability in SUH660 steel. Some researchers have reported that the hardness of a metal depends on the grain size, solid solution element, precipitate, and phase [26]. Because SUH660 steel is an austenitic precipitation-hardened stainless steel, the solid solution element and austenitic phase are the same in all the grains of a particular specimen. In the Vickers hardness test of this chapter, the *HV* data were obtained from the center of the grain and therefore did not affect the results of the Vickers hardness test. The author therefore surmises that the hardness variability was related to the precipitate; i.e., heterogeneous sizes or non-uniform numbers cause different resistance to dislocation motion and slip generation.

The fatigue specimen for *HV* test is electro-polished to remove indentations after *HV* test, and then to be used for fatigue test at σ_a = 230 MPa. Figure 17 shows the crack distribution on the surface of the SUH660 fatigue test specimen at σ_a = 230 MPa after 6.0×10^7 cycles. The cracks in the different fields of the SUH660 plain specimen surface varied from a few to many. In Fig. 18, the *HV* data of the zone containing many cracks and that containing few cracks are plotted on a normal probability paper. The Vickers hardness distribution in the many cracks zone is lower than that in the

few cracks zone. This indicates that cracks are initiated more easily in a low hardness zone than in a high hardness zone. In the high stress amplitudes, cracks monotonously propagate, and because of the much large proportion of crack propagation life in the fatigue life, the crack propagation life dominates the fatigue life. Miller [27] reported that, for microcrack, the microstructure has a large effect on the growth rate of microcrack, however, for long crack, its stress intensity factor is large, the influence of microstructure becomes smaller. Thence, it is considered that, for the cracks which are initiated in different zones with different hardness, their growth rates varies in the stage of microcrack, but tend to be similar after becoming long cracks. For SUH660 steel, because the crack growth rate of crack length from 100 μm to 1000 μm is accelerated owing to pre-strain (according to Fig. 7 in Chapter 2.3), the fatigue crack, whose length is no longer than 1000 μm, is considered as a microcrack. Moreover, according to the crack growth curves shown in Fig. 6, the crack propagation life of microcrack accounts for most proportion of crack propagation life. Therefore, the hardness of microcrack propagation pathway is considered to affect the propagation life of microcrack, and dominates the fatigue life. For metal, hardness is the level of resistance to plastic deformation [28]. Thus, the crack easily propagates in the low hardness zone with low resistance to plastic deformation. And because the maximum length of microcrack is less than twice size of zone, the microcrack only propagates to the adjacent zone. Therefore, the microcrack is considered to be initiated and propagated in the low hardness region, which means the low hardness region dominates the fatigue life. In the low stress amplitudes, the crack is temporarily arrested, and the fatigue life becomes much longer owing to temporarily crack arrest. In low hardness region, because of low resistance to plastic deformation at crack tip, the shear stress loaded at crack tip easily exceeds the elastic limit. Thus, compared to the crack in high hardness region, the crack is different to temporarily arrest in low hardness region, which means that the fatigue life is dependent on the temporary crack arrest behavior in low hardness region. Because the primary crack is temporarily arrested with its length of

approximate 500μm (according to Fig. 8 in Chapter 2.2), the primary crack is considered to be initiated, propagated and temporarily arrested in the low hardness zone. Therefore, the author considered that the low hardness zone dominated the fatigue strength of SUH660 steel and caused the low fatigue strength. This is the reason why the 200-μm-diameter hole did not affect the fatigue strength of SUH660 steel's as noted in Section 2.1.4.1.

However, as shown in Fig. 3, the tensile strength of SUH660 steel is high, compared to its low fatigue strength. Different zones in SUH660 steel exhibit different levels of plastic deformation resistance owing to the hardness variability of the material. When the tensile stress approaches the yield strength, the low hardness zone yields first, and the high hardness zone later yields as the tensile stress increases further. After the yielding of all the zones, the entire specimen undergoes uniform plastic deformation until the tensile stress reaches the maximum value. The low and high hardness zones resist plastic deformation and concurrently affect the tensile strength, leading to high tensile strength. Therefore, because of the hardness variability, the iron based precipitation hardened alloy SUH660 has a high tensile strength and low fatigue strength, which results in a lower fatigue strength ratio than that of general steel.

2.1.5 Conclusions

To investigate the fatigue strength characteristics of SUH660 steel, tensile tests, fatigue tests, and Vickers hardness tests were performed. The conclusions are as follows.

(1) SUH660 steel exhibits two types of crack propagation behaviors: (1) cracks propagate monotonously at high stress amplitudes; (2) crack propagates intermittently at low stress amplitudes, wherein the crack is temporarily arrested, and after a large number of cycles, a new crack is initiated near the tip of the arrested crack and coalesces with it, leading to re-propagation of the temporarily arrested cracks.

(2) The *S-N* diagram for SUH660 steel consists of two "fatigue limits". Fatigue Limit I is the fatigue strength at 10^7 cycles, which is not the true fatigue limit of SUH660 steel. However, it can be predicted by Murakami's equation because the temporarily arrested crack behavior is considered to be caused by plasticity-induced crack closure, as in general steel below the fatigue limit. Fatigue Limit II is the true fatigue limit and is considered to be the threshold of either PSB crack propagation or PSB crack initiation. However, because it is difficult to determine by an actual experiment, the safe side of Fatigue Limit II, which is based on the threshold theory of PSB crack behavior, is suggested for the prediction.

(3) The hardness variability of SUH660 steel results in low fatigue strength because fatigue cracks are initiated and propagate more easily in the low hardness zones. In addition, the hardness variability produces high tensile strength because the low and high hardness zones concurrently resist plastic deformation, thus affecting the tensile strength. Therefore, SUH660 steel has a lower fatigue strength ratio than general steel.

References

[1] Broom T, Mazza AJ, Whittaker NV. Structural changes caused by plastic strain and by fatigue in Aluminium-Zinc-Magnesium copper alloys corresponding to DTD 683. *J Inst Metals*, **86**; 1957, p. 17−23

[2] Wang ZG, Rahka K, Nenonen P, Laird C. Changes in morphology and composition of carbides during cyclic deformation at room and elevated temperature and their effect on mechanical properties of Cr-Mo-V steels. *Acta Metall*, **33**; 1985, p. 2129−41

[3] Klesnil M, Lukac P. Fatigue of metallic materials. Elsevier; 1992, p. 46−50

[4] Murakami Y. Metal fatigue: effects of small defects and non-metallic inclusions. UK: Elsevier; 2002.

[5] Man J, Vystavel T, Weidner A, Kubena I, Petrenec M, Kruml T, Polak J. Study of cyclic strain localization and fatigue crack initiation using FIB technique. *International Journal of Fatigue*, **39**; 2012, p 44−53

[6] Miao J, Pollock TM, Jones JW. Crystallographic fatigue crack initiation in nickel-based superalloy René 88DT at elevated temperature. *Acta Materialia*, **57**; 2009, p. 5964−74

[7] Differt K, Essmann U, Mughrabi H. A model of extrusions and intrusions in fatigued metals II. Surface roughening by random irreversible slip. *Philosophical Magazine A*, **54**; 1986, p. 237−58

[8] Miao J, Pollock TM, Jones JW. Microstructural extremes and the transition from fatigue crack initiation to small crack growth in a polycrystalline nickel-base superalloy. *Acta Materialia*, **60**; 2012, p. 2840−54

[9] Rasmussen KV, Pedersen OB. Fatigue of copper polycrystals at low plastic strain amplitudes. *Acta Metallurgica*, **28**; 1980, p.1467−78

[10] Mughrabi H. On 'multi-stage' fatigue life diagrams and the relevant life-controlling mechanisms in ultrahigh-cycle fatigue. *Fatigue Fract Eng Mater Struct*, **25**; 2002, p. 755−64

[11] Suresh S, Ritchie RO. A geometric model for fatigue crack closure induced by fracture surface roughness. *Metall Trans A*, **13A**; 1982, p. 1627−31

[12] Brooks AJ, Thompson WA. Microstructure and hydrogen effects on fracture in the alloy A286. *Metall Trans A*, **24A**; 1993, p. 1983−91

[13] Cicco DH, Luppo IM, Gribaudo ML, Ovejero-García J. Microstructural development and creep behaviour in A286 superalloy. *Materials Characterization*, **52**; 2004, p. 85−92

[14] Thompson AW, Brooks JA.The mechanism of precipitation strengthening in an iron-base superalloy. *Acta Metallurgica*, **30**; 1982, p. 2197–203

[15] Ducki KJ. Structure and precipitation strengthening in a high-temperature Fe–Ni alloy. *Archives of Materials Science and Engineering*, **28**; 2007, p. 203–10

[16] Lippold JC, Kiser SD, DuPont JN. Welding Metallurgy and Weldability of Nickel-Base Alloys. John Wiley & Sons, 2011

[17] Guo Z, Zhao M, Li C, Chen S, Rong L. Mechanism of hydrogen embrittlement in a gamma-prime phase strengthened Fe–Ni based austenitic alloy. *Materials Science and Engineering: A*, **555**; 2012, p. 77–84

[18] Chen S, Zhao M, Rong L. Effect of grain size on the hydrogen embrittlement sensitivity of a precipitation strengthened Fe–Ni based alloy. *Materials Science and Engineering: A*, **594**; 2014, p. 98–102

[19] Takahashi A, Ghoniem NM. A computational method for dislocation–precipitate interaction. *Journal of the Mechanics and Physics of Solids*, **56**; 2008, p. 1534–53

[20] Weertman J: Fatigue crack growth in ductile metal, Mechanics of Fatigue, edited by Mura T. *ASME AMD*, **47**; 1986, p.11

[21] Kondo Y, Sakae C, Kubota M, Kudou T. The effect of material hardness and mean stress on the fatigue limit of steels containing small defects. *Fatigue & Fracture of Engineering Materials &*

Structures, **26**; 2003, p. 675−82

[22] Pokluda J, Kondo Y, Slamecka K, Sandera P, Hornikova J. Assessment of extrinsic crack tip shielding in austenitic steel near fatigue threshold. *Key Eng Mater*, **385-387**; 2008, p. 49−52

[23] Ishihara S, Yoshifuji S, Mcevily AJ, Kawamoto M, Sawai M, Takata M. Study of the fatigue lifetimes and crack propagation behaviour of a high speed steel as a function of the R value. *Fatigue & Fracture of Engineering Materials & Structures*, **33**; 2010, p. 294−302

[24] Tamura E, Ohji K, Kubo S, Nakai Y, Shiotari S, Enoki H, Kacou TAP. Near-threshold fatigue crack growth behavior of SUS304 steel at high temperatures using interferometric strain/displacement gage: 2nd report, fatigue crack growth behavior. *JSME International Journal Series A*, **42**; 1999, p. 97−103

[25] Ohr SM. Electron microscope studies of dislocation emission from cracks. *Scripta Metallurgica*, **20**; 1986, p. 1501−5

[26] Dowling NE. Mechanical behavior of materials (4th edition). Prentice Hall; 2012.

[27] Miller KJ. Materials science perspective of metal fatigue resistance. *Materials Science and Technology*, **9**; 1993, p. 453−62

[28] Clifford M, Simmons K, Shipway P. An Introduction to Mechanical Engineering: Part 1. CRC Press; 2009.

List of tables and figures

Table 1 Chemical composition of SUH660 samples (wt. %).

C	Si	P	S	Ni	Cr	Mo	Ti	V	Al	Fe	N	B
0.041	0.11	0.003	0.0017	25.4	15.19	1.43	2.23	0.30	0.21	Bal.	0.0012	0.0033

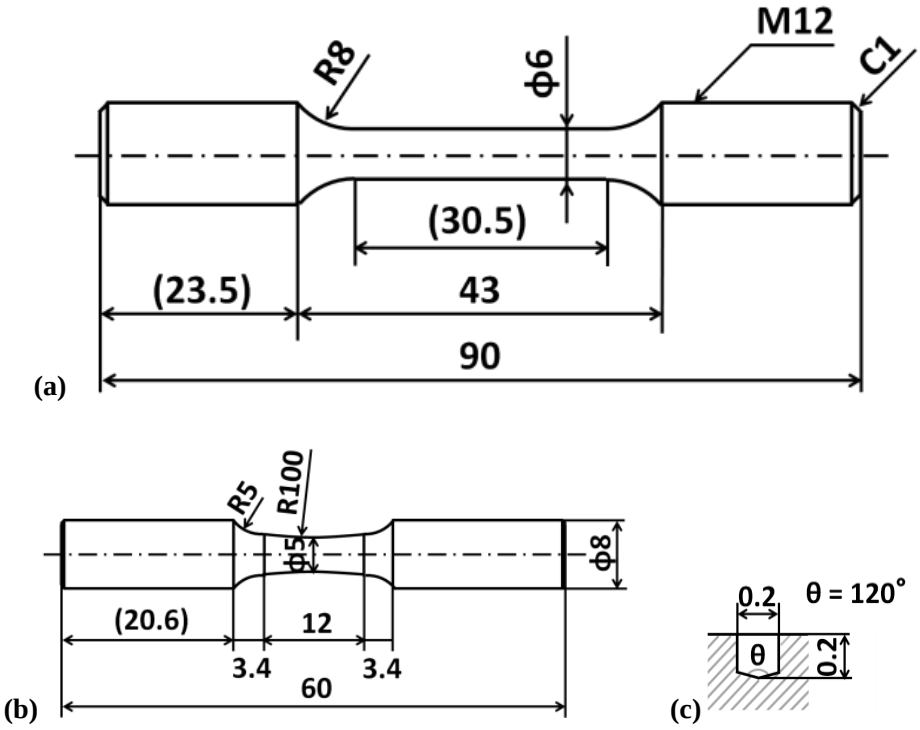

Fig. 1 Shapes and dimensions of specimens (unit: mm): (a) tensile test specimen;

(b) fatigue test specimen (with artificial hole and without artificial hole);

(c) artificial hole for fatigue test specimen.

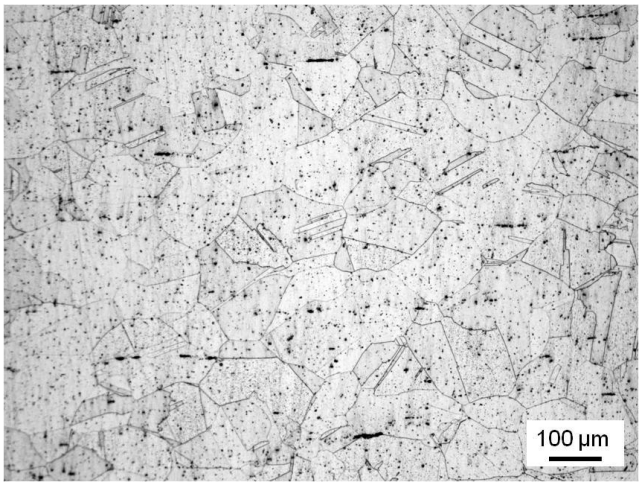

Fig. 2 Microstructure of SUH660 steel.

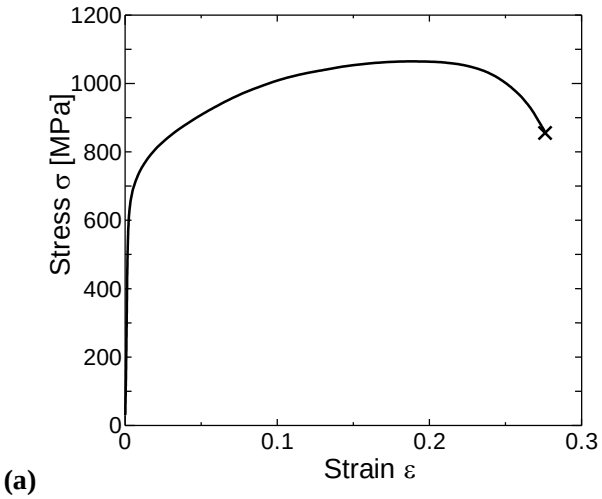

(a)

(b)

Fig. 3 Tensile test of SUH660 steel: (a) stress-strain curve;

(b) fractured tensile specimen.

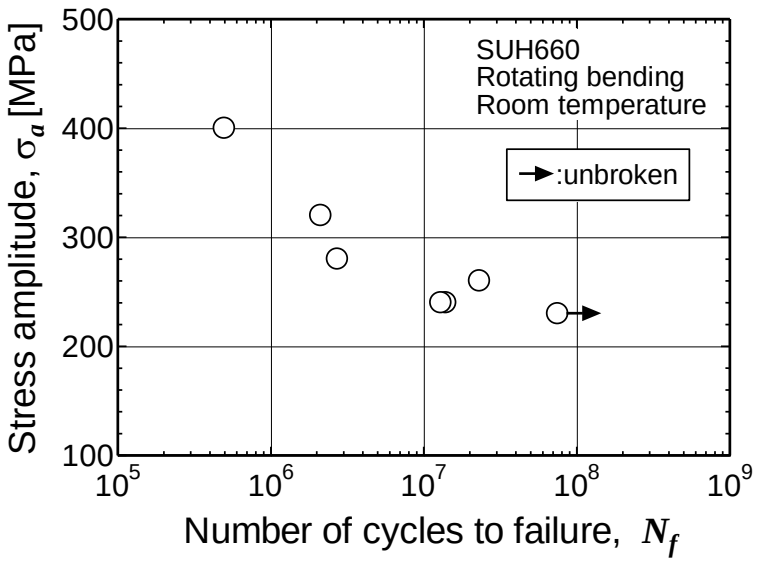

Fig. 4 *S-N* diagram of SUH660 steel.

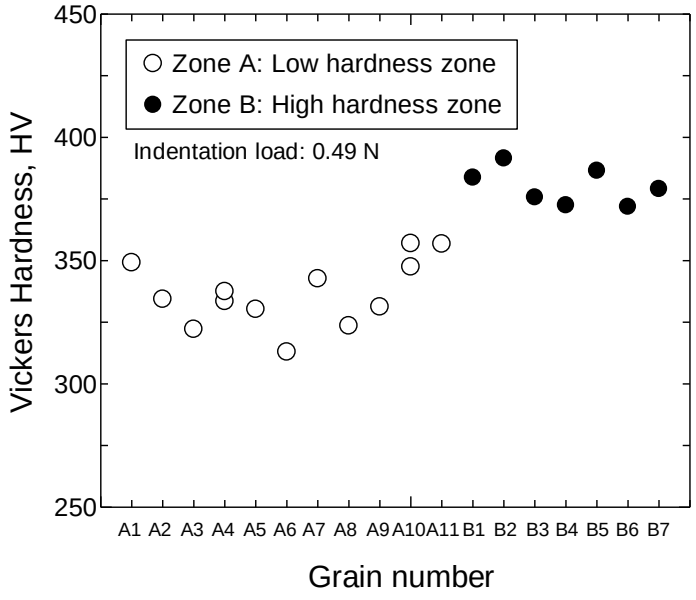

Fig. 5 Vickers hardness distribution of SUH660 steel.

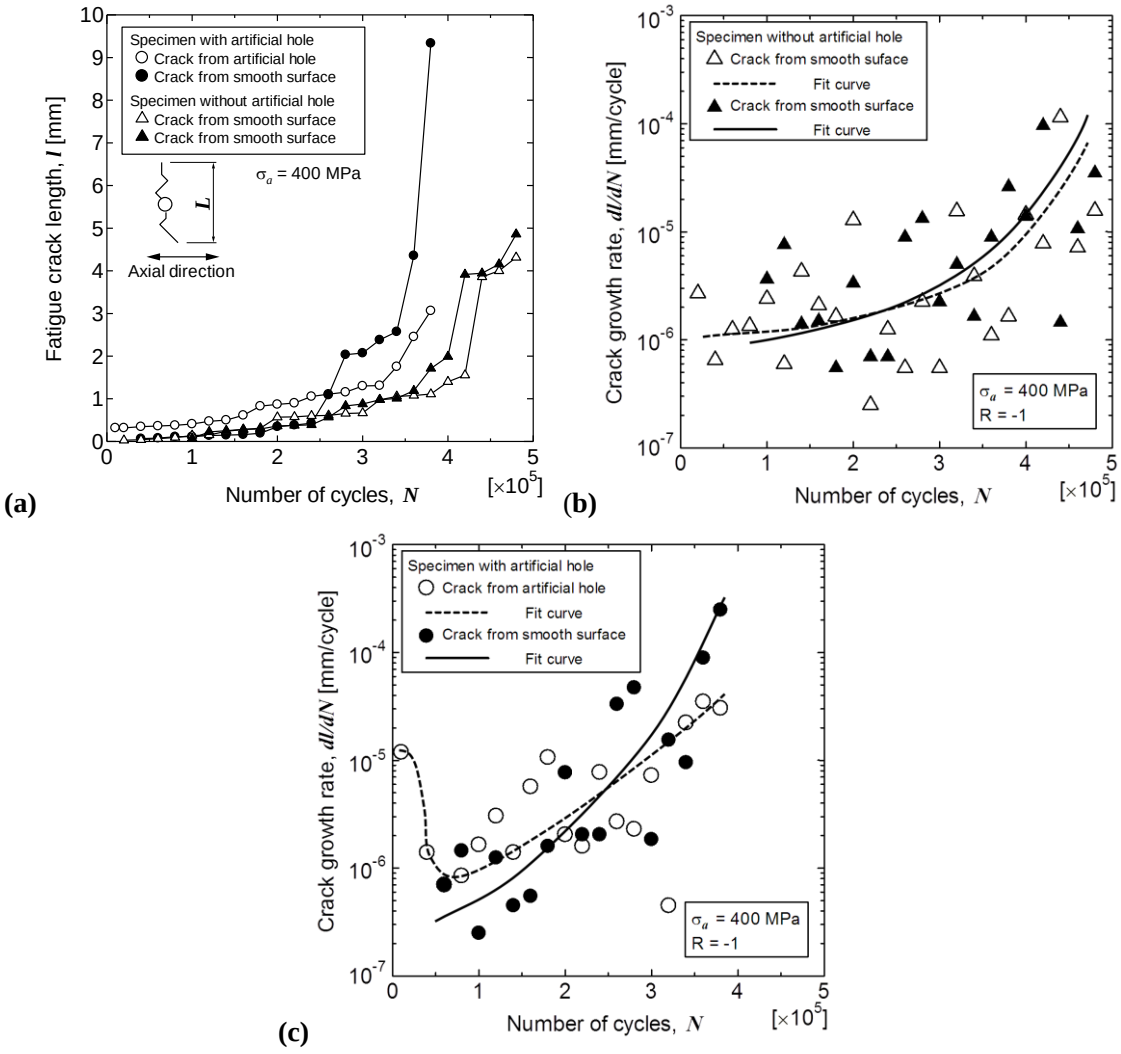

Fig. 6 Fatigue crack growth behavior at σ_a = 400 MPa: (a) crack growth curve;

(b) crack growth rate of specimen without artificial hole;

(c) crack growth rate of specimen with artificial hole.

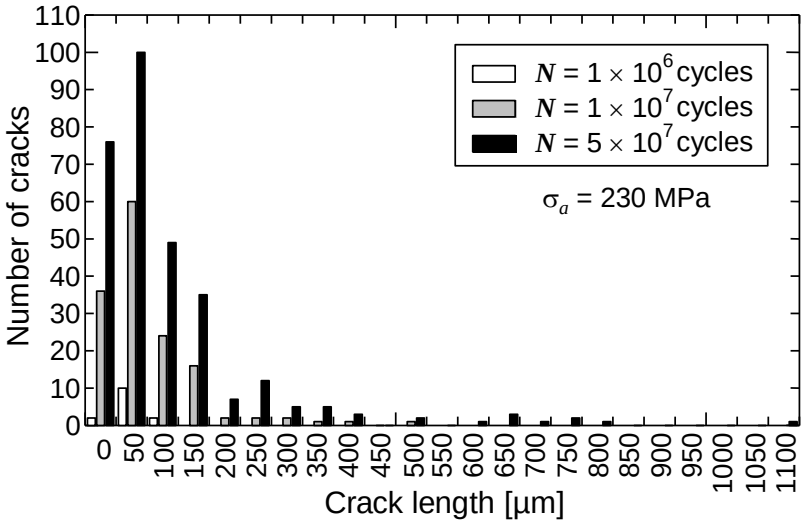

Fig. 7 Fatigue crack length distribution (σ_a = 230 MPa).

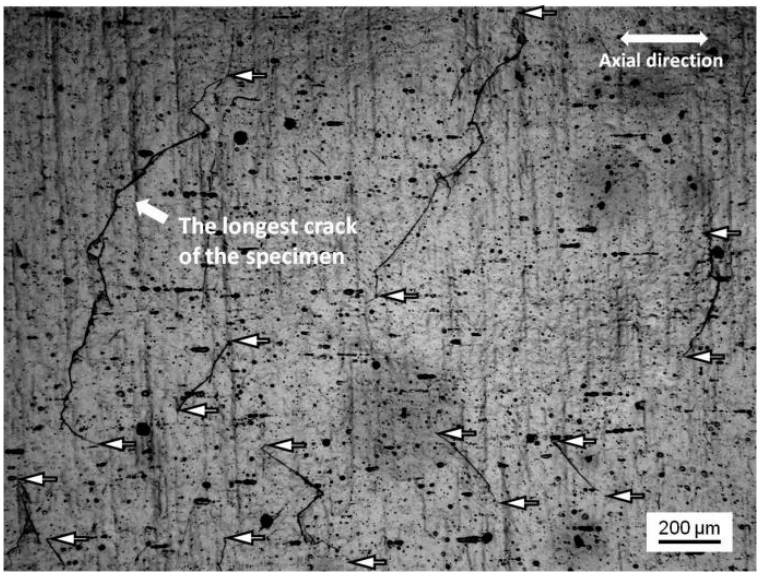

Fig. 8 Crack distribution on surface of SUH660 steel (the arrows indicate the crack tips)

(σ_a = 230 MPa, N = 6.0 × 10^7 cycles).

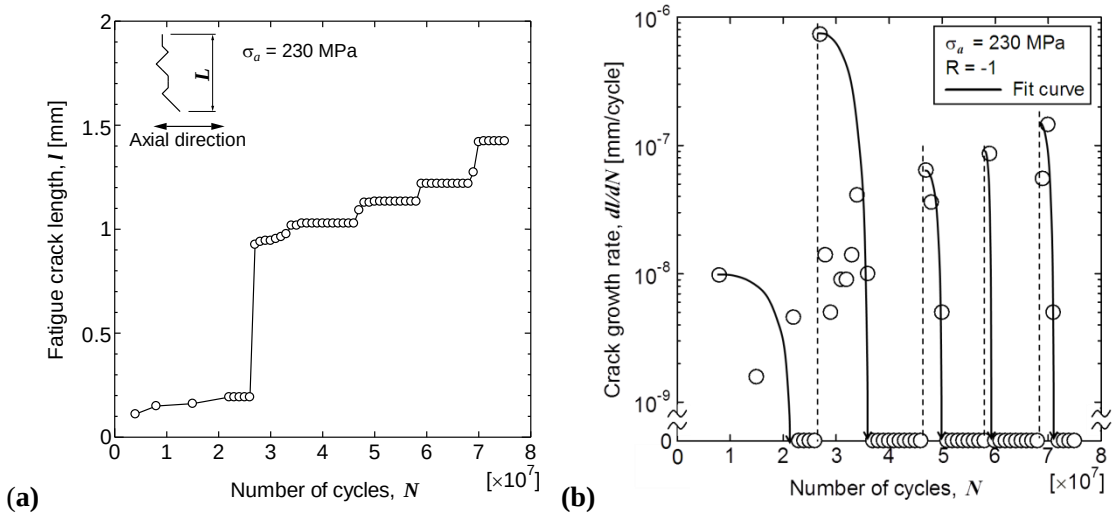

Fig. 9 Fatigue crack growth behavior at σ_a = 230 MPa: (a) crack growth curve; (b) crack growth rate.

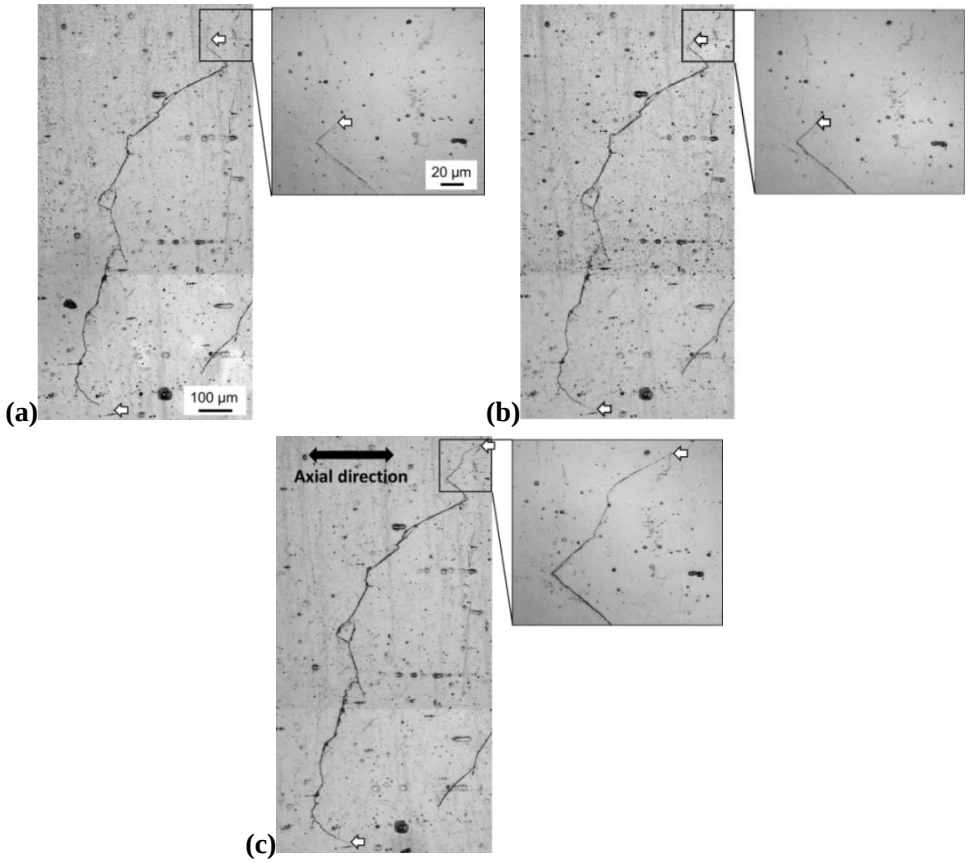

Fig. 10 Crack growth behavior (the arrows indicate the crack tips) (σ_a = 230 MPa): (a) $N = 4.8 \times 10^7$ cycles; (b) $N = 5.8 \times 10^7$ cycles; (c) $N = 5.9 \times 10^7$ cycles.

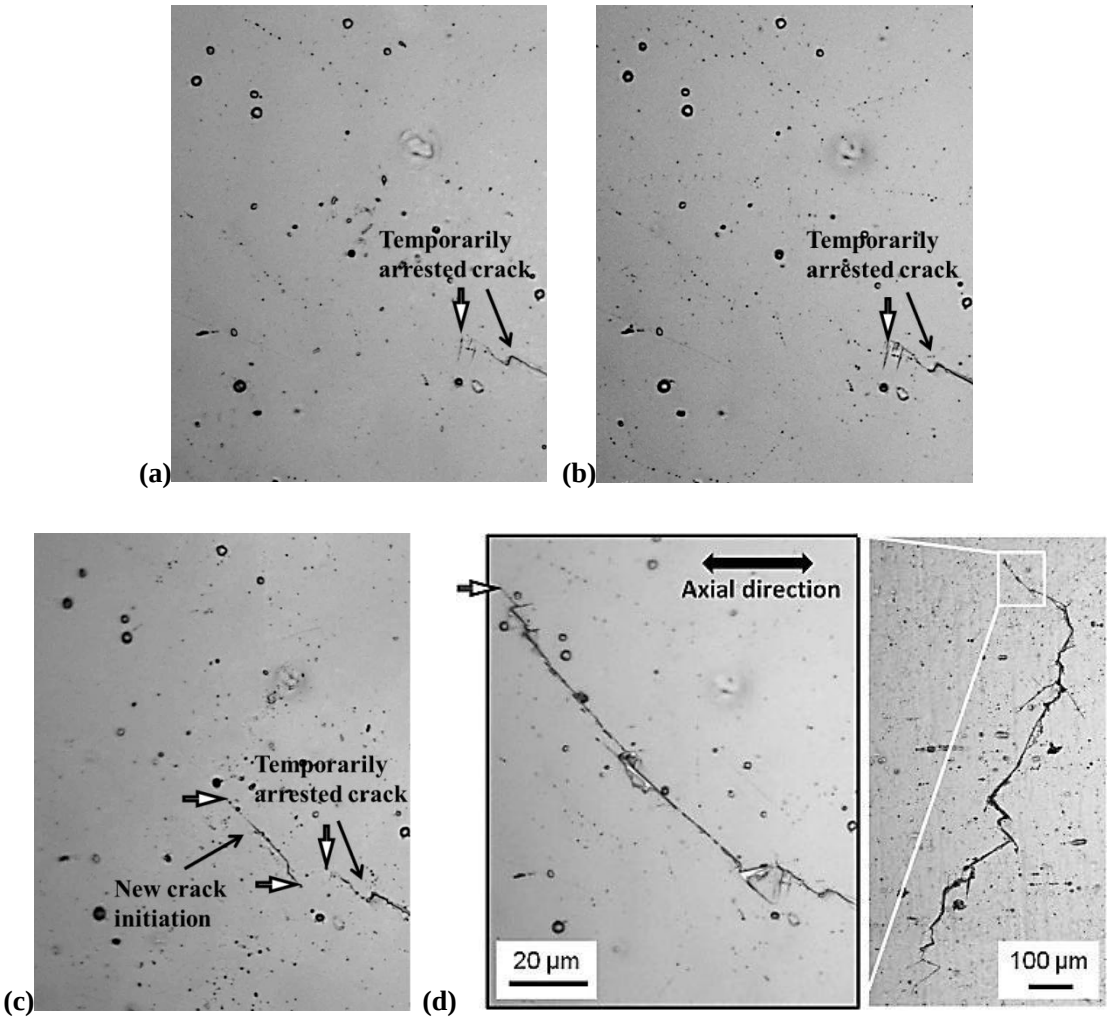

Fig. 11 New crack initiation behavior near the tip of the temporarily arrested crack (the arrows indicate the crack tips) (σ_a = 230 MPa): (a) $N = 6.0 \times 10^7$ cycles; (b) $N = 6.3 \times 10^7$ cycles; (c) $N = 6.4 \times 10^7$ cycles; (d) $N = 6.5 \times 10^7$ cycles.

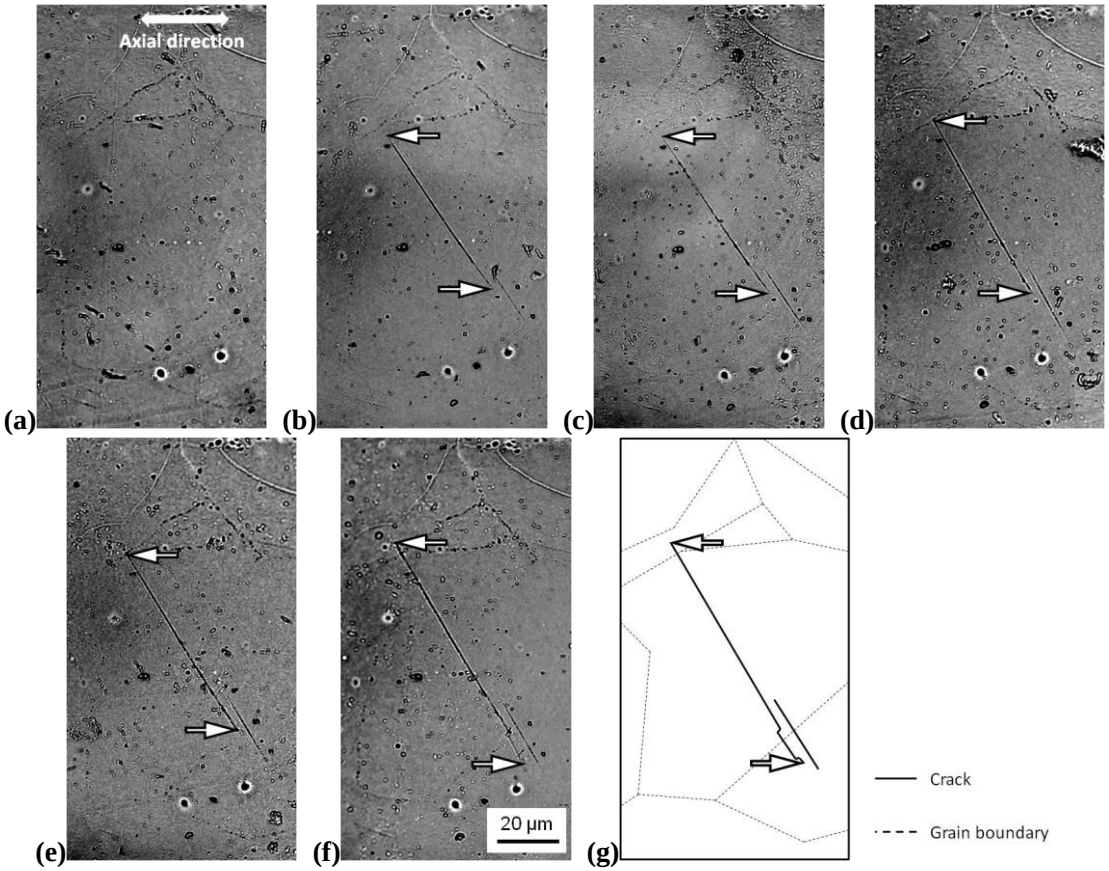

Fig. 12 Crack initiation behavior (the arrows indicate the crack tips) (σ_a = 230 MPa): (a) N = 0; (b) N = 4.0 × 10^5 cycles; (c) N = 6.0 × 10^5 cycles; (d) N = 8.0 × 10^5 cycles; (e) N = 1.0 × 10^6 cycles; (f) N = 1.2 × 10^6 cycles; (g) Schematic diagram of photo at N = 1.2 × 10^6 cycles.

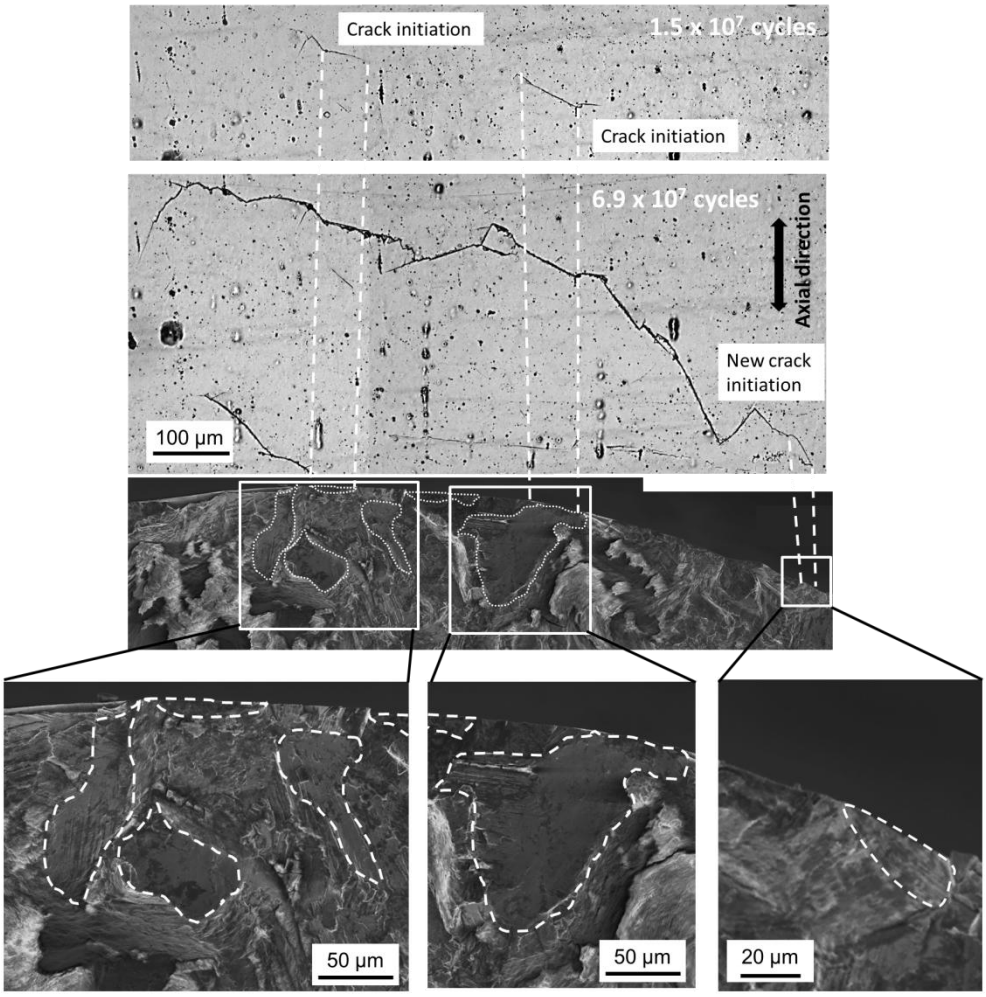

Fig. 13 Corresponding points of the surface crack and the fractured surface (σ_a = 230 MPa).

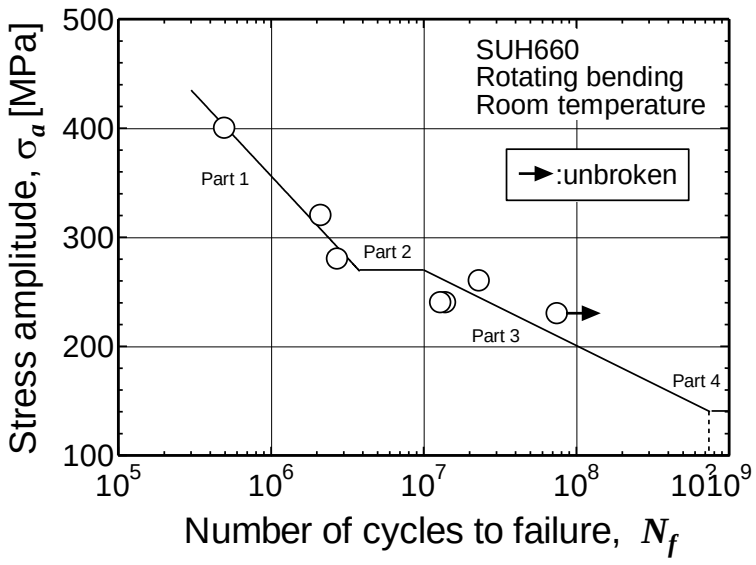

Fig. 14 *S-N* diagram with two "fatigue limits" of SUH660 steel.

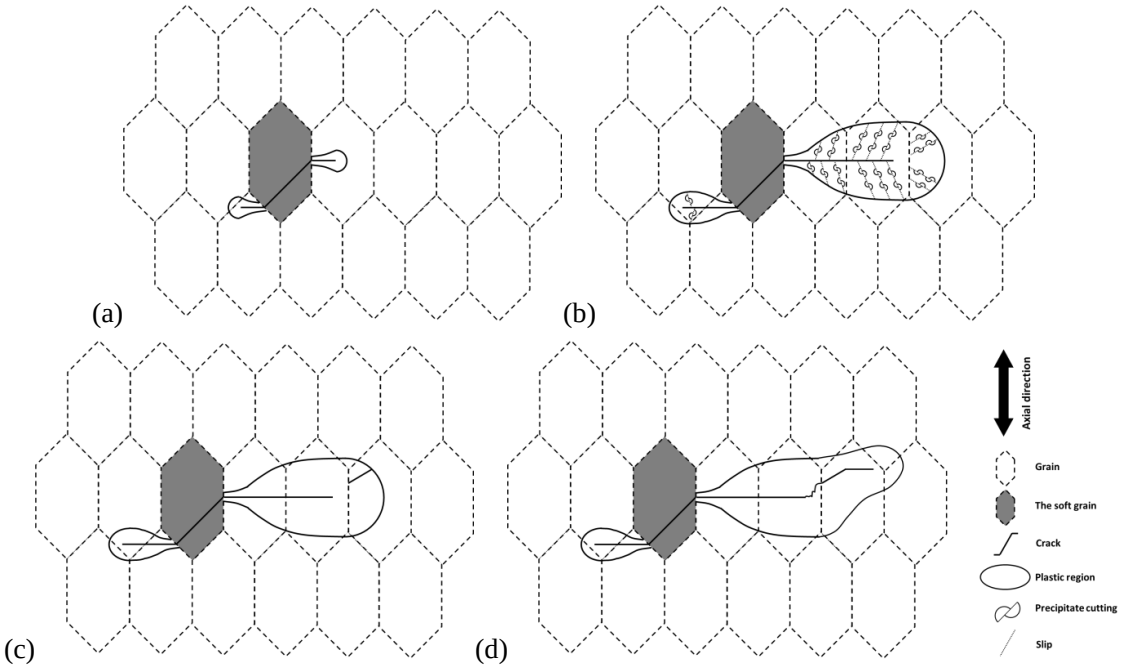

Fig. 15 New crack initiation model near the tip of the temporarily arrested crack at low stress amplitudes.

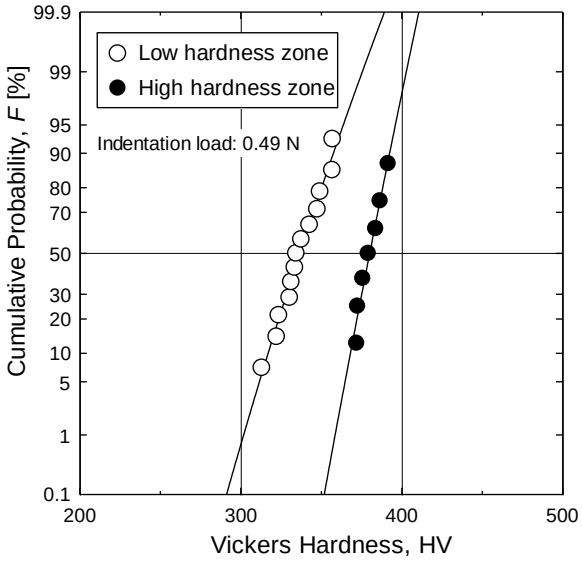

Fig. 16 Normal distribution in low and high hardness zone of SUH660 steel.

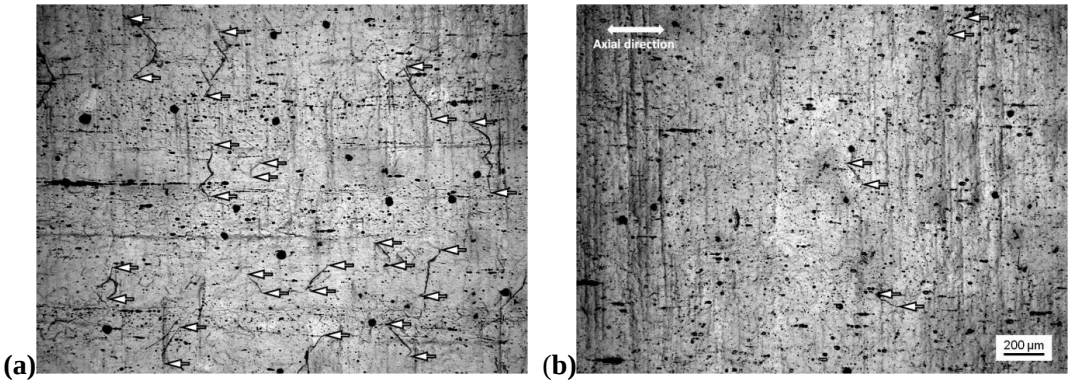

Fig. 17 Crack distribution in SUH660 steel specimen (the arrow indicates the crack tips) (σ_a = 230 MPa, N = 6.0 × 10^7 cycles): (a) many cracks zone; (b) few cracks zone.

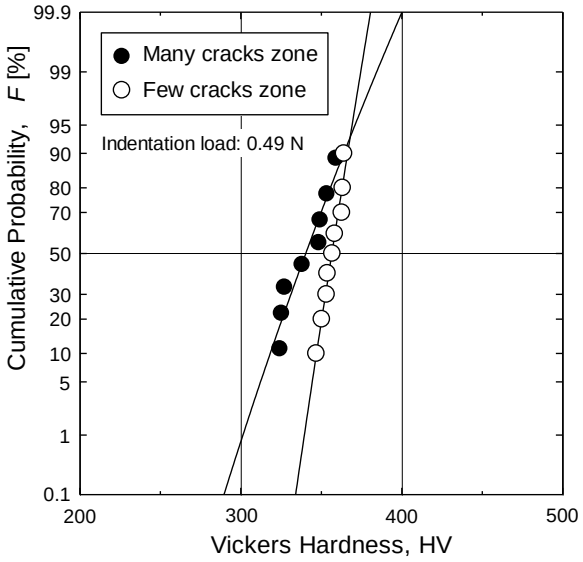

Fig. 18 Normal distribution in many and few cracks zones of SUH660 steel.

Chapter 2.2 Fatigue strength prediction based on Vickers hardness

2.2.1 Introduction

When predicting a fatigue limit using the equations by Murakami et al. [1, 2], Vickers hardness is measured and used; however, the following two questions arise. (1) What load should be used for the Vickers hardness measurement? (2) Which of the varying measured values should be used? In the present paper, question (2) is discussed. About question (1), it can be thought that the intrinsic hardness should be measured in a domain about the size of a non-propagating crack because the fatigue limit is the state at which a small crack starts and becomes a non-propagating crack due to plasticity-induced fatigue crack closure. In addition, for SUH660 stainless steel, no inclusion was observed on the crack initiation site [3]. The effect on the intrinsic hardness of the grain boundary, second phase, and inclusion is not discussed.

The intrinsic hardness of a metal should not vary if thermomechanical treatment is performed correctly. However, as a method of evaluating intrinsic hardness, the Vickers hardness, an indenter is pressed into a metal and the resulting plastic deformation is evaluated. In the case of this evaluation, the relationship between the direction of the indentation (or the direction of plastic deformation) and the crystal orientation of a metal varies relative to the plane of the measured specimen, the obtained Vickers hardness varies. Because there are many slip systems in the case of body-centered cubic (BCC) metal, this scatter is small compared to that of face-centered cubic (FCC) metal; however, because there are few slip systems in the case of FCC metal, the scatter in Vickers hardness becomes greater compared to BCC metal. Furthermore, when an inhomogeneous metal has a scatter in its intrinsic hardness, Vickers hardness indicates that scatter. Therefore, the Vickers hardness value used to predict a fatigue limit has not been clarified.

In Chapter 2.1, a very large scatter in Vickers hardness compared to common homogeneous

metals was found in SUH660 stainless steel, and the relationship between this very large scatter in Vickers hardness and a lower fatigue strength ratio compared to carbon steel was confirmed. Therefore, SUH660 stainless steel is an inhomogeneous FCC metal. In this chapter, according to the definition of Vickers hardness and intrinsic hardness of an inhomogeneous FCC metal, the intrinsic hardness distribution of the fatigue specimen is obtained from Vickers hardness distribution in several test zones. Then, the influence of intrinsic hardness of the softest zone on fatigue behavior is discussed to find the *HV* value that can be used to predict the fatigue limit by Murakami's approach [1, 2] for an inhomogeneous FCC metal.

2.2.2 Proposed experimental principle

To determine the influence of the intrinsic hardness of the softest zone on the fatigue limit of an inhomogeneous FCC metal, the average *HV* value of the softest zone should be obtained. However, the location of the softest zone in the specimen is not known, thus the average *HV* value of the softest zone cannot be obtained by an *HV* test. Therefore, to solve this problem, a new experimental procedure for predicting the average *HV* value was developed, which is shown in Fig. 1. In this experiment, a statistical method is used to predict the average *HV* value of the softest zone. Figure 2 shows the fundamental point of view of the intrinsic hardness distribution. For an inhomogeneous FCC metal, the intrinsic hardness and the Vickers hardness are homogeneous within a grain. However in a zone, the intrinsic hardness is homogeneous but the Vickers hardness is inhomogeneous because in an *HV* test, the crystal orientation varies according to the indented direction (or the direction of plastic deformation). When an *HV* test is performed in a test zone, the Vickers hardness distribution is obtained for the test zone, and then the *HV* value of the softest grain in the test zone would be predicted by a statistical method. After *HV* tests in several test zones, the *HV* value of the softest grain in the specimen surface would be predicted by statistics of extreme [4] using the *HV* values of the softest grain in each of several test zones. Meanwhile the average Vickers hardness variability would be obtained from the Vickers hardness variability of the several test zones. Therefore, according to the *HV* value of the softest grain and average Vickers hardness variability of the specimen surface, the Vickers hardness distribution in the softest zone can be obtained, thus the average *HV* value of the softest zone can be predicted.

2.2.3 Experimental methods

In this chapter, SUH660 stainless steel was used as the inhomogeneous FCC metal to predict the fatigue limit. Table 1 shows the chemical composition of SUH660 stainless steel samples. The SUH660 stainless steel samples were solution treated (ST) for 1 h at 980 °C, air cooled, aged (A) 16 h at 720 °C, and then air cooled again.

The *HV* tests were performed on the surface of the SUH660 stainless steel specimen. The indentation load was 0.49 N, and the indentations were made at the center of the grain to avoid any grain boundary effects. The size of the indentation was approximately 15 μm. SUH660 stainless steel is an inhomogeneous FCC metal, and although the Vickers hardness test indicated approximately the same value within a distance of several crystal grain sizes from the first measurement position, measurement positions located 1 mm or more from each other had significantly different *HV* values. The intrinsic hardness varied on the surface of SUH660, whereas carbon steel, which is a homogeneous FCC metal, has a constant intrinsic hardness. To discuss the intrinsic hardness scatter, which depends on the measurement position, a region of 600 × 450 μm was then defined as a zone, which is the size of the field of view of the 200× optical microscopes used in this chapter. Figure 3 shows the microstructure of a zone on the test specimen surface. The maximum grain size was approximately 200 μm. In Fig. 3, 65 grains were observed in a zone, which meant that the cumulative probability of 1/65 (or ~1.5%) was the smallest *HV* grain in a zone. Because the area of a zone was 0.27 mm^2 (270,000 μm^2), and the area of the fatigue specimen surface was 188 mm^2, the fatigue specimen surface could be divided into 698 zones.

2.2.4 Results and Discussions

2.2.4.1 Intrinsic hardness and Vickers hardness variability

Slip in FCC metal is more difficult than that in BCC metal because the slip system of FCC metal is 12, which is less than the slip system of BCC metal (i.e., 48) [5]. Moreover, the stacking fault energy of FCC metal is lower than that of BCC metal, which means for FCC metal, the cross slip is more difficult than for BCC metal [6]. Therefore, in an *HV* test, plastic deformation of FCC metal is considered more difficult than BCC metal under the same conditions. However, the Vickers hardness of a metal is variable because although the indented direction (or the direction of plastic deformation) in an *HV* test is constant relative to the measured specimen surface, the crystal orientation of each grain in the measured specimen varies. The Vickers hardness is largest when the slip direction of the crystal is perpendicular to the direction of maximum shear stress caused by the indentation, and the Vickers hardness is smallest when the slip direction of the crystal is parallel to the direction of maximum shear stress. For FCC metal, the influence of crystal orientation is more pronounced compared to BCC metal, which has a lower slip system. Therefore, for FCC metal, Vickers hardness variability is greater than for BCC metal.

Figure 4 shows the Vickers hardness distribution in 5 test zones of the SUH660 stainless steel specimen. The *HV* data for 5 zones were plotted on a normal probability scale, and the Vickers hardness distribution in each test zone followed a normal distribution as reported by Sakai et al. [7]. In Fig. 4, the slope of the best-fit line represents the Vickers hardness variability. Because the crystal orientation of each grain varies relative to the indented direction, the *HV* value varies. The line spacing among the best-fit lines of each zone represents different intrinsic hardness values for every test zones on the specimen surface, which indicates intrinsic hardness variability due to the different levels of plastic deformation resistance of each zone. Then, Vickers hardness and intrinsic hardness are both variable in an inhomogeneous FCC metal, which is different from homogeneous FCC metal

in which only Vickers hardness variability can be found.

In *HV* test, the defined zone is the measurement region used to predict the intrinsic hardness of the softest region, does not represent the actual region of homogeneous hardness. Thence, there is a possibility that, multiple regions of homogeneous hardness may exist in a zone, and their respective intrinsic hardness may affect the Vickers hardness variability in a zone. For adjacent regions of homogeneous hardness, if their intrinsic hardness change is nonlinear, the *HV* data of grains in the zone are bound to have large scatter, and its fit line cannot maintain continuous line in the normal probability scale. However, in Fig. 4, the hypothetical situation does not appear, the *HV* change renders linearly in each test zone. Therefore, in SUH660 steel, the distribution of intrinsic hardness is considered to be linear, and have little effect on the Vickers hardness variability in a zone.

2.2.4.2 Hardness and fatigue behavior

For a homogeneous FCC metal in which all zones have the same intrinsic hardness, when the fatigue test stress is below the fatigue limit, the crack is non-propagating due to plasticity-induced crack closure [8]. Therefore, plastic elongation of the plastic region in the tensile direction is considered to affect crack non-propagation. In the plastic zone near the crack tip, each grain has a different *HV* value, which means each grain has a different slip direction, so when fatigue test stress is loaded, the plastic deformation amount of each grain in the plastic zone near the crack tip is different, and the plastic strain on each grain in the tensile direction would be different after the fatigue stress is unloaded. Then different *HV* values cause different plastic strain in the tensile direction. Considering the dimensions of a non-propagating crack and a crystal grain, some crystal grains are thought to influence a non-propagating crack. However, because a crack propagates in three dimensions, there are more grains with different *HV* values than expected in the plastic region of a non-propagating crack, and the Vickers hardness distribution can be found in the plastic region. Thus the Vickers hardness distribution in the plastic region would result in a plastic strain distribution in plastic region, and if all grains in plastic region have the same average *HV*, all grains have same average plastic strain. Then, total plastic elongation of a plastic region that has a plastic strain distribution is considered to be the same as a plastic region that has an average plastic strain due to an average *HV* value. Thus the average *HV* in a plastic region affect residual stress leads to crack closure. Moreover, the Vickers hardness distribution in a plastic region follows a Vickers hardness distribution in the specimen surface. Therefore, the mean value of the Vickers hardness distribution in the specimen surface can be used to predict the fatigue limit by Murakami's approach [1, 2] for homogeneous FCC metals.

However, Vickers hardness and intrinsic hardness are both variable in an inhomogeneous FCC metal, which is different from a homogeneous FCC metal which only has Vickers hardness

variability. For an inhomogeneous FCC metal, the mean value of the Vickers hardness distribution in a specimen cannot be used to predict its fatigue limit. In Chapter 2.1, the author found that for SUH660 stainless steel, specimen surfaces with both few and many crack zones were observed for low stress levels amplitude, and the intrinsic hardness of the zones with many cracks was lower than that of the zones with few cracks. Therefore, in an inhomogeneous FCC metal, cracks initiate and propagate easily in the soft zone where the resistance to plastic deformation is small, and the soft zone greatly affects the fatigue limit of an inhomogeneous FCC metal. In an inhomogeneous FCC metal, the intrinsic hardness in a zone is homogeneous, thus the Vickers hardness distribution in a plastic region, which affects the residual stress that leads to crack closure, follows the Vickers hardness distribution in the softest zone where non-propagating cracks initiate. Therefore, the mean value of the Vickers hardness distribution in the softest zone where non-propagating cracks initiate can be used to predict the fatigue limit by Murakami's approach [1, 2] for an inhomogeneous FCC metal.

2.2.4.3 The fatigue strength prediction for an inhomogeneous FCC metal

In this section, SUH660 stainless steel was used as the inhomogeneous FCC metal to predict the fatigue limit. In Chapter 2.1, the author found that, for SUH660 stainless steel, the temporarily arrested crack behavior below the fatigue strength at 10^7 cycles is primary caused by the plasticity-induced crack closure, the same as for carbon steel below the fatigue limit. Therefore, the fatigue strength at 10^7 cycles can be predicted as the fatigue limit for SUH660 stainless steel by Murakami's approach [1, 2], which is shown in Eq. (2).

In the following, σ_w is the predicted fatigue strength at 10^7 cycles for SUH660 stainless steel, and *HV* is the mean value of the Vickers hardness distribution in the softest zone according to Section 2.2.4.2. To obtain the intrinsic hardness distribution from the Vickers hardness distribution, the definitions of Vickers hardness and intrinsic hardness must be considered. According to Section 2.2.4.1, the lowest *HV* in a zone means the slip direction of the crystal is almost parallel to the direction of maximum shear stress caused by the indentation, and it represents the level of resistance to plastic deformation, which has the same definition as intrinsic hardness. Therefore, the lowest *HV* value in the test zone can be considered as the intrinsic hardness in the *HV* test zone. Figure 5 shows the intrinsic hardness distribution according to the *HV* data of 5 test zones. Figure 5(a) shows the same normal probability scale of the *HV* data as Fig. 4. In Fig. 5(a), the best-fit line for each test zone intersects with the horizontal axis of cumulative probability at 1.5%; the point of intersection presents the lowest *HV* (or intrinsic hardness) in each test zone. Then, the intrinsic hardness data from each test zone were plotted on extreme-value probability scale, which is shown in Fig. 5(b). There are 698 zones on the specimen surface, and the softest zone has the lowest intrinsic hardness value of the 698 zones. Therefore, in the extreme-value probability scale of the intrinsic hardness distribution, when the return period T = 698, which means that in the 698 zones on the specimen surface, the lowest intrinsic hardness value in the softest zone would be 256 *HV*. However, although

the lowest intrinsic hardness value in the softest zone is obtained by statistical prediction, the Vickers hardness distribution in the softest zone cannot be obtained by an *HV* test because we do not know which zone is the softest zone on the specimen surface. According to the slope of the best-fit line for each test zone, the Vickers hardness variability of the test zones does not differ much because the crystal orientation distribution in the zones does not differ much within the same FCC metal specimen. Therefore, the average slope of the best-fit lines for the 5 test zones can be used as the Vickers hardness variability of the softest zone. Figure 6 shows the Vickers hardness distribution in the softest zone using the average Vickers hardness variability. In Fig. 6(a), the average slope of the best-fit line is obtained according to the best-fit lines for the 5 test zones. Fig. 6(b) shows a normal probability scale of Vickers hardness distribution in the softest zone. From Fig. 6(b), the mean value of Vickers hardness distribution in the softest zone is 276 *HV*.

Another parameter of Murakami's approach is $\sqrt{area}$. According to Murakami [1, 2], the $\sqrt{area}$ is originally defined as a square root of the area obtained by projecting a small artificial hole, which becomes the fatigue crack initiation site, onto a plane perpendicular to the first principal stress. A fatigue crack which begins to propagate from the small artificial hole is mainly affected by plasticity-induced fatigue crack closure which is caused by plasticity-induced residual stresses. Then, the fatigue crack is considered to stop after some propagation, when the applied cyclic stress is below the fatigue crack non-propagation limit. For a metal with nonmetallic inclusions, when a crack is initiated at the interface between the inclusion and the matrix, or a crack originates through cracking of the inclusion, then the stresses within the inclusion are relieved, and the inclusion domain may be regarded as mechanically equivalent to a stress-free defect or pore [2]. According to data for some type of hard metals which have nonmetallic inclusions, Murakami [2] showed a modified *S*-*N* curve to express the relationship between the ratio of the experimental fracture stress

amplitude at the inclusion location, σ', to the predicted fatigue limit at the inclusion location in consideration of the inclusion, σ_w', and the cycles to failure, N_f. In most specimens, the values of σ'/σ_w' are greater than 1.0 and within +20% range of 1.0 around 10^7 cycles fatigue life, except in two cases which are below but very close to 1.0. It is considered that the +20% range scatter band is not caused by an error or a variation, but by the effect of the nonmetallic inclusion on the fatigue strength which can be named a correction factor. Because every nonmetallic inclusion may cause a different value of correction factor, it is difficult to calculate correction factors for every hard metal with inclusions. Therefore, the fatigue limit, which is predicted from the maximum inclusion's $\sqrt{area}$ without the correction factor, can be regarded as the safe side value of the fatigue limit for a hard metal with nonmetallic inclusions. This is the reason that the inclusion size can be used for fatigue limit prediction on the safe side.

Following the Murakami's approach of a fatigue limit prediction by its inclusion size, in an SUH660 plain specimen, the initial crack size is suggested to be used for the fatigue limit prediction. Figure 7 shows an example of a crack initiation, propagation, and temporary crack arrest. In the SUH660 plain specimen, the crack easily propagates by Mode II and mixed Mode. Figure 8 shows the crack growth rate from the initiation to the temporary crack arrest, the crack is shown in Fig. 7. The crack growth rate becomes faster and faster once the crack is initiated, then slows down after the crack length, l = 295 μm, the crack coalesces with another crack at l = 517 μm, and the crack stops to propagate when the crack length reaches l = 539 μm. In this case, the crack whose length is 295 μm can be regarded as the initial crack. Then, residual stress which occurred by the fatigue crack propagation from the initial crack, is considered to cause the temporary crack arrest by plasticity-induced fatigue crack closure, like as from the artificial hole. Because of the similar crack behavior which is mentioned above, the initial crack can be used to predict the fatigue limit with Murakami's approach.

Figure 9 shows the scanning electron microscope (SEM) images of fracture surfaces at σ_a = 240 MPa, 320 MPa, and 400 MPa. Table 2 shows the $\sqrt{area}$ of the initial crack vs. applied stress level amplitude. From Table 2, the $\sqrt{area}$ of the initial crack is approximately 80.8 μm. Therefore, using Murakami's approach, the predicted fatigue strength at 10^7 cycles of SUH660 stainless steel can be predicted as 272 MPa. Figure 10 shows the actual value ± 10% error and the predicted value in the *S-N* diagram of SUH660 stainless steel. In Chapter 2.1, the author proposed *S-N* diagram with two 'fatigue limits' for SUH660 steel, one is the fatigue strength at 10^7 cycles, the other is safe side of Fatigue limit II. In Fig. 10, the predicted value of the fatigue strength at 10^7 cycles is inside the ± 10% error range. Therefore, for an inhomogeneous FCC metal, the fatigue limit can be predicted using the mean value of the Vickers hardness distribution in the softest zone.

2.2.5 Conclusions

To predict the fatigue limit of an inhomogeneous FCC metal, the difference between the intrinsic hardness and the Vickers hardness and the relationship between hardness and fatigue behavior were discussed. The conclusions are listed below.

(1) Vickers hardness and intrinsic hardness are both variable in an inhomogeneous FCC metal, and Vickers hardness is more variable in FCC metal than in BCC metal.

(2) The mean *HV* affect the level of residual stress leads to crack closure, and cracks initiate and propagate easily in the softest zone of an inhomogeneous FCC metal; therefore, the mean *HV* value of the softest zone can be used to predict the fatigue limit by Murakami's approach for an inhomogeneous FCC metal.

(3) The Vickers hardness distribution in the softest zone can be obtained using a normal probability scale and an extreme-value probability scale. Using the mean value of the Vickers hardness distribution in the softest zone, the fatigue strength at 10^7 cycles of a plain specimen of SUH660 stainless steel, which is an inhomogeneous FCC metal, can be predicted by Murakami's approach.

References

[1] Murakami Y, Endo M. Effects of hardness and crack geometries on ΔKth of small cracks emanating from small defects, in: Miller JK, Rios LDRE. *The Behaviour of Short Fatigue Cracks.* Mechanical Engineering Publications, 1986, p. 275−93

[2] Murakami Y. Metal fatigue: effects of small defects and nonmetallic inclusions. UK: Elsevier; 2002

[3] Wu H, Oshida Y, Hamada S, Noguchi H. Fatigue strength properties of precipitation strengthening stainless steel A286 focused attention on small fatigue crack behavior. *Procedia Engineering*, **10**; 2011, p. 1973−78

[4] Gumbel JE. *Statistics of extremes*. Dover Publications, 2004.

[5] Hashimoto N, Byun ST, Farrell K, Zinkle JS. Deformation microstructure of neutron-irradiated pure polycrystalline metals. *Journal of Nuclear Materials*, **329-333**; 2004, p.947−52

[6] Van der Walt CM. Slip in the B.C.C metals. *Acta Metallurgica*, **17**; 1969, p.393−5

[7] Sakai T, Suzuki M. Distribution characteristics of mechanical properties and correlation between the respective properties on S35C carbon steel. *Journal of Materials Science*, **26**; 1991, p.1755−61

[8] Elber W. The significance of fatigue crack closure. *Damage Tolerance in Aircraft Structures, ASTM STP 486*; 1971, p. 230−42

List of tables and figures

Table 1 Chemical composition of SUH660 samples (wt. %).

C	Si	P	S	Ni	Cr	Mo	Ti	V	Al	Fe	N	B
0.041	0.11	0.003	0.0017	25.4	15.19	1.43	2.23	0.30	0.21	Bal.	0.0012	0.0033

Table 2 $\sqrt{area}$ of initial crack vs. applied stress level amplitude for SUH660 stainless steel

Applied stress level amplitude, σ_a	$\sqrt{area}$
240 MPa	87.6 μm
320 MPa	61.5 μm
400 MPa	93.3 μm
Average	80.8 μm

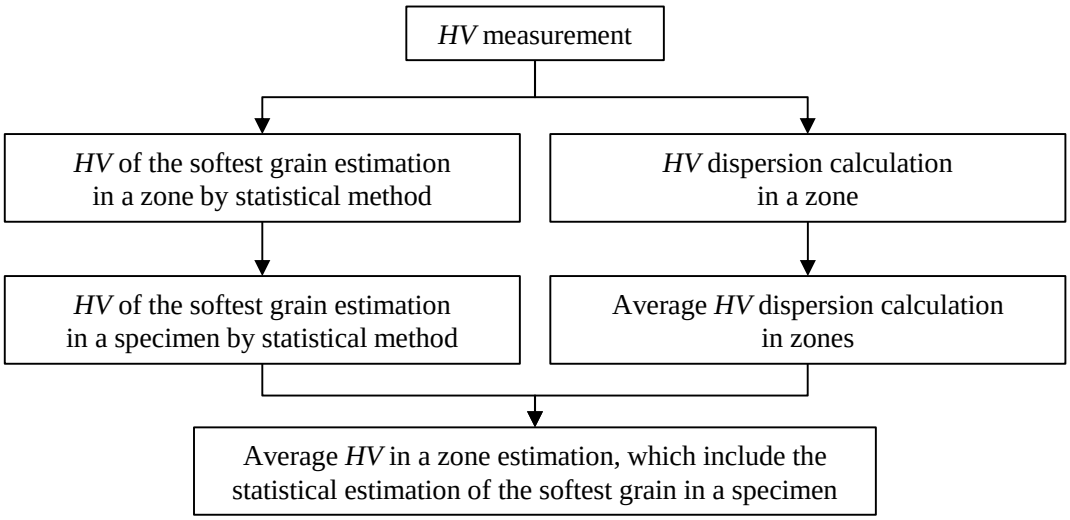

Fig. 1 Experimental procedure for predicting average *HV*

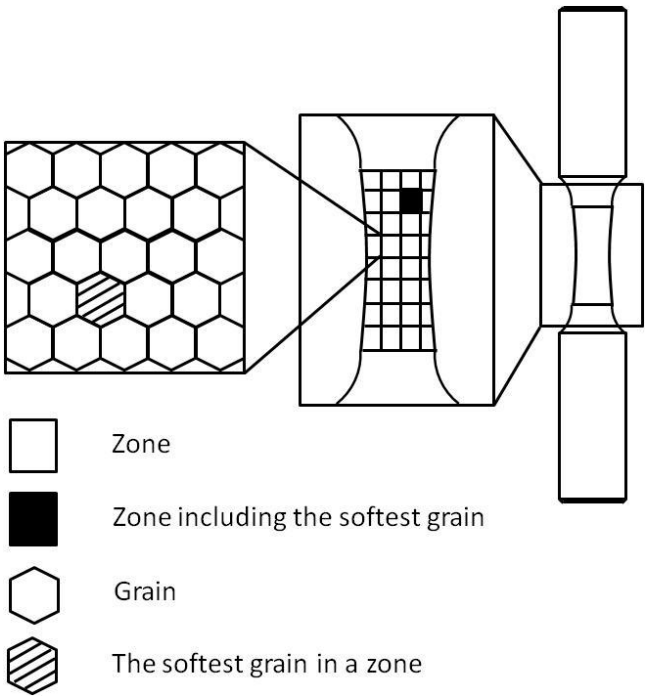

Fig. 2 Fundamental point of view for intrinsic hardness distribution

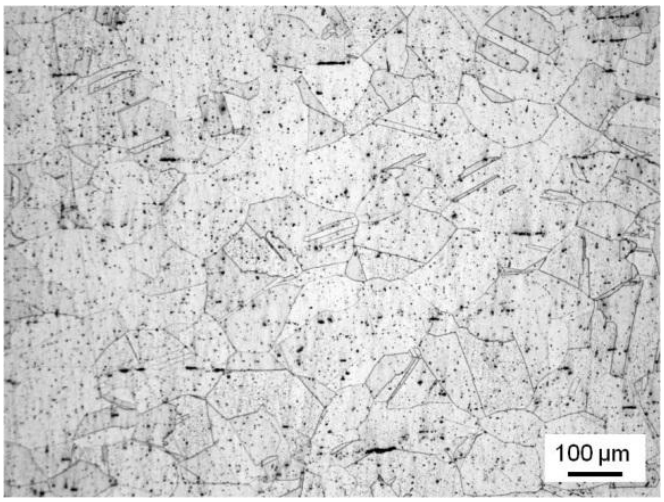

Fig. 3 Microstructure of SUH660 stainless steel

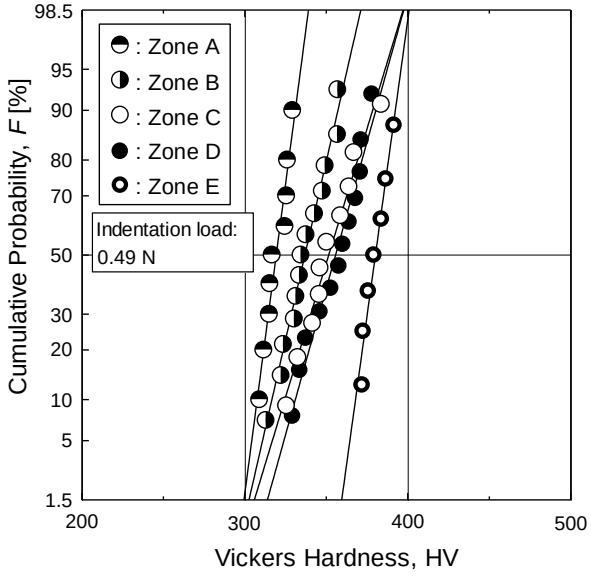

Fig. 4 Vickers hardness distribution of SUH660 stainless steel

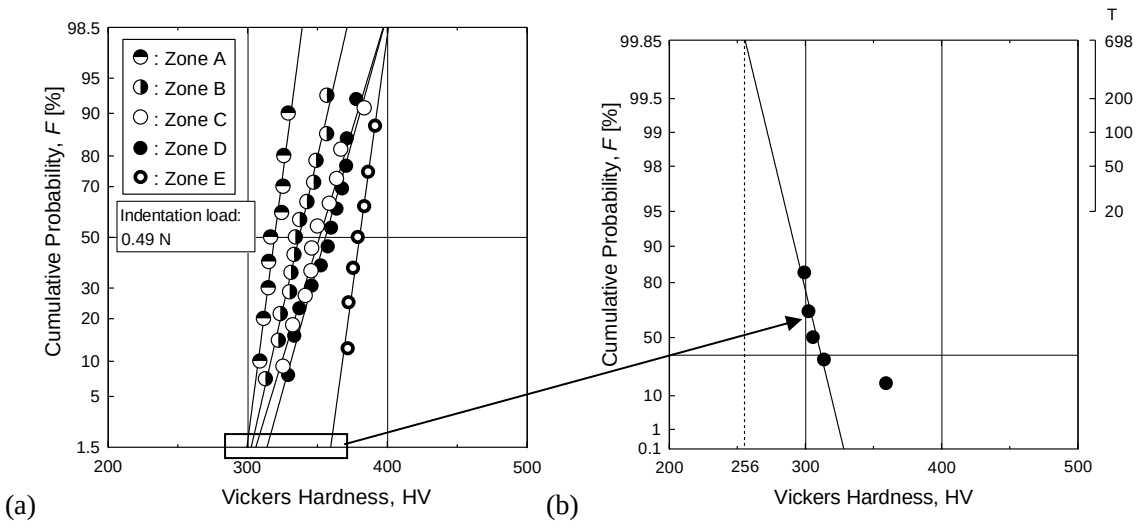

Fig. 5 Vickers hardness distribution and intrinsic hardness distribution of SUH660 stainless steel:

(a) Vickers hardness distribution (normal probability scale);

(b) intrinsic hardness distribution (extreme-value probability scale)

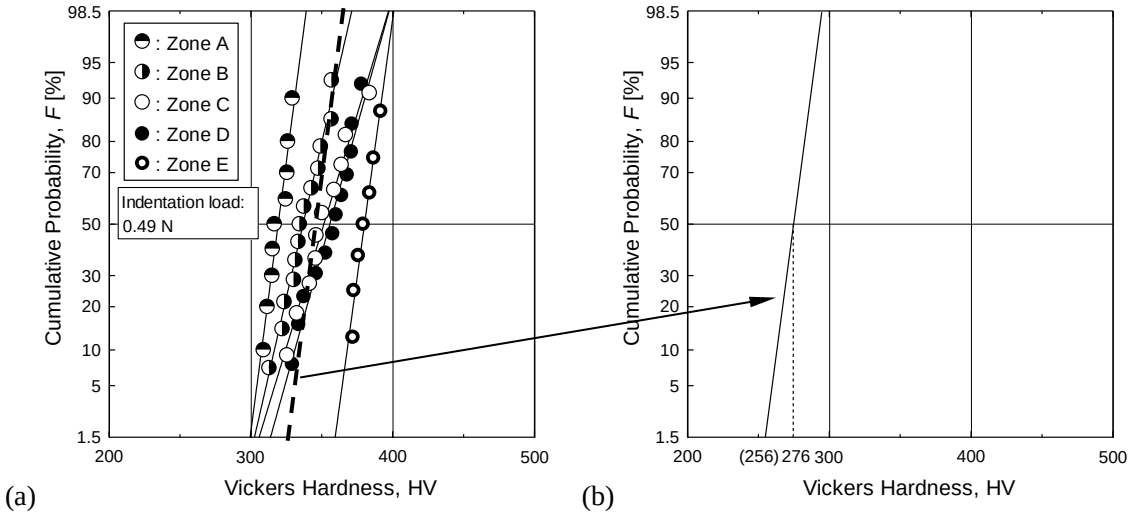

Fig. 6 Vickers hardness distribution of SUH660 stainless steel:

(a) Vickers hardness distribution (normal probability scale);

(b) Vickers hardness distribution in the softest zone (normal probability scale)

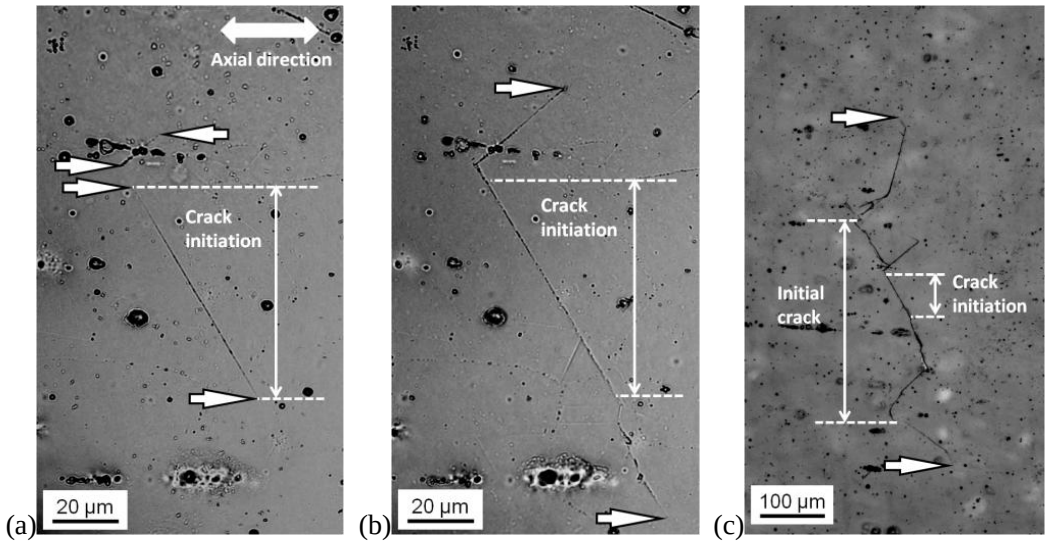

Fig. 7 Initial crack and temporary arrested crack (arrow indicates crack tips) (σ_a = 260 MPa): (a) crack initiation (N = 1.0 × 10^5 cycles); (b) crack propagation (N = 1.1 × 10^6 cycles); (c) temporary crack arrest (N = 6.0 × 10^6 cycles).

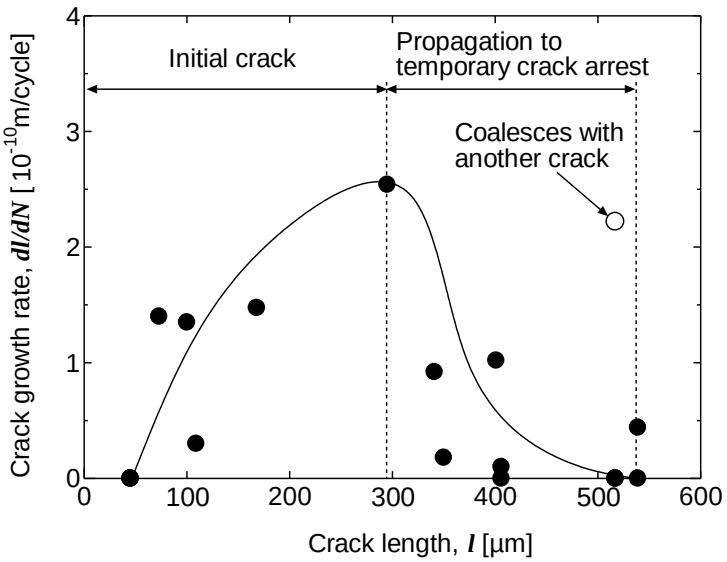

Fig. 8 Crack growth rate from the initiation to temporary crack arrest (σ_a = 260 MPa).

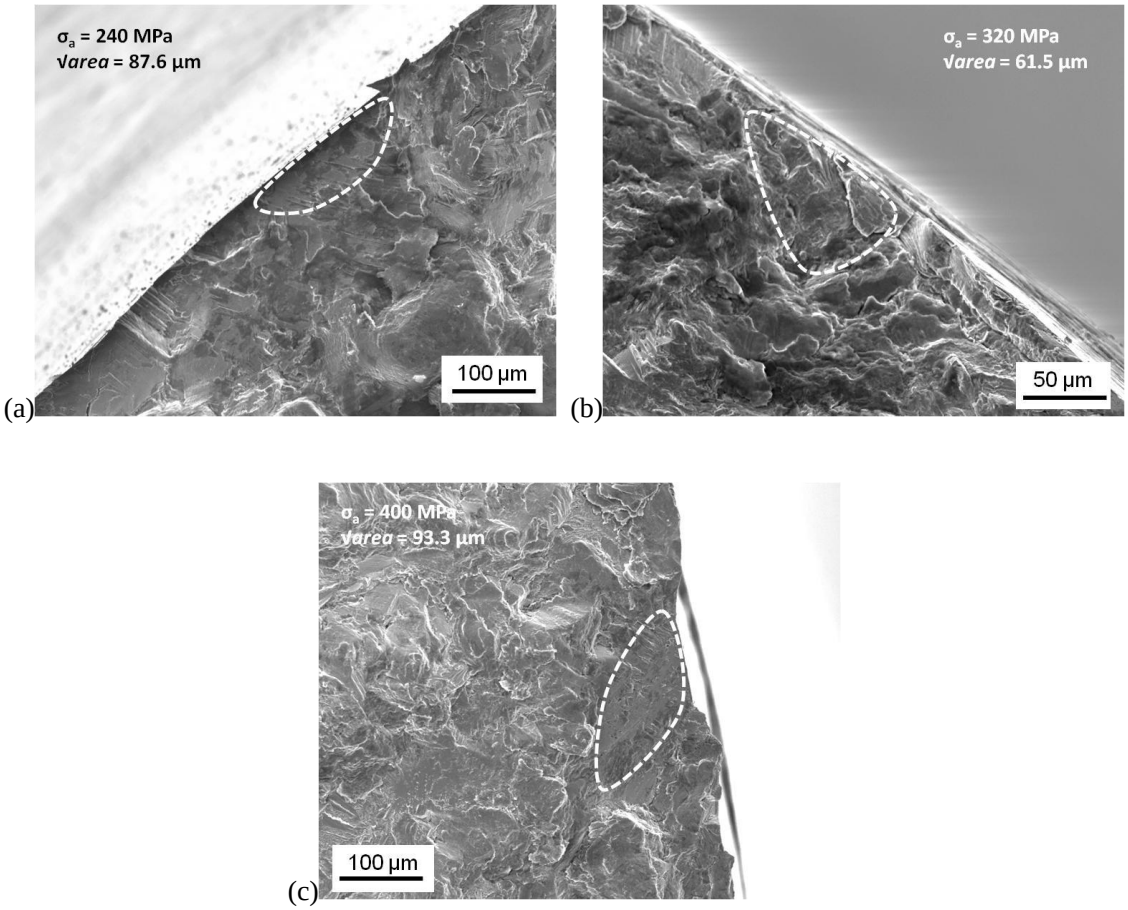

Fig. 9 SEM image of a fractured surface of SUH660 stainless steel

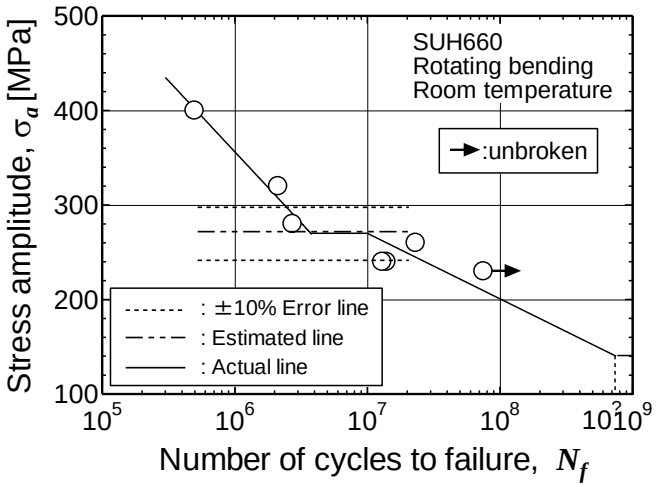

Fig. 10 *S-N* diagram with the estimated line for SUH660 stainless steel

Chapter 2.3 Pre-strain effect on fatigue strength characteristics

2.3.1 Introduction

In the machinery manufacturing industry sector, pre-strain treatment as a method to enhance its strength and fatigue life has been commonly used. Moreover, in the process of machinery manufacturing, work hardening always occurs and affects the service life of product. Therefore, it is particularly important to clarify the effect of pre-strain on fatigue behavior of the material for machinery manufacturing.

SUH660 steel as an iron-based alloy, its fatigue strength is expected to increase due to the pre-strain treatment like carbon steel [1−3]. However, because of its precipitation-hardening strengthening mechanisms, the fatigue strength characteristics may be affected by precipitate cutting in a manner similar to aluminum alloys [4, 5]. Therefore, to ensure the safe use of SUH660 steel, the effect of pre-strain on the steel's fatigue strength characteristics is investigated in this chapter.

2.3.2 Experimental Methods

Both pre-strained and non-strained specimens of SUH660 steel were used in this chapter. Table 1 lists the chemical composition of the steel. The steel samples were solution-treated for 1 h at 980 °C, air-cooled, aged for 16 h at 720 °C, and then air-cooled again. The pre-strained specimens were then compressed by cold rolling to achieve a cross-sectional reduction rate of approximately 10%. The specimen surfaces were buff-polished after machining, and electro-polished to remove the damaged surface layer (10–20 μm).

Tensile and fatigue tests were performed in this chapter. For the tensile tests, an AUTOGRAPH AG-5000 (Shimadzu Corporation) was used. For the fatigue tests, an Ono-type rotating-bending fatigue test machine was used. The fatigue tests were conducted in air at room temperature at a testing frequency of 55 Hz. To observe the microscopic fatigue crack behaviors, the crack length in specimen surface was obtained using the replica method. Figure 1 shows the shapes and dimensions of the tensile and fatigue test specimen.

2.3.3 Results and Discussions

2.3.3.1 Effect of pre-strain on fatigue life

Figure 2 and Table 2 show the tensile test results for the SUH660 steel specimens. The ultimate tensile strength and 0.2% proof stress of the pre-strained specimen were higher than for the non-strained specimen. The fractured tensile specimens shown in Figs. 2(b) and (c) have cup-and-cone fracture that is a ductile fracture, similar to that shown by carbon steel. According to some studies [1−3], the fatigue life and fatigue limit of carbon steel increase with the increase in hardness imposed by pre-strain. For general steel such as carbon steel, pre-strain treatment is considered to cause plastic deformation, which inhibits slip re-generation and enhances fatigue strength. However, for precipitation-strengthened SUH660steel, fatigue strength is not always increased by pre-strain treatment because plastic deformation may cause precipitate cutting.

Figure 3 shows the fatigue test results for SUH660 steel. In contrast to carbon steel at the same fatigue stress amplitude, the pre-strained specimen of SUH660 steel, which had a higher tensile strength than the non-strained specimen, had a shorter fatigue life compared to the non-strained specimen. Figure 4 shows the crack propagation curves of SUH660 steel at σ_a = 400 and 260 MPa. Below σ_a = 400 MPa, the crack initiation life accounts for only a small part of the fatigue life, and the crack propagation life governs the fatigue life. Figure 4(a) shows that the fatigue crack in the pre-strained specimen propagates faster than the crack in the non-strained specimen. For the non-strained specimen, small crack growth dominants the whole fatigue life like as in fatigue specimen of carbon steel, most of fatigue life is spent for the crack growth to 1 mm, and then the crack growth becomes much faster until fracture occurs. However, for a pre-strained specimen, the fatigue crack grows faster than in the non-strained specimen, and more than 50% of fatigue life is spent for the growth of the crack from 1 mm to the final fracture. Thus, the author conclude that pre-strain treatment causes a significant acceleration for crack growth to 1 mm. Figure 5 shows crack

photographs of the pre-strained and non-strained specimens at σ_a = 400 MPa. The fatigue cracks in the pre-strained and non-strained specimens were easily propagated by Mode II or mixed Mode. Thus, there are two possibilities for the reason of the unusual fatigue behavior in pre-strained specimen. The first one is fatigue crack growth only in the specimen surface by Mode II, and causes crack growth acceleration in the diagram. In this possibility, the author surmised that, different from in the specimen for tension-compression fatigue test, the fatigue crack in the specimen for rotating bending fatigue test cannot easily grow as semicircle in inside of the specimen. The other one is precipitate cutting occurs after pre-strain treatment like aluminum alloy, and causes crack growth acceleration. Figure 6(a) shows fracture surface of pre-strained specimen at 400 MPa. Flat and coarse areas are observed around the crack initiation site, and thus crack propagates to 1 mm by not only Mode II but also Mode I. Thus, for the first possibility, when Mode I crack propagating, if the crack grows only in specimen surface, the crack opening displacement at crack initiation site is almost not changed with crack propagating, thus crack tip opening displacement becomes smaller and Mode I crack propagation is inhibited. Obviously, the assumption of fatigue crack growth only in the specimen surface cannot cause crack growth rate increasing but reducing, and the first possibility is impossible. Therefore, the author advocate the second possibility of which precipitate cutting due to pre-strain causes the crack growth acceleration. Figure 6(b) shows fracture surface of non-strained specimens at 400 MPa. Flat areas also can be observed at and near the crack initiation site in non-strained specimen. Compared with the fracture surface of non-strained specimen, although the pre-strained specimen shown in Fig. 6(a) has four flat areas, two more than that for non-strained specimen, the total area that is flat does not greatly changes after pre-strain treatment. Thus, we consider that pre-strain treatment does not promote the mode change of crack growth from Mode I to Mode II in SUH660 steel. Moreover, according to Figs. 6(a) and (b), in both pre-strained and non-strained specimens, the crack length in specimen surface, which corresponding to the zone

contained flat areas, is no longer than 1 mm, thus the author considered that Mode II crack easily propagates when its length less than 1 mm. Figure 7 shows the crack growth rate diagram. For pre-strained and non-strained specimens, below 1 mm of crack length, crack propagates by Mode II or mixed Mode. When the fatigue crack length exceeds 100 μm, the crack growth rate of non-strained specimen slows down first, and then becomes faster and faster after crack length reaches 600 μm. However, the crack growth rate of pre-strained specimen continuously increases with crack propagating once it initiates. Above 1 mm of crack length, crack propagates by Mode I or crack coalescence until fracture, and two type specimens have almost same crack growth rate. In general, when the crack grows from 100 μm to 1000 μm, the Mode II crack growth rate of the pre-strained specimen is approximately 10 times faster than that of the non-strained specimen. These results are similar to those of 6061-T6 aluminum alloy [5], in which precipitates were cut by pre-strain treatment. Therefore, for SUH660 steel, precipitate cutting is considered to be occurred by pre-strain treatment (as in the case of aluminum alloy), and accelerate Mode II crack propagation, thereby reducing the crack propagation life. Moreover, based on the behavior of crack growth rate on plain specimens, the author consider that, although the crack acceleration due to pre-strain shorten the fatigue life, because of the relatively small difference of fatigue life in S-N diagram shown in Fig. 3, the effect of pre-strain on fatigue behavior of a plain specimen can be ignored. However, if the specimen with small defects is used, the effect of crack acceleration on fatigue life is considered to be enlarged and cannot be ignored.

Figure 4(b) shows the fatigue crack propagation curves at σ_a = 260 MPa. The fatigue crack propagates monotonically in the pre-strained specimen; however, in the non-strained specimen, the fatigue crack stops propagating and then starts again, it is called as temporarily arrested crack behavior and has been discussed in Chapter 2.1. According to Chapter 2.1, the temporarily arrested crack behavior below the fatigue strength at 10^7 cycles was mainly caused by plasticity-induced

crack closure. In this chapter, the author consider that pre-strain treatment inhibits slip re-generation and the occurrence of plastic deformation; after that, low-level plastic deformation with crack propagation cannot cause enough residual stress to satisfy crack non-propagation. Moreover, for the pre-strained specimen, precipitate cutting reduces the resistance to dislocation emitting from the crack tip. Therefore, the author considers that crack non-propagation in pre-strained specimen occurs with more difficulty than in the non-strained specimen. This means that the latter has a higher fatigue strength at 10^7 cycles than the pre-strained specimen.

2.3.3.2 Dislocation accumulation model at the crack tip

As described in the previous section, the author reported that, although pre-strain treatment increases the slip resistance for tensile and strengthens yield strength, it no increases the slip resistance for crack propagating but accelerates crack growth. According to the studies of Thompson et al. [6] and Cicco et al. [7], for SUH660 steel, after aged at 600 ~ 730 °C from 1 to 1000 h, the diameter of γ′-phase particles are 10 ~ 20 nm, and hundreds of this particles are distributed in the region of 600 × 600 nm; that is, countless γ′-phase particles existed in every grain and strengthening its strength. Shen et al. [8] reported that dislocation accumulations occurred in the dispersed nano-scale precipitates for precipitation-strengthened material. Bayley et al. [9] reported that dislocation-induced back stress and a stress field were found around the dislocation. Therefore, the author considers that, for precipitation-strengthened materials, the dislocations easily pile up at precipitates, and if precipitate were cut, the dislocation pile up at elsewhere. The effect of back stress on dislocation source increases while dislocation pile up, and thus resists the dislocation generation and movement. Figure 8 shows schematic diagrams of the dislocation accumulation for tensile test. When tensile stress exceeds the yield strength, the monotonic deformation occurs in test section of specimen. Figure 8(a) shows a case of dislocation accumulation in non-strained specimen. Because of the uniform tensile stress exerted on test section of tensile specimen, in the grains, the dislocations generate and pile up at precipitates at first. With the dislocation accumulation, the back stress increases and affect the dislocation generation from dislocation source. Thence, the precipitate strengthens the material by hindering dislocation motion, which inhibits dislocation and slip generation; the yield strength increases. When tensile stress is increasing, dislocations begin to shear precipitates. The sheared precipitates lose their resistance to dislocation motion, and the dislocations pass through the sheared one and pile up at the precipitate beside. Thus, the back stress still increases though the precipitate cutting. As the tensile test progresses, the dislocations finally pile up at grain

boundary. Figure 8(b) shows a case of dislocation accumulation in pre-strained specimen. After pre-strain treatment, although precipitates are sheared, a certain amount of dislocations have generated and accumulated. Thus, the yield strength of pre-strained specimen is larger than non-strained specimen.

According to the relationship between back stress and dislocation movement, the author considers that the back stress effects on the crack tip increase with a greater dislocation accumulation and inhibits crack growth, but decrease with an increase in the distance from the area of a dislocation pile up along the slip plane. Accordingly, the author suggests a dislocation accumulation model at the crack tip for a precipitation-strengthened material, to describe the acceleration of crack growth due to precipitate cutting. Figure 9 shows schematic diagrams of the dislocation accumulation model at the crack tip. Differently from whole plastic deformation in tensile test, local plastic deformation occurs around crack tip in fatigue test. Figure 9(a) demonstrates dislocation movement at the crack tip with precipitates. In the case of the non-strained specimen, many precipitates exist near the crack tip. When the stress is loaded, because of stress concentration at crack tip, dislocations generate from the crack tip and pile up at the precipitates which are very close to the crack tip. Thereafter, the dislocations shear the nearest precipitate and pile up at the precipitate beside. In the stage of the increasing in the stress of tensile direction, the dislocations shear precipitates near the crack tip and pile up at the precipitates beside. However, in the region that little further from crack tip, the shear stress becomes lower and cannot shears the precipitates. Thus, the dislocations finally pile up at the uncut precipitates, and because of their relatively close distance from the crack tip, the back stress on the crack tip is considered to increases very quickly with dislocation accumulation and causes a significant impact on the crack growth rate. Figure 9(b) shows the dislocation movement around the crack tip with precipitate cutting. Because the precipitates in a pre-strained specimen are cut by the pre-strain treatment, the dislocations easily move and pass through the cutting precipitates even in

the region that little further from crack tip with lower shear stress. Thus, in the pre-strained specimen, the dislocations pile up at somewhere much farther from the crack tip, compared with in the non-strained specimen. Because the distance between the crack tip and the dislocation pile up site becomes longer after pre-strain treatment, the author considers that, at the same condition, the back stress effects on the crack tip of the pre-strained specimen increase slowly and it is to be exceeded by the non-strained specimen while the dislocations pile up. Therefore, for the pre-strained specimen, the crack growth acceleration is considered to be caused by precipitate cutting.

Overall, the crack growth rate for SUH660 steel is considered to be affected more by precipitate cutting than by plastic deformation, which is why the non-strained specimen has a longer crack propagation life compared to the pre-strained specimen.

2.3.3.3 Effect of buff-polish on fatigue life

In contrast to pre-strain treatment, which causes plastic deformation and precipitate cutting across an entire SUH660 specimen, buff-polish treatment causes surface strengthening only, also called local plastic deformation. Because the work hardened layer is thin, the author considers it to have little effect on the fatigue characteristics. To evaluate this assumption, buff-polished fatigue specimens without electro-polish treatment were added at 400 MPa and 260 MPa.

Figure 10 shows the results for the buff-polished fatigue specimens, compared to the electro-polished specimen. Figure 10(a) demonstrates that the buff-polish treatment had little effect on crack propagation at 400 MPa in the pre-strained specimen. Because the precipitates had been cut by the pre-strain treatment, the buff-polish treatment only increased the plastic deformation level of the specimen surface. Figure 11 shows the residual stress distribution of the buff-polished specimens. The residual stress measurement in the longitudinal direction was performed using a micro X-ray stress measurement apparatus PSPC-RSF/KM (Rigaku Corporation). To obtain the residual stress distribution in the radial direction, each surface was successively removed (4−8 μm) by electro-polishing. The maximum residual stress exists on the specimen surface and decreases with distance from the surface. Then, the author estimates that the depth of the work-hardened layer is about 30 μm for the pre-strained specimen, and about 15 μm for the non-strained specimen. Therefore, because the depth of the work-hardened layer is very thin compared to the 5 mm-diameter of the fatigue test specimen shown in Fig. 1(b), the small increase in local plastic deformation due to the buff-polish treatment has little effect on crack propagation and fatigue life for the pre-strained specimen. Figure 10(b) shows that the buff-polish treatment also reduced the crack propagation life at 400 MPa for the non-strained specimen. The crack growth rate at 400 MPa is shown in Fig. 12. The fatigue crack of the buff-polished non-strained specimen grew at almost the same rate as for the electro-polished pre-strained specimen. Figure 13 shows a photograph of the fracture surface of the

buff-polished non-strained specimen at 400 MPa. A flat area can be observed in the path of crack growth from the crack initiation site, and within 20 μm from the specimen surface. The Mode II crack growth path within least 20 μm depths from specimen surface covers a 15-μm-deep work-hardened layer of the non-strained specimen. In Section 2.3.3.1, the crack growth acceleration was considered to be caused by precipitate cutting. Therefore, the author considers that as the precipitate cutting occurs in the work-hardened layer due to the buff-polish treatment, the crack growth rate on the specimen surface becomes faster, leading to the crack growth inside of the specimen.

Figure 10(c) demonstrates that the buff-polish treatment enhances the temporary crack non-propagation at 260 MPa for the pre-strained specimen. In Section 2.3.3.1, the effect of pre-strain on plasticity-induced crack closure was discussed, the fatigue strength of SUH660 steel at 10^7 cycles is related to the residual stress. The buff-polish treatment causes local plastic deformation on the specimen surface, thus the residual stress of the work-hardened layer enhances plasticity-induced crack closure and causes temporary crack non-propagation. For the same reason, the residual stress owing to the buff-polish treatment will enhances plasticity-induced crack closure in the non-strained specimen. Figure 10(d) shows the crack growth curves of non-strained specimens at 260 MPa. The temporary crack non-propagation in the buff-polished non-strained specimen occurs earlier than in the electro-polished non-strained specimen. Therefore, the author considers that the buff-polish treatment causes residual stress in the surface and enhances the temporary crack non-propagation occurrence.

2.3.4 Conclusions

To investigate the effect of pre-strain on the fatigue strength characteristics of an SUH660 plain specimen, tensile and fatigue tests were performed. From the results of the experiment, the unusual fatigue behavior of crack growth acceleration due to pre-strain is observed at high stress amplitude, and the author considers the significant effect of pre-strain on the crack growth rate to be related to precipitate cutting. Moreover, the fatigue strength at 10^7 cycles becomes lower after pre-strain treatment, thus the author considers the effect of pre-strain on temporary crack non-propagation to be related to plastic deformation.

Based on the increases of crack growth rate due to pre-strain, a dislocation accumulation model at the crack tip for precipitation-strengthened material was proposed. According to the model, the different fatigue characteristics for the pre-strained and non-strained specimens of SUH660 steel are caused by different locations of dislocation accumulation at the crack tip.

To compare with the effect of pre-strain on fatigue behavior, the fatigue tests using buff – polished specimens were added to investigate the effect of local plastic deformation on fatigue behavior. According to the results of experiment, buff-polish treatment causes cutting of precipitates and residual stress in the work-hardened layer. At high stress amplitude loading, the cutting of precipitates accelerates crack growth in the specimen surface, and thus enhances crack growth inside of the specimen. At low stress amplitude loading, residual stress due to local plastic deformation enhances the plasticity-induced crack closure and the occurrence of temporary crack non-propagation.

References

[1] Frost NE. The effect of cold work on the fatigue properties of two steels. *Metallurgia*, **62**; 1960, p. 85−90

[2] Kage M, Nisitani H. The effect of tensile prestrain on the fatigue strength of strength-anisotropic rolled steel. *Bulletin of JSME,* **20**; 1977, p. 1359−66

[3] Kang M, Aono Y, Noguchi H. Effect of prestrain on and prediction of fatigue limit in carbon steel. *International Journal of Fatigue*, **29**; 2007, p. 1855−62

[4] Al-Rubaie KS, Del Grande MA, Travessa DN, Cardoso KR. Effect of pre-strain on the fatigue life of 7050-T7451 aluminium alloy. *Materials Science and Engineering A*, **464**; 2007, p. 141−50

[5] Ikematsu K, Mishima T, Kang M, Aono Y, Noguchi H. Effect of prestrain on fatigue crack growth of age-hardened Al 6061-T6. *ASTM STP 1508: Fatigue and Fracture Mechanics*, **36**; 2009, p.561−73

[6] Thompson AW, Brooks JA.The mechanism of precipitation strengthening in an iron-base superalloy. *Acta Metallurgica*, **30**; 1982, p. 2197–203

[7] Cicco DH, Luppo IM, Gribaudo ML, Ovejero-García J. Microstructural development and creep behaviour in A286 superalloy. *Materials Characterization*, **52**; 2004, p. 85−92

[8] Shen YF, Wang CM, Sun X. A micro-alloyed ferritic steel strengthened by nanoscale precipitates. *Materials Science and Engineering A*, **528**; 2011, p. 8150–6

[9] Bayley CJ, Brekelmans WAM, Geers MGD. A comparison of dislocation induced back stress formulations in strain gradient plasticity. *International Journal of Solids and Structures*, **43**; 2006, p. 7268−86.

List of tables and figures

Table 1 Chemical composition of SUH660 steel (wt. %)

C	Si	P	S	Ni	Cr	Mo	Ti	V	Al	Fe	N	B
0.041	0.11	0.003	0.0017	25.4	15.19	1.43	2.23	0.30	0.21	Bal.	0.0012	0.0033

Table 2 Mechanical properties results for SUH660 steel

Type	Ultimate tensile strength (σ_U)	0.2% proof stress ($\sigma_{0.2}$)	Elongation (δ)
Non-strained tensile specimen	1065 MPa	664 MPa	27.6%
Pre-strained tensile specimen	1259 MPa	1200 MPa	11.7%

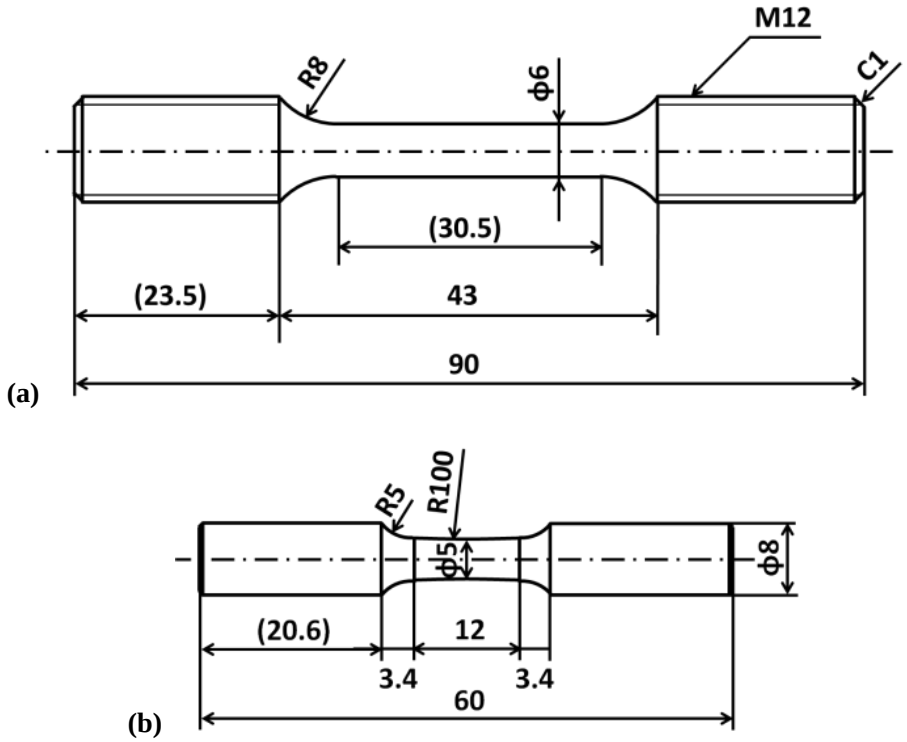

Fig. 1 Shapes and dimensions of specimens (unit: mm): (a) tensile test specimen;

(b) fatigue test specimen.

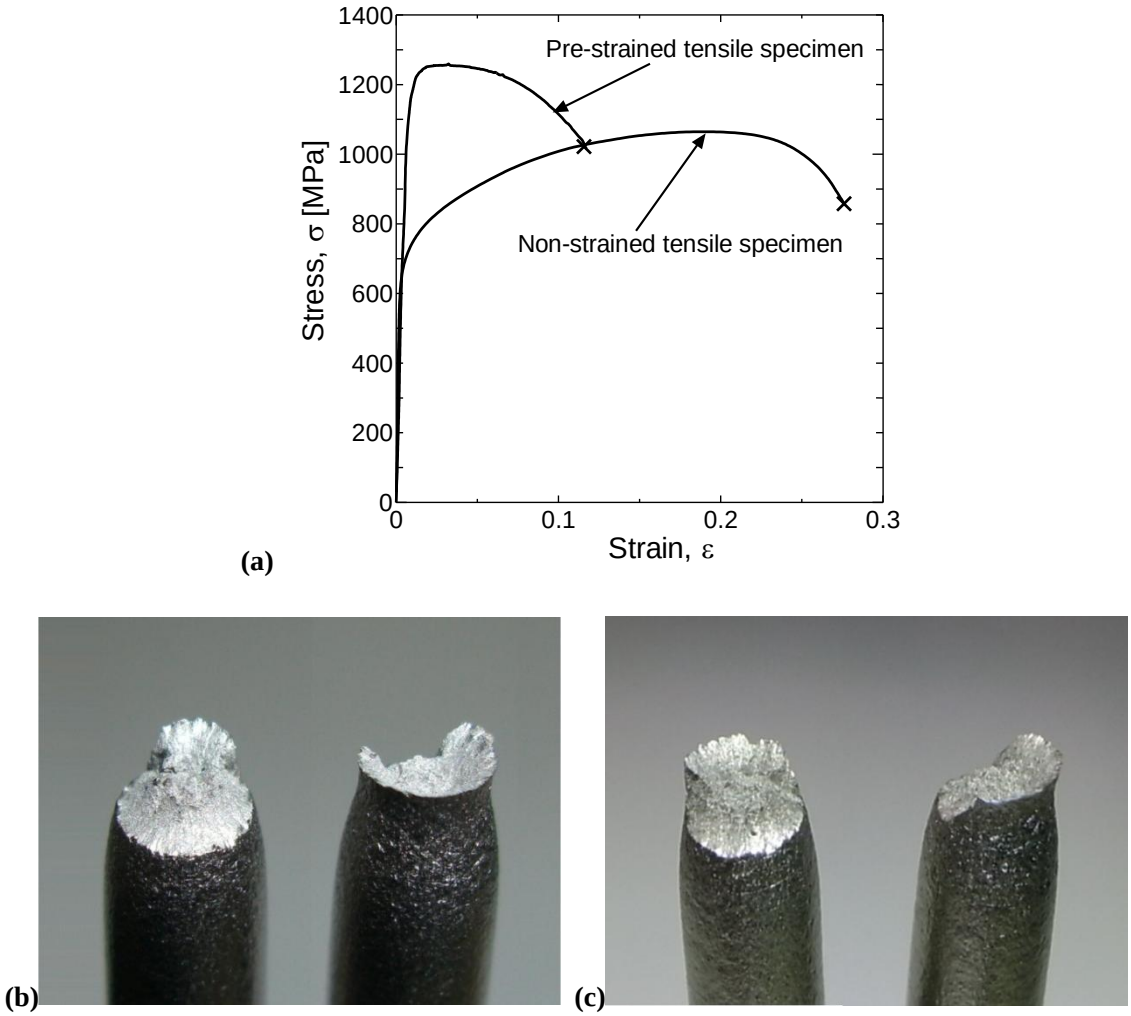

Fig. 2 Tensile test results for SUH660 steel: (a) stress-strain curve;

(b) fractured non-strained tensile specimen; (c) fractured pre-strained tensile specimen.

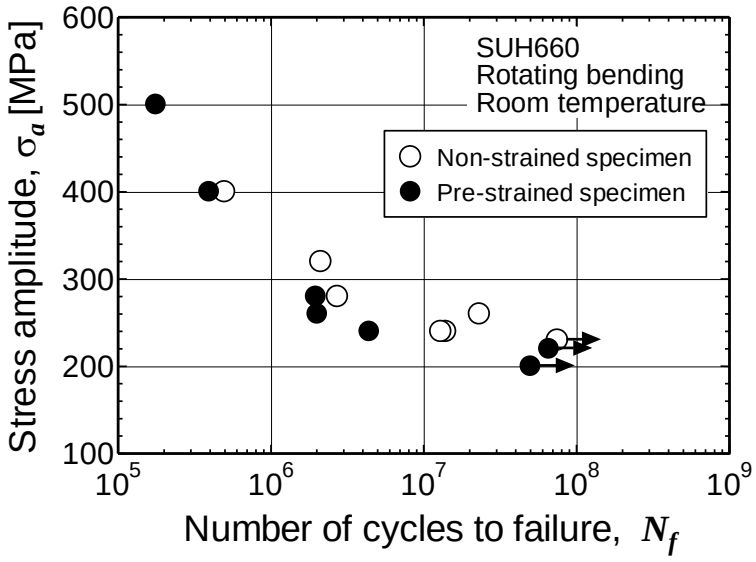

Fig. 3 Fatigue strength of SUH660 steel.

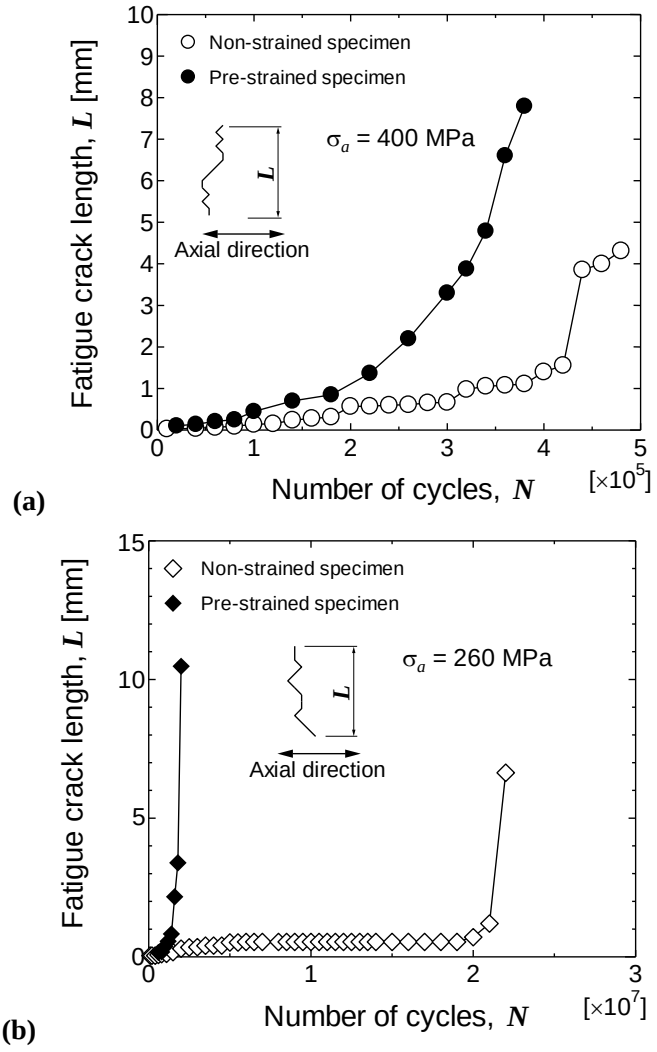

Fig. 4 Crack propagation in pre-strained and non-strained SUH660 specimens: (a) σ_a = 400 MPa; (b) σ_a = 260 MPa.

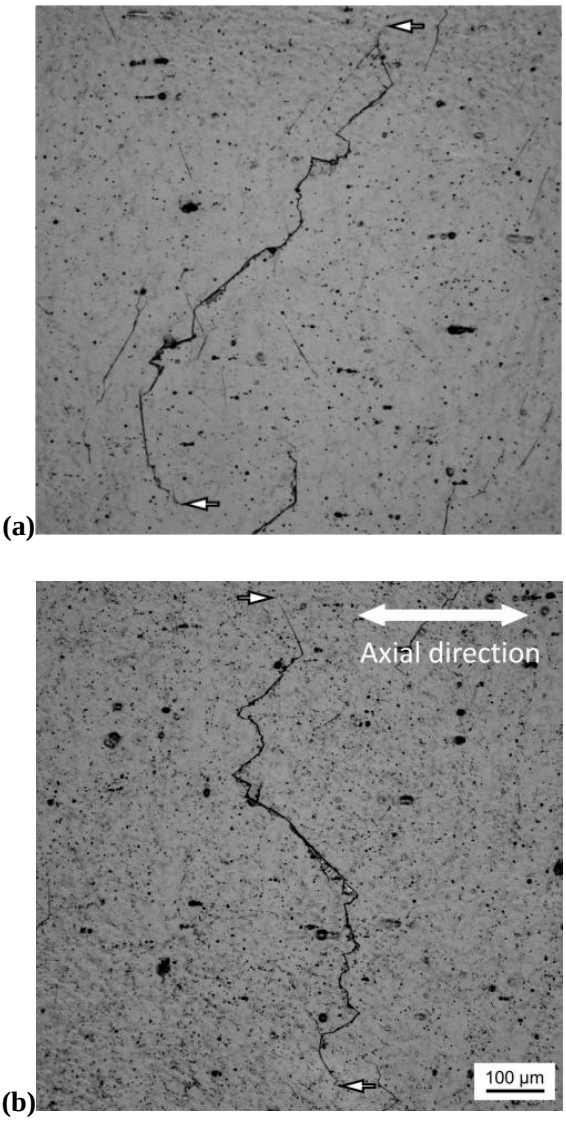

Fig. 5 Cracks in SUH660 specimens at σ_a = 400 MPa (arrows indicate crack tips):

(a) non-strained specimen ($N = 3 \times 10^5$ cycles); (b) pre-strained specimen ($N = 1.8 \times 10^5$ cycles).

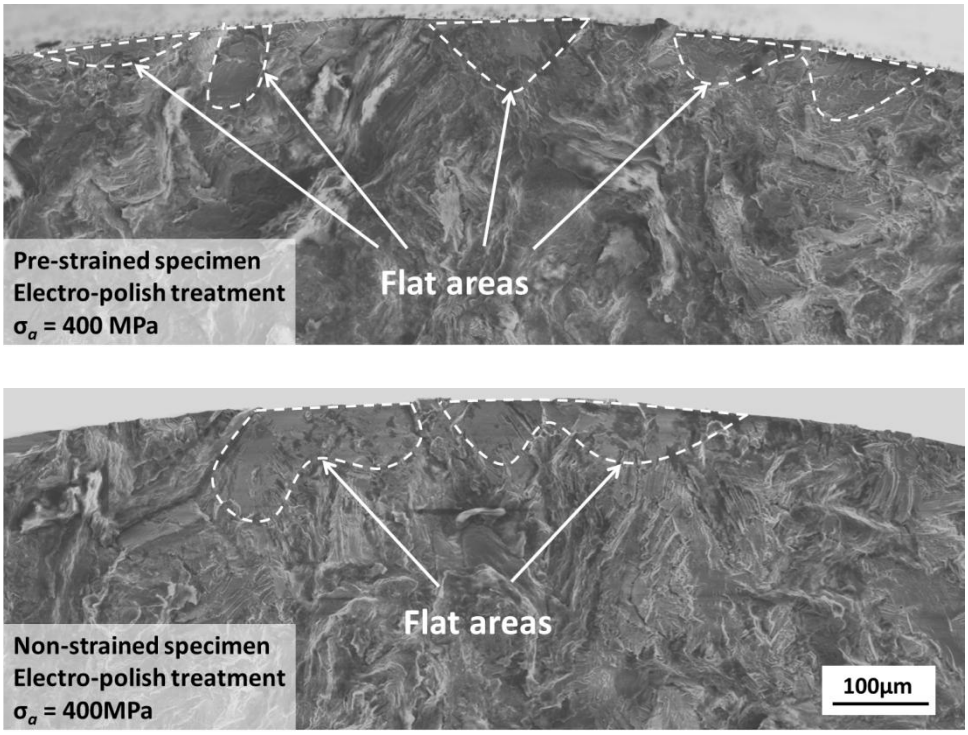

(a)

(b)

Fig. 6 Fracture surfaces of pre-strained and non-strained specimens at σ_a = 400 MPa:

(a) pre-strained specimen; (b) non-strained specimen.

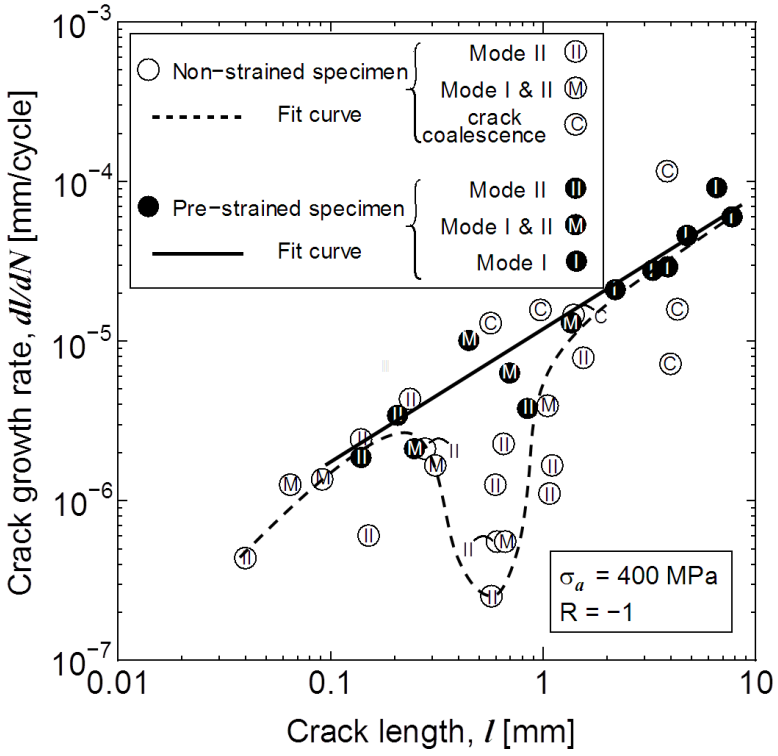

Fig. 7 Crack growth rate of pre-strained and non-strained specimens at σ_a = 400 MPa.

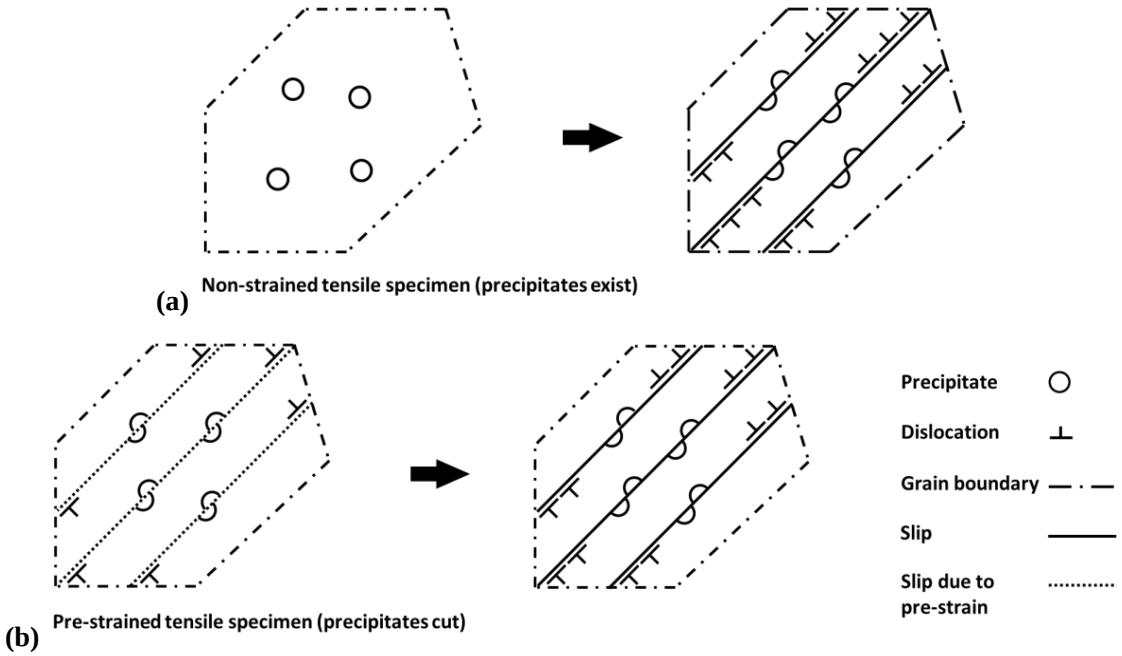

Fig. 8 Dislocation accumulation for tensile test of SUH660 steel: (a) non-strained specimen; (b) pre-strained specimen.

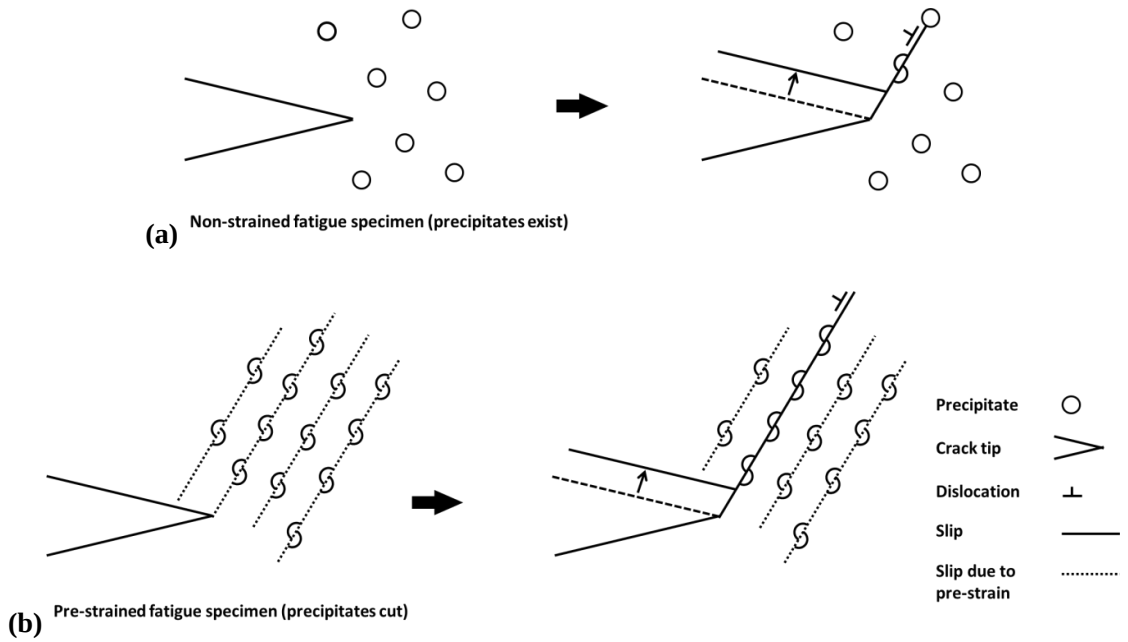

Fig. 9 Dislocation accumulation model at the crack tip for SUH660 steel: (a) non-strained specimen; (b) pre-strained specimen.

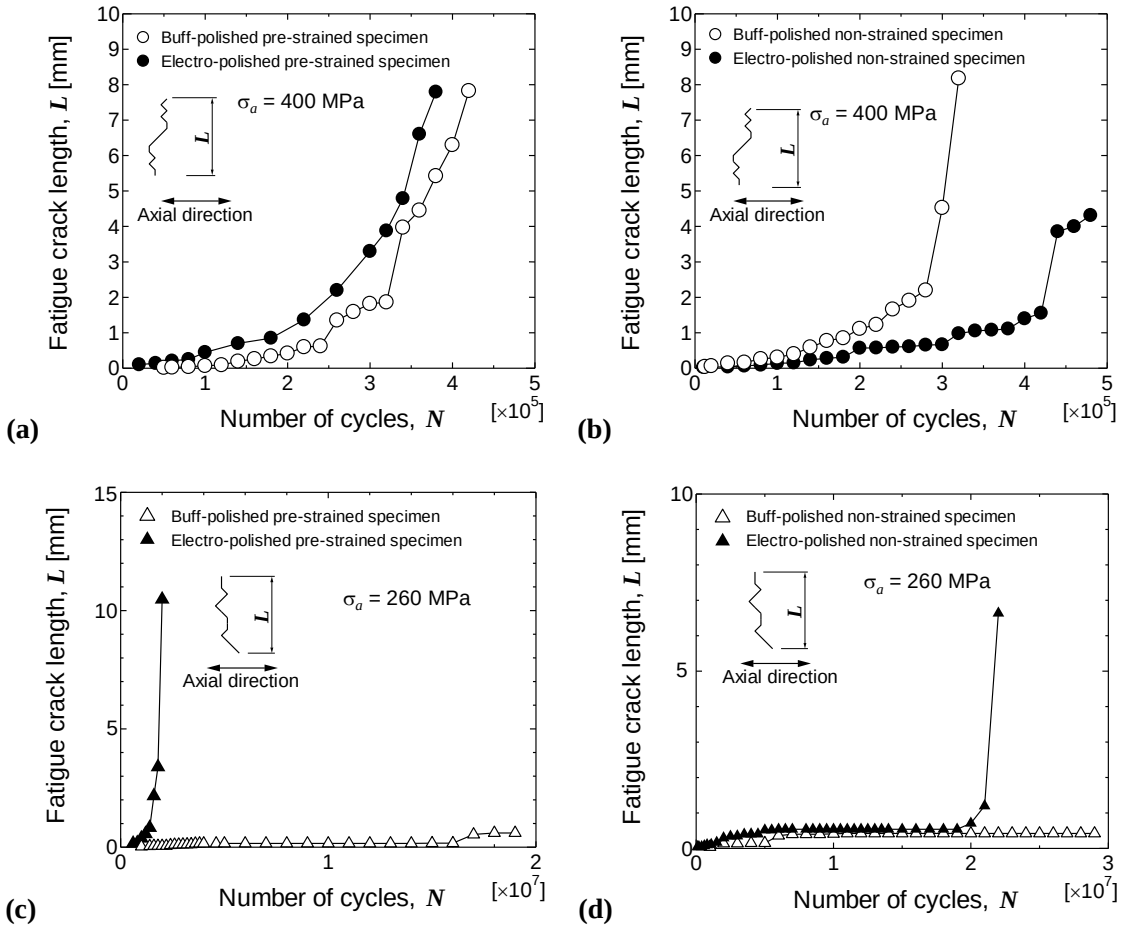

Fig. 10 Fatigue test results of buff-polished specimens compared to electro-polished specimen:

(a) buff-polished pre-strained specimen at σ_a = 400 MPa;

(b) buff-polished non-strained specimen at σ_a = 400 MPa;

(c) buff-polished pre-strained specimen at σ_a = 260 MPa;

(d) buff-polished non-strained specimen at σ_a = 260 MPa.

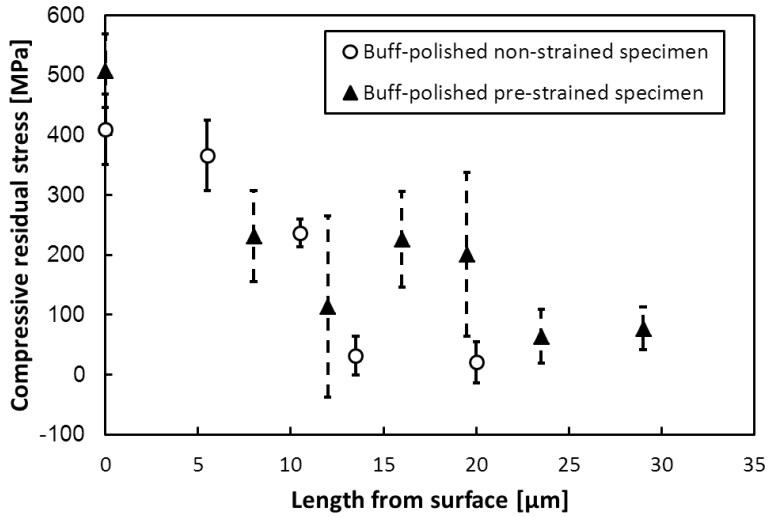

Fig 11 Residual stress distribution of buff-polished specimens.

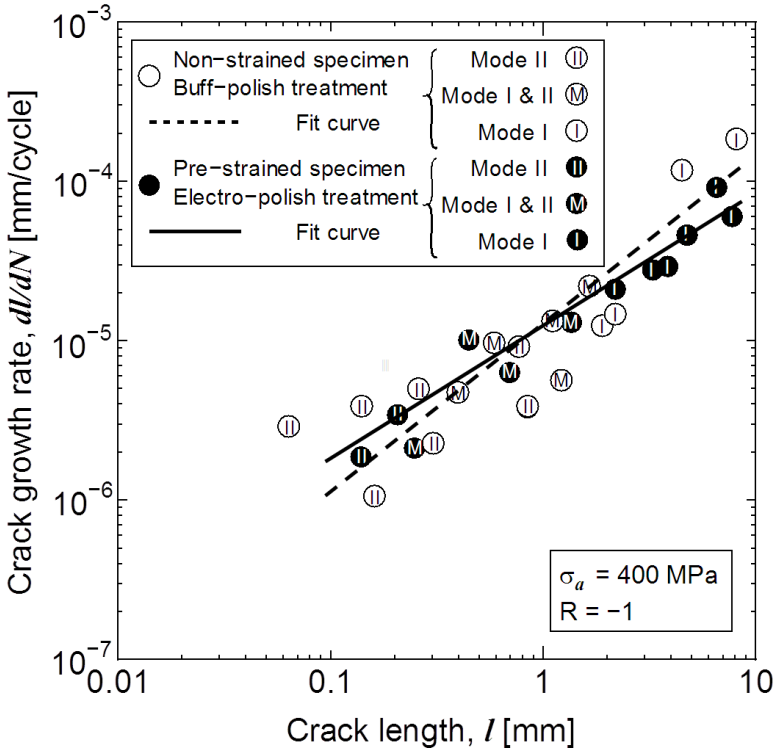

Fig. 12 Crack growth rate of electro-polished and buff-polished specimens at σ_a = 400 MPa.

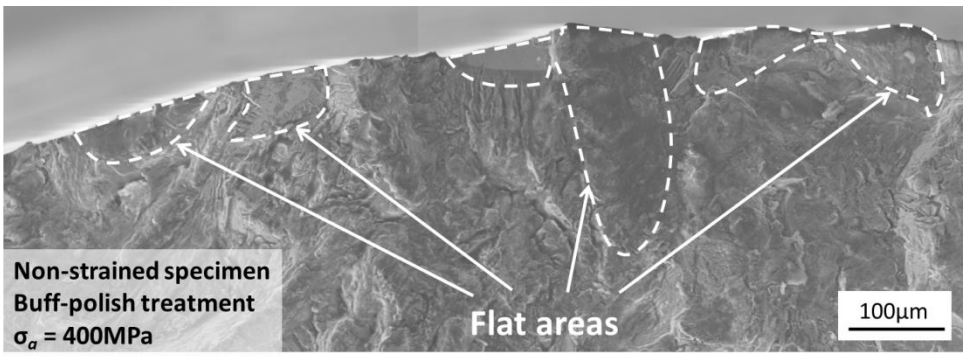

Fig. 13 Fracture surfaces of buff-polished non-strained specimens at σ_a = 400 MPa.

CHAPTER 3 EFFECT OF INTERNAL HYDROGEN ON VERY HIGH CYCLE FATIGUE

3.1 Introduction

Many research studies [1−4] have been conducted to clarify the effect of hydrogen on fatigue life by using fatigue specimens with artificial holes, pre-cracks, and flaws. As the fatigue life of common steel is usually dominated by crack growth [5, 6], the effect of hydrogen on the growth rate of fatigue crack from artificial holes or pre-cracks is an important consideration for understanding the influence of hydrogen on fatigue strength. However, the other aspect of fatigue life, namely, crack initiation life, has not been adequately investigated, with few research studies on hydrogen on fatigue crack initiation. Nakatani et al. [7] investigated the effect of irreversible hydrogen on fatigue crack behavior from an inclusion and estimated its fatigue crack initiation life.

Chapter 2.1 clarified the fatigue crack propagation behavior at the fatigue strength over 10^7 cycles, illustrating that the temporarily arrested crack re-propagated after a new crack was initiated near the crack tip. In SUH660 steel, crack initiation affects crack propagation life, thereby dominating fatigue life at the fatigue strength over 10^7 cycles, implying that the effect of hydrogen on crack initiation life cannot be neglected. As a crack in this material is initiated by slip generation and accumulation [8], the study of hydrogen influence on fatigue crack initiation from inclusion [7] is not applicable. Because of diffusion coefficient of hydrogen is extremely low, it is very difficult for hydrogen to invade SUH660 steel in a hydrogen environment [9]. Nevertheless, it can be invaded through hydrogen charging using a large amount of hydrogen, as under prolonged exposure to a high-pressure hydrogen gas environment, its tensile strength gets affected by the internal hydrogen [10]. Therefore, this chapter discusses the use of hydrogen-charged specimen to investigate the effect of hydrogen on crack initiation and fatigue life at the fatigue strength over 10^7 cycles for ensuring

the long-term reliability of SUH660 steel in a high-pressure hydrogen gas environment.

3.2 Experimental methods

Table 1 summarizes the chemical composition of SUH660 stainless steel discussed in this chapter. Prior to developing the specimen, the steel was solution treated (ST) for 1 h at 980 °C, air cooled, aged (A) for 16 h at 720 °C, and then air cooled again.

Figure 1 shows the shapes and dimensions of the fatigue test specimens, whose surfaces were buff-polished after machining and subsequently, electro-polished at 50 °C to remove damaged surface layers of 10−20 μm [11]. The surfaces of the hydrogen-charged specimens were electro-polished before charging at a temperature of 150 °C and hydrogen pressure of 10 MPa for 300 h. The hydrogen content was measured using thermal desorption spectrometry (TDS, EMD-WA1000S/H) for temperatures up to 800 °C at a heating rate of 0.33 °C/s. Figure 2 shows the cylindrical specimen and the sample for TDS measurement. For obtaining uncharged specimen measurements, a sample of 2 mm thickness was cut off from the cylindrical specimen. For obtaining hydrogen-charged specimen measurement, the cylindrical was first exposed at the same condition as the fatigue specimens, and thereafter, a sample was cut off from its center.

Fatigue tests were performed at room temperature in air using an Ono-type rotating-bending fatigue test machine. The uncharged and hydrogen-charged specimens were tested at frequencies of 55 Hz and 28 Hz, respectively. Shishime et al. [12] found that internal hydrogen indeed affected the fatigue strength of SUH660 steel at the latter frequency. The microscopic fatigue crack behaviors were observed using the replica method.

Vickers hardness (*HV*) tests were performed on the surface of the specimens. Indentations were made using a load of 0.49 N at the center of the grain to avoid grain boundary effects.

3.3 Experimental results

3.3.1 Distribution of hydrogen content

For the infinite cylinder of radius r_0, the following equations for hydrogen concentration ratio (C/C_0) and average hydrogen concentration ratio (C_{ave}/C_0) have been proposed [13, 14]:

$$\frac{C}{C_0} = 1 - 2\sum_{n=1}^{\infty} \frac{\exp(\frac{-D\beta_n^2 t}{r_0^2}) J_0(\frac{\beta_n r}{r_0})}{\beta_n J_1(\beta_n)} \quad (1)$$

$$\frac{C_{ave}}{C_0} = 1 - 4\sum_{n=1}^{\infty} \frac{\exp(\frac{-D\beta_n^2 t}{r_0^2})}{\beta_n^2} \quad (2)$$

where C_0 (ppm) is the surface hydrogen content; C (ppm) is the hydrogen content at distance r (m) from the center of cylinder; C_{ave} (ppm) is the average hydrogen content; D (m^2/s) is the hydrogen diffusion coefficient; t (s) is the time of hydrogen diffusion; J_0 and J_1 are Bessel functions of the first kind of zero and first orders, respectively; and β_n is a root of $J_0(\beta) = 0$.

The values of average hydrogen contents in uncharged and hydrogen-charged samples of 8-mm-diameter (obtained using TDS) were 0.06 ppm and 2.96 ppm, respectively. The hydrogen diffusion coefficient of SUH660 steel was obtained by Mine et al. [9] as 2×10^{-13} m^2/s at 150 °C. After hydrogen charging at the conditions discussed earlier, the C_0 of the 8-mm-diameter sample was calculated as 11.91 ppm in a hydrogen pressure of 10 MPa from equation (2). As hydrogen content first reached equilibrium at the specimen's surface, the C_0 is regarded as the equilibrium hydrogen content. According to equation (1), the hydrogen content distribution in the 5-mm-diameter test section of the fatigue specimen was calculated as shown in Fig. 3. This distribution is observed to extend from the surface to the interior of the specimens. After hydrogen charging, the hydrogen content in the specimen reaches its saturated value at its surface and is close to that of the uncharged specimen at its interior. Chapter 2.1 clarified that fatigue crack in SUH660 steel is initiated by slip generation and accumulation in the grain. The average length of the crack initiation site is

approximately 70 μm [15]. The layer from the specimen surface to the depth of 70 μm may be regarded as the "crack initiation layer" and hence, the hydrogen existing within is considered to affect crack initiation. When a hydrogen-charged fatigue specimen is tested in air at room temperature, the hydrogen content at its surface reduces because it is discharged into air. The calculation of hydrogen content distribution after 10^7 cycles (100 h) in air at room temperature (Fig. 3(b)) revealed that although the hydrogen content decreases significantly from the specimen surface to the depth of 20 μm, adequate hydrogen exists within the crack initiation layer to have an effect on it after 10^7 cycles.

3.3.2 *S-N* and fatigue crack behavior

Figure 4 shows the *S-N* diagram of uncharged and hydrogen-charged specimens. Chapter 2.1 stated that an *S-N* curve with two 'fatigue limits' can be used for uncharged specimens. In the vicinity of fatigue strength at 10^7 cycles of the uncharged specimen, the hydrogen-charged specimen's fatigue life exceeds 10^7 cycles at 280 MPa and remains unbroken even over 4×10^7 cycles at 260 MPa. Figure 5 shows the crack growth behavior of the primary crack that leads to fatigue failure at 400 and 280 MPa. Similar trends for crack growth rate can be observed in the uncharged and hydrogen-charged specimens at 400 and 280 MPa; the crack growth rates accelerated first and decelerated after the crack length reached a certain value and re-accelerated until fatigue failure. Therefore, the crack growth mechanism is not considered to be altered by internal hydrogen above the fatigue strength at 10^7 cycles of the uncharged specimen.

Figure 6 shows the crack growth behavior of the longest crack at 260 MPa. As the specimen was unbroken, the fatigue behavior of the longest crack on its surface is discussed instead of its primary crack. In both types of specimens, after 10^7 cycles, the growth rate of the longest crack at 260 MPa decelerated to zero, and did not re-accelerate immediately, but after several million cycles, it increased instantaneously to a higher value and then decreased to zero. The longest fatigue crack in both specimens propagated intermittently (as seen in Figs. 7 and 8). In the uncharged specimen, the longest crack was arrested for three million cycles (from 2.8×10^7 cycles to 3.1×10^7 cycles); however, in the next one million cycles, both arrested crack tips re-propagated. The upper crack tip followed the same direction as the arrested crack tip, and its re-propagation site was not from but close to the arrested crack tip. The re-propagated lower crack tip followed the same direction as that of the arrested crack tip. The longest crack in the hydrogen-charged specimen was arrested for 20 million cycles (from 1.15×10^7 cycles to 3.15×10^7 cycles) and the lower crack tip re-propagated in the next one million cycles. Similar to the uncharged specimen, the re-propagated crack site was

close to the arrested crack tip. Hence, its crack re-propagation mechanism is also considered to be due to new crack initiation near the temporarily arrested crack tip (as clarified in Chapter 2.1), implying that the crack growth mechanism is not altered by internal hydrogen below the fatigue strength at 10^7 cycles of the uncharged specimen.

In summary, the fatigue strength at 10^7 cycles of hydrogen-charged specimen is the same as that of the uncharged specimen because the crack growth behavior is not altered by internal hydrogen above and below the fatigue strength at 10^7 cycles.

3.3.3 Fractography of fracture surface

Figure 9 shows the fracture surfaces at 400 MPa. In the uncharged and hydrogen-charged SUH660 steel specimens, flat areas existed near and inside their surface, caused by crack initiation and Mode II crack growth, respectively, as stated in Chapter 2.1. Therefore, the hydrogen-charged specimen's crack initiation site also existed within the crack initiation layer near the surface, inside which it facilitated the easy growth of the crack by Mode II. This implies that the crack growth behavior inside the specimen is not altered after hydrogen charging.

3.4 Discussion

3.4.1 Effect of internal hydrogen on the crack initiation behavior

3.4.1.1 Effect of internal hydrogen above the fatigue strength at 10^7 cycles

The primary crack initiation lives of the uncharged and hydrogen-charged specimens are almost the same and account for a small proportion of the fatigue life at 400 MPa, as seen from Figs. 5 and 6. At 280 MPa, the primary crack initiation life of the hydrogen-charged specimen is much longer and accounts for a greater proportion of the fatigue life than does the uncharged specimen. However, at 260 MPa, the crack initiation life of the longest crack of the hydrogen-charged specimen appears shorter than that of the uncharged specimen. In the fatigue test of SUH660 steel, many cracks were initiated on the specimen surface; the primary or the longest crack was one of them but it was not necessarily the first initiated crack. Therefore, the crack initiation lives of the primary or the longest cracks in both type specimens have a large scatter and cannot be used for discussing hydrogen influence. In this chapter, all cracks on the specimen surface are used for investigating the effect of hydrogen on crack initiation.

Figures 10 and 11 illustrate the crack initiation behaviors of uncharged and hydrogen-charged specimens. At first, a thin line appeared in the grain and thereafter, its length increased and formed a crack. As the thin line did not have adequate stress intensity factor, its length could not be increased by propagation, although slip was generated and accumulated. Thus, it cannot be regarded as a crack until it begins to propagate. In this chapter, the number of cracks on the specimen surface at each cycle is obtained to clarify the regularity of crack initiation. Figure 12 shows the number of cracks vs. the number of cycles (*N*-*N* diagram) at 400 and 280 MPa. The number of cracks on the specimen surface increases with the number of cycles, and fewer cracks were initiated on hydrogen-charged specimen compared to those in the uncharged specimen at the same number of cycles. Therefore, hydrogen inhibits (or increases the difficulty in) the number of cracks initiated above the fatigue

strength at 10^7 cycles. In the diagram showing the increments in crack initiation, if the numbers of cracks in two adjacent cycles are subtracted, those in each segment of the crack initiation life can be obtained. Figure 13 shows the distribution of crack initiation life at 400 and 280 MPa. According to mechanism of SUH660 steel, the crack initiation life depends on the rate of slip generation and accumulation. As the crystal orientation and maximum shear stress direction affect these two phenomena in a grain, the crack initiation life is said to be related to crystal orientation during fatigue tests. In Chapter 2.2, the relationship of *HV* and crystal orientation was clarified, indicating that the distribution of the crystal orientation of grains follows the normal distribution, as in the case of *HV* values. Therefore, the pattern of change in the number of cracks in each segment of the crack initiation life is considered to be fitted to the distribution curve, it is called crack initiation life distribution in this chapter. In the said distribution pattern at 400 and 280 MPa, the crack initiation life pertaining to the maximum number of cracks is represented by the peak site and those near it pertain to a majority of the cracks. Therefore, the crack initiation life at the peak site can be regarded as the approximate average crack initiation life (AACIL). At 400 MPa, the AACIL of the hydrogen-charged specimen was almost the same as that of the uncharged specimen. However, when the stress decreased to 280 MPa, the AACIL of the former increased to 4×10^6 cycles, which was 2×10^6 cycles longer than that of the latter. Hydrogen accelerates the increase in crack initiation lives, and its influence is not obvious at 400 MPa but becomes increasingly significant with stress decreasing. Therefore, compared to the uncharged specimen, the primary crack in the hydrogen-charged specimen is considered to present greater probability for longer crack initiation life owing to its higher AACIL. Therefore, the hydrogen-charged specimen has a much longer primary crack initiation life than the uncharged specimen at 280 MPa.

3.4.1.2 Effect of internal hydrogen below the fatigue strength at 10^7 cycles

Figure 14 shows the *N*-*N* diagram and crack initiation life distribution at 260 MPa. Compared to those on the uncharged specimen, fewer cracks are initiated on the hydrogen-charged specimen at 260 MPa, implying that hydrogen inhibits the number of cracks initiated by increasing the difficulty of initiation below the fatigue strength at 10^7 cycles. Owing to this temporary crack arrest behavior [8], fatigue life exceeds 10^7 cycles, after which crack initiation occurs. At 260 MPa, the distribution of crack initiation life has two peak sites: one before and another after 10^7 cycles. The minimum point existing between the two peak sites may be used to demarcate the distribution of crack initiation life and bifurcate it. Chapter 2.2 mentioned that SUH660 steel is also characteristic of hardness variation besides *HV* variation, and cracks are easily initiated in low hardness zones. Therefore, the multiple parts in the distribution of crack initiation life are considered to be related to the different hardness zones, with the first part regarded to be related to the low hardness zone. In Fig. 14(b), the crack initiation life distributions in low hardness zone exists before 10^7 cycles in both type specimens, and they have almost the same AACIL of 4×10^6 cycles. The AACIL of hydrogen-charged specimen is also 4×10^6 cycles at 280 MPa according to Fig 13(b). Therefore, the distributions of crack initiation life above the fatigue strength at 10^7 cycles may be considered as the crack initiation life distribution in low hardness zone. The AACILs in low hardness zone stop changing at a crack initiation life of 4×10^6 cycles in both types of specimens, and this value is regarded to be the maximum value of AACIL for SUH660 steel in low hardness zone. Hence, hydrogen is considered to have no effect on the maximum value of AACIL but only accelerates the increase in crack initiation lives with decreasing stress in low hardness zone.

After most of cracks are initiated in low hardness zone with the increase in the number of cycles, cracks begin to be initiated in zones with higher hardness. In this chapter, such zones are referred to as medium hardness zone to easily distinguish them from low hardness zone. The second

part of the crack initiation life distribution may be regarded as that in medium hardness zone. Figure 14(b) shows that the AACIL of the uncharged specimen in medium hardness zone is 2×10^7 cycles whereas for the hydrogen-charged specimen, the peak site has not yet appeared after the crack initiation life of 4×10^7 cycles. Therefore, the AACIL of hydrogen-charged specimen in medium hardness zone is considered to be longer than that of the uncharged specimen at 260 MPa, implying that below the fatigue strength at 10^7 cycles, hydrogen accelerates the increase in crack initiation lives in medium hardness zone with decreasing stress.

The effect of internal hydrogen on crack initiation in SUH660 steel can be summarized as follows. Hydrogen inhibits the number of cracks initiated on the specimen surface. Above the fatigue strength at 10^7 cycles, cracks are typically initiated in low hardness zone. Hydrogen is considered to have no effect on the maximum value of AACIL but only accelerates the increase in crack initiation lives with decreasing stress in low hardness zone. Below the fatigue strength at 10^7 cycles, cracks are initiated in medium hardness zone beside in low hardness zone. Hydrogen accelerates the increase in crack initiation lives with decreasing stress in medium hardness zone.

3.4.2 Effect of hydrogen on the hardness

Section 3.4.1, which discusses the effect of hydrogen on crack initiation, reveals that hydrogen inhibits crack initiation and accelerates the increase in the crack initiation life. In a study conducted by Jia et al. [16], the relationship between crack initiation and hardness was clarified, revealing that higher hardness hinders crack initiation. Hence, the effect of hydrogen on crack initiation is surmised to be related to the change in hardness after hydrogen charging. However, because of the variation in hardness, the common method of averaging the *HV* data is not applicable to investigating hydrogen influence. Therefore, a method of obtaining the hardness distribution using the *HV* distributions in multiple test zones (proposed in Chapter 2.2) is used for clarifying the difference in the hardness of uncharged and hydrogen-charged specimens. Figure 15 shows the *HV* distributions of both specimens. According to Chapter 2.2, a region of 600 × 450 μm on the specimen surface was defined as a zone, and the *HV* data of 10 grains per zone were obtained and plotted in the normal probability paper. In this chapter, the *HV* data for six zones are discussed for each type of specimen. As a zone comprised an average of 65 grains, the cumulative probability of 1/65 (~1.5%) represented the softest grain in the zone, and its *HV* value could be regarded as its hardness value of the zone. Thereafter, the hardness values for six zones for both specimens were plotted in the normal probability paper to investigate the influence of hydrogen. According to the hardness distribution (shown in Fig. 16), in high hardness zones, the hardness of both specimens remained almost the same. However, in medium and low hardness zones, the hardness of the hydrogen-charged specimen was 14 *HV* higher than that of the uncharged specimen. In the *HV* test, when the indenter comes into contact with the specimen surface, a large number of dislocations are generated with plastic deformation occurring around the indentation. Moriya et al. [17] reported that hydrogen gets trapped at a dislocation core and pins to an edge dislocation. Therefore, in medium and low hardness zones, based on the increase in hardness, hydrogen is considered to diffuse into new dislocations and hinder

slip, and then inhibit the initiation of cracks and accelerate the increase in crack initiation life.

3.4.3 Effect of internal hydrogen on the fatigue life below the fatigue strength at 10^7 cycles

Chapter 2.1 clarified the crack re-propagation behavior of SUH660 steel below the fatigue strength at 10^7 cycles, demonstrating that precipitate cutting occurred in the plastic region near the temporarily arrested crack tip, weakening its hardness and promoting new crack initiation. Hence, below the fatigue strength at 10^7 cycles, fatigue life is dependent on the initiation lives of new cracks near the temporarily arrested crack tip. According to Fig. 6, re-propagation behavior of the temporarily arrested crack in SUH660 steel occurs mainly after 10^7 cycles. Therefore, according to Section 3.4.1.2, new crack initiation in the weakened plastic region near the temporarily arrested crack tip can be regarded as crack initiation in medium hardness zone, and the scatter of the initiation lives is considered following its distribution in medium hardness zone. As the hydrogen accelerates the increase in crack initiation life in medium hardness zone, the fatigue life of the hydrogen-charged specimen is considered to be much longer than that of the uncharged specimen below the fatigue strength at 10^7 cycles.

Figure 17 shows the *S*-*N* curve of the hydrogen-charged specimen. At 280 MPa, owing to higher AACIL in low hardness zone, a higher probability of a longer crack initiation life extends its fatigue life to close to or greater than 10^7 cycles. At 260 MPa, this specimen's fatigue life is extended owing to its longer life of new crack initiation near the temporarily arrested crack tip. Therefore, in the vicinity of fatigue strength at 10^7 cycles, compared to the uncharged specimen, the hydrogen-charged specimen has a longer fatigue life and its pattern of change is considered to be smoother. At 400 MPa, the AACIL of the hydrogen-charged specimen seems no longer than that of the uncharged specimen, implying that the difference in the crack initiation life is not the main reason for the difference in the fatigue lives of both types of specimens. According to Shishime et al [12], in the region of fatigue life at 10^6 cycles, the hydrogen-charged specimen of SUH660 steel has a shorter crack propagation life owing to its lower crack growth rate. However, according to Fig. 5,

the hydrogen-charged specimen has a longer crack propagation life than that of the uncharged specimen. As hydrogen content has a significant influence on the crack growth rate [18, 19], it is difficult to discuss its effect on crack propagation using the existing data obtained from fatigue tests in the superficial hydrogen-charged specimen. Therefore, in this chapter, a dotted curve is temporarily used to depict the pattern of change in the fatigue life of the hydrogen-charged specimen above 280 MPa.

3.5 Conclusions

The study discussed in this chapter was conducted using all cracks instead of only the primary crack that leads to fatigue failure for the purpose of investigating the effect of internal hydrogen on crack initiation in SUH660 steel, to further predict its pattern of change in fatigue life below the fatigue strength at 10^7 cycles after hydrogen charging. The following conclusions were drawn from the study:

(1) Hydrogen inhibits the number of cracks initiated, but does not change the fatigue strength at 10^7 cycles. Above the fatigue strength at 10^7 cycles, hydrogen accelerates the increase in crack initiation lives with decreasing stress in low hardness zone. Below the fatigue strength at 10^7 cycles, hydrogen accelerates the increase in the crack initiation lives with decreasing stress in medium hardness zone.

(2) The hardness of the hydrogen-charged specimen is 14 *HV* higher than that of the uncharged specimen in medium and low hardness zones, and is considered to be related to the slip hindrance due to hydrogen diffusing into new dislocations and inhibiting crack initiation, and the acceleration of the increase in crack initiation life.

(3) The scatter of new crack initiation lives is considered to follow the distribution of the crack initiation life in medium hardness zone. New crack initiation life is accelerated by hydrogen. Therefore, the fatigue life of the hydrogen-charged specimen is much longer than that of the uncharged specimen below the fatigue strength at 10^7 cycles.

References

[1] Kanezaki T, Narazaki C, Mine Y, Matsuoka S, Murakami Y. Effects of hydrogen on fatigue crack growth behavior of austenitic stainless steels. *International Journal of Hydrogen Energy*, **33**; 2008, p. 2604–19

[2] Macadre A, Yano H, Matsuoka S, Furtado J. The effect of hydrogen on the fatigue life of Ni–Cr–Mo steel envisaged for use as a storage cylinder for a 70 MPa hydrogen station. *International Journal of Fatigue*, **33**; 2011, p. 1608–19

[3] Takakuwa O, Soyama H. Suppression of hydrogen-assisted fatigue crack growth in austenitic stainless steel by cavitation peening. *International Journal of Hydrogen Energy*, **37**; 2012, p. 5268–76

[4] Gaddam R, Pederson R, Hornqvist M, Antti ML. Fatigue crack growth behaviour of forged Ti–6Al–4V in gaseous hydrogen. *Corrosion Science*, **78**; 2014, p. 378–83

[5] Wong YK. A phenomenological and mechanistic study of fatigue under complex loading histories. Thesis (Ph.D.)--University of Western Australia, 2003

[6] Lei Z, Xie J, Sun C, Liu X, Hong Y. Effects of microstructure on very-high-cycle fatigue crack initiation and life scatter for a high strength steel. 13th International Conference on Fracture, 2013

[7] Nakatani M, Sakihara M, Minoshima K. Decrease in fatigue crack initiation life by irreversible hydrogen in cold drawn eutectoid steel. 12th International Conference on Fracture, 2009

[8] Wu H, Hamada S, Noguchi H. Fatigue strength characteristics evaluation of SUH660 considering small fatigue crack propagation behavior and hardness distribution. *International Journal of Fatigue*, under review

[9] Mine Y, Kimoto T. Hydrogen uptake in austenitic stainless steels by exposure to gaseous hydrogen and its effect on tensile deformation. *Corrosion Science*, **53**; 2011, p. 2619–29

[10] Hicks PD, Altstetter CJ. Internal hydrogen effect on tensile properties of iron- and nickel-base superalloys. *Metallurgical and Materials Transactions*, **21**; 1990, p. 365−72

[11] Wu H, Hamada S, Noguchi H. Pre-strain effect on fatigue strength characteristics of SUH660 plain specimens. *International Journal of Fatigue*, **55**; 2013, p. 291–8

[12] Shishime K, Kubota M, Kondo Y. Effect of absorbed hydrogen on the near threshold fatigue crack growth behavior of short crack. *Materials Science Forum*, **567 – 568**; 2013, p. 409–12

[13] Demaret A, Hock AG, Meunier FA. Diffusion of hydrogen in mild steel. *Acta Metallurgia*, **2**; 1954, p. 214–23

[14] Suzuki Y, Itoga H, Noguchi H. Effect of hydrogen exposure on the notch tensile properties of high strength steel in hydrogen gas environment. *Journal of Solid Mechanics and Materials Engineering*, **6**; 2012, p. 265-77 (in Japanese)

[15] Wu H, Hamada S, Noguchi H. Fatigue strength prediction for inhomogeneous face-centered cubic metal based on Vickers hardness. *International Journal of Fatigue*, **48**; 2013, p. 48–54

[16] Jia GW, Hua L, Mao HJ. The influence of surface layer microstructure evolution of M2 steel cold-ring rolling mandrel roller on fatigue crack initiation. *Journal of Materials Processing Technology*, **187–188**; 2007, p. 562–65

[17] Moriya S, Matsui H, Kimura H. The effect of hydrogen on the mechanical properties of high purity iron II. Effect of quenched-in hydrogen below room temperature. *Materials Science and Engineering*, **40**; 1979, p. 217–25

[18] Murakami Y, Matsuoka S. Effect of hydrogen on fatigue crack growth of metals. *Engineering Fracture Mechanics*, **77**; 2010, p. 1926–40

[19] Mine Y, Orita A, Murakami K, Olive JM. Fatigue crack growth behaviour in austenitic stainless steels subjected to superficial and entire hydrogenation. *Materials Science and Engineering A*, **548**; 2012, p. 118–25

List of tables and figures

Table 1 Chemical composition of SUH660 steel (wt. %).

C	Si	P	S	Ni	Cr	Mo	Ti	V	Al	Fe	N	B
0.041	0.11	0.003	0.0017	25.4	15.19	1.43	2.23	0.30	0.21	Bal.	0.0012	0.0033

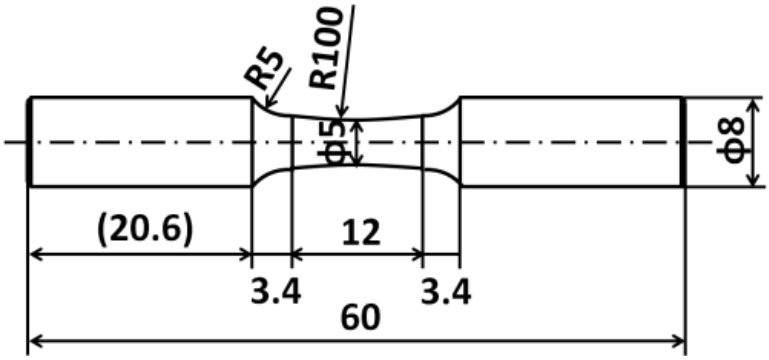

Fig. 1 Shapes and dimensions of fatigue test specimens (unit: mm).

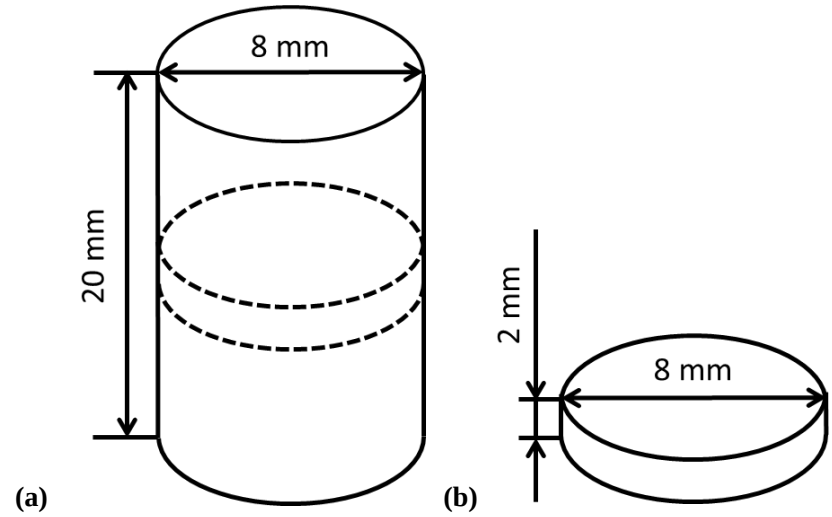

Fig 2 Cylindrical specimen and the sample for TDS measurement: (a) cylindrical specimen;

(b) TDS measurement sample.

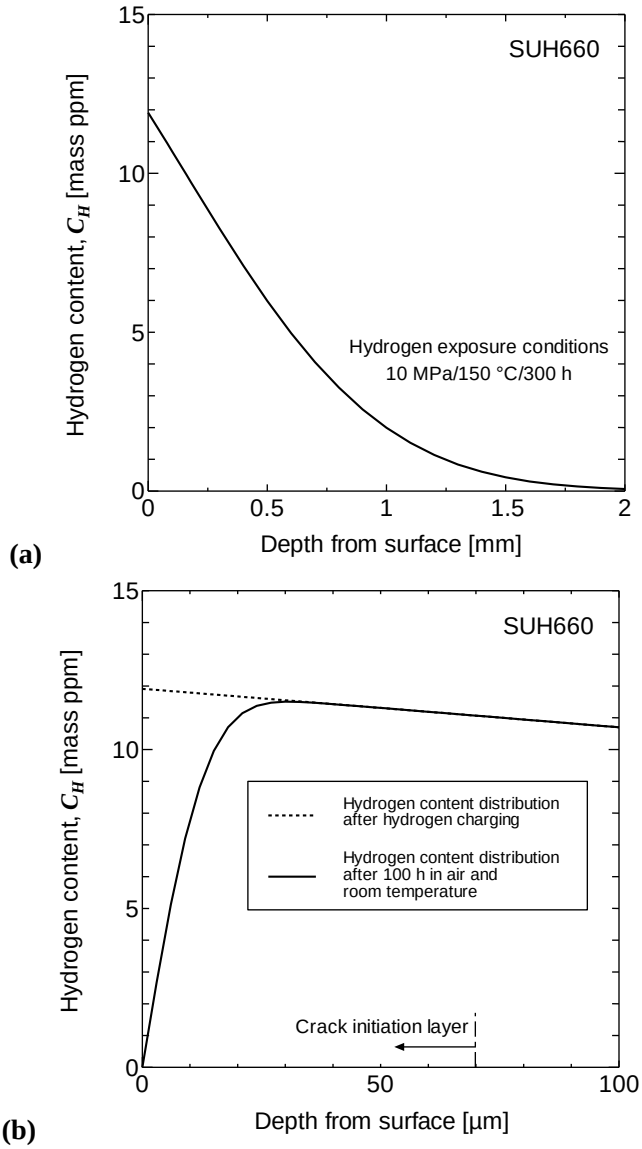

Fig. 3 Hydrogen content distribution in the test section of the fatigue specimen:

(a) after hydrogen charging; (b) after 100 h in air and room temperature.

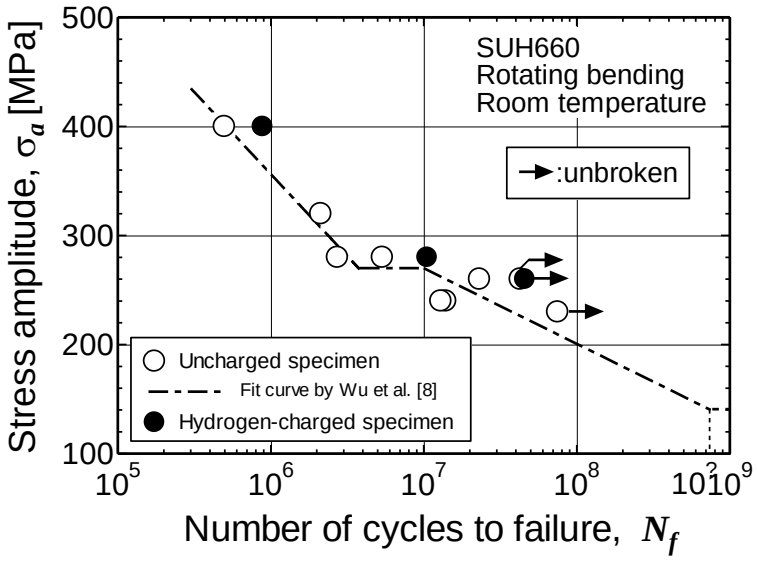

Fig. 4 *S-N* diagram of SUH660 steel.

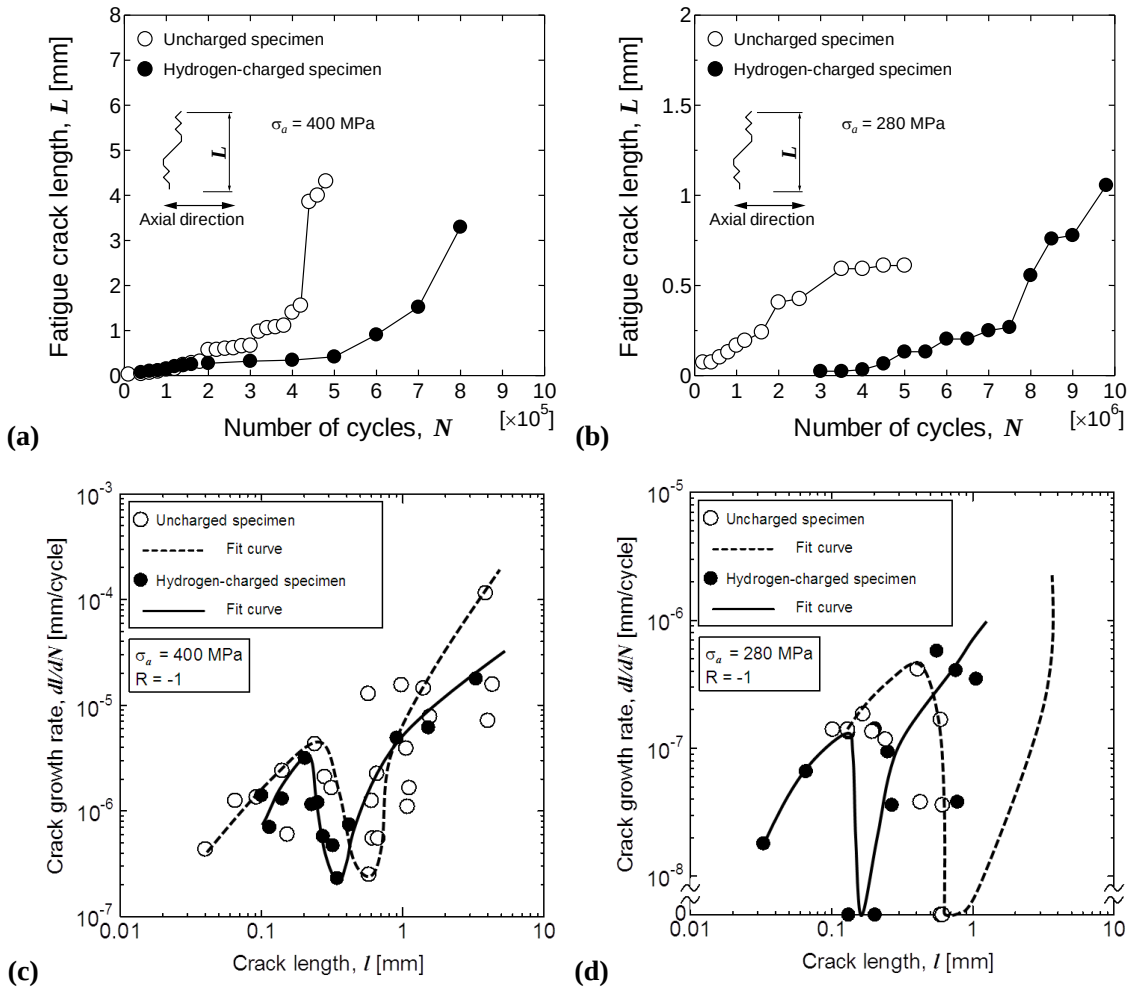

Fig. 5 Fatigue crack growth behavior at 400 and 280 MPa: (a) crack growth curve at 400 MPa; (b) crack growth curve at 280 MPa; (c) crack growth rate at 400 MPa; (d) crack growth rate at 280 MPa.

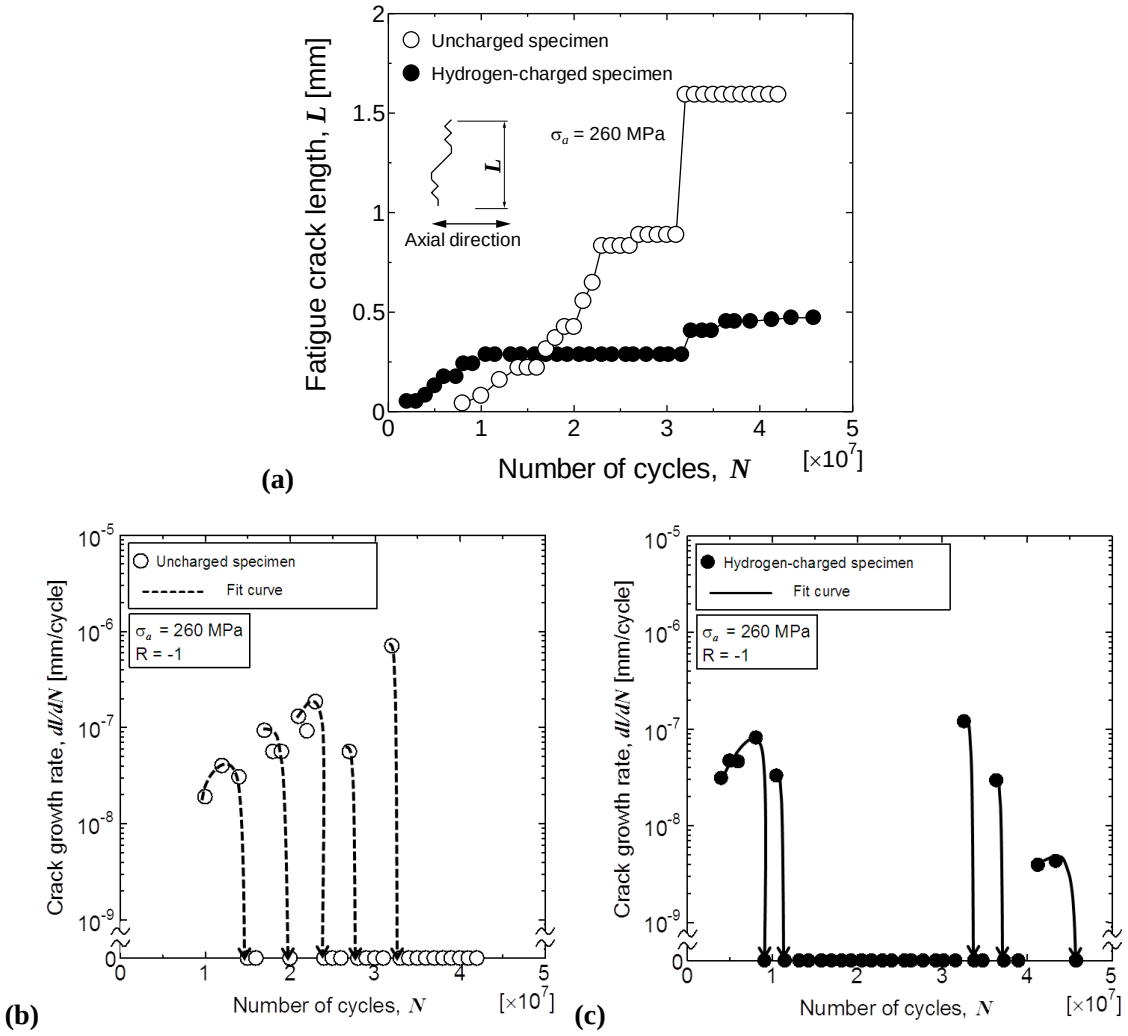

Fig. 6 Fatigue crack growth behavior at 260 MPa: (a) crack growth curve;

(b) crack growth curve of uncharged specimen;

(c) crack growth curve of hydrogen-charged specimen.

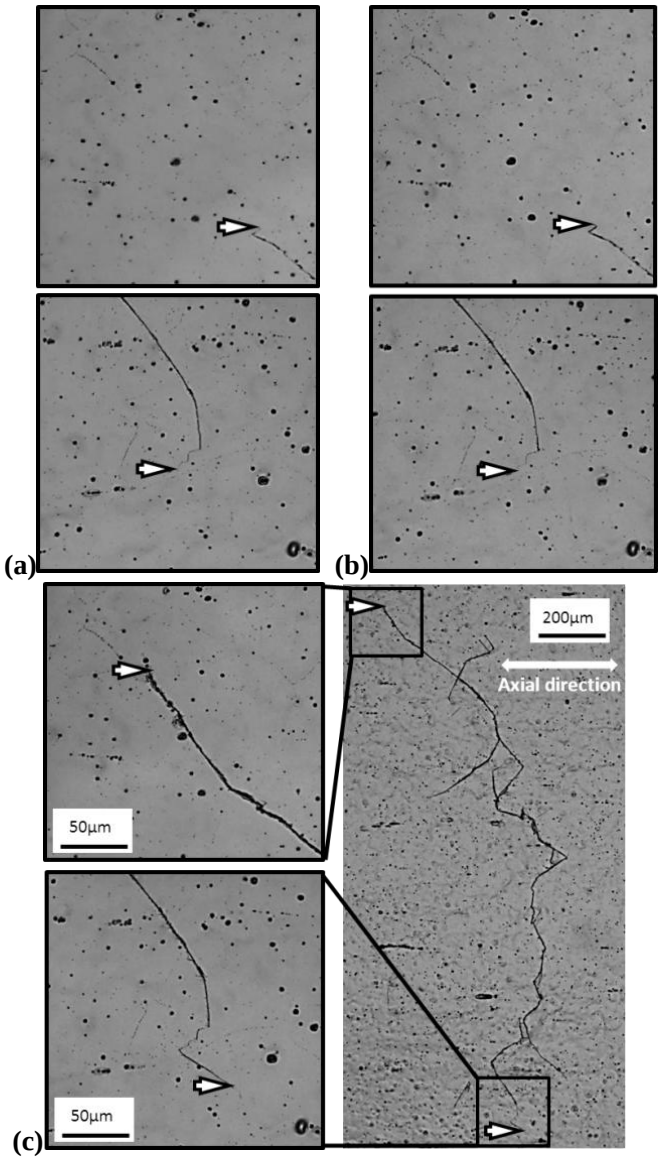

Fig. 7 Crack growth behavior of uncharged specimen (the arrows indicate the crack tips) (σ_a = 260 MPa): (a) $N = 2.8 \times 10^7$ cycles; (b) $N = 3.1 \times 10^7$ cycles; (c) $N = 3.2 \times 10^7$ cycles.

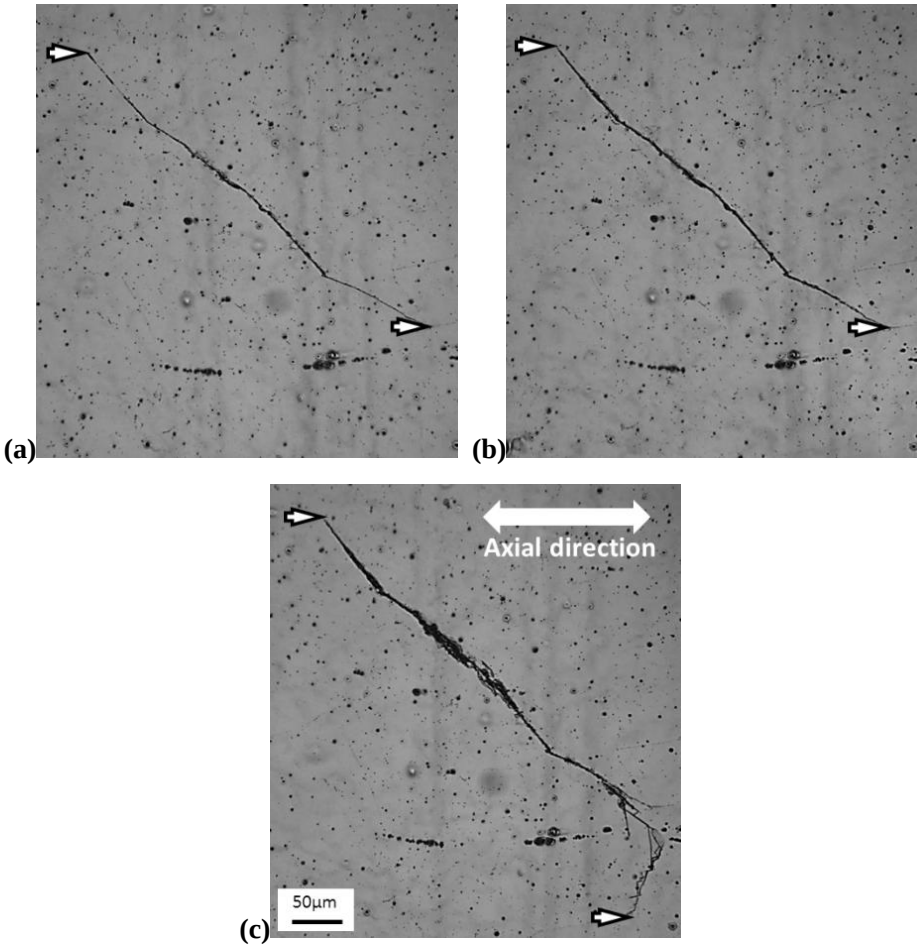

Fig. 8 Crack growth behavior of hydrogen-charged specimen (the arrows indicate the crack tips) (σ_a = 260 MPa): (a) $N = 1.15 \times 10^7$ cycles; (b) $N = 3.15 \times 10^7$ cycles; (c) $N = 3.25 \times 10^7$ cycles.

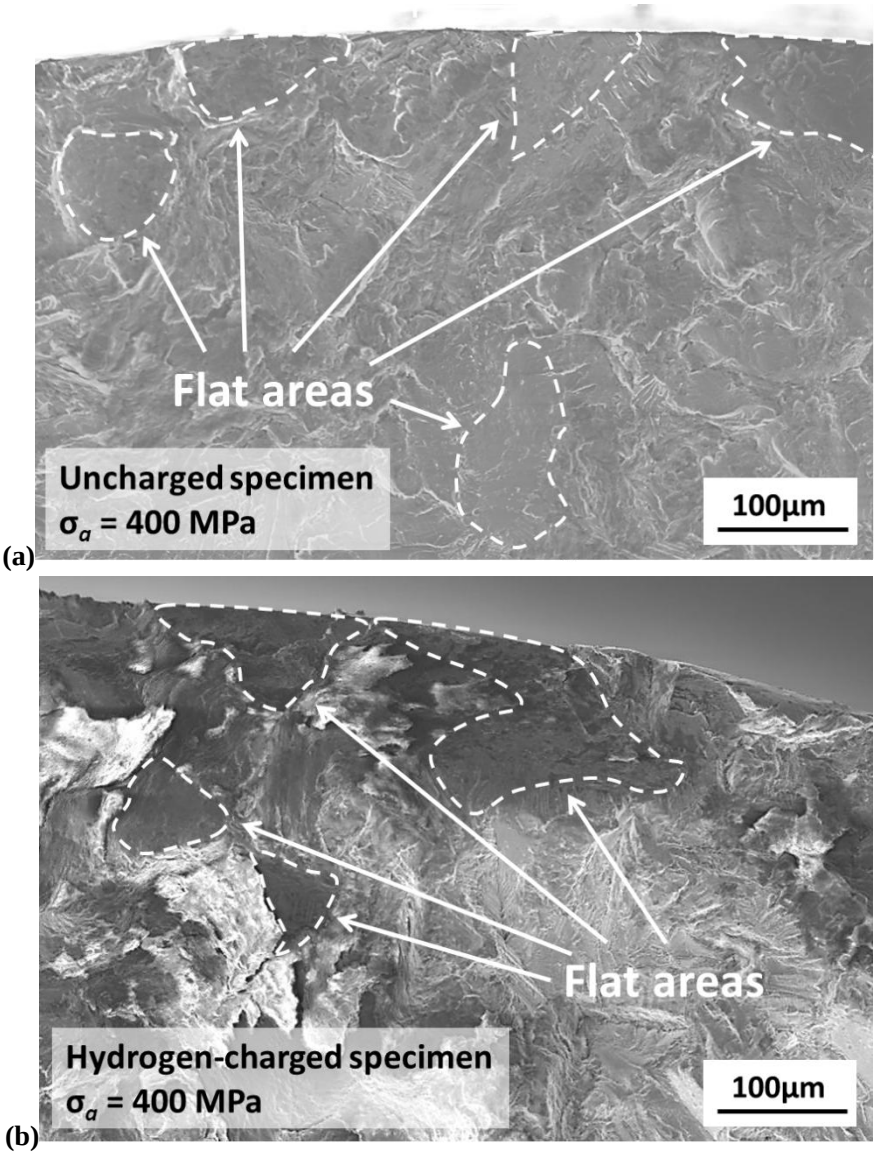

Fig. 9 Fracture surfaces at 400 MPa: (a) uncharged specimen; (b) hydrogen-charged specimen.

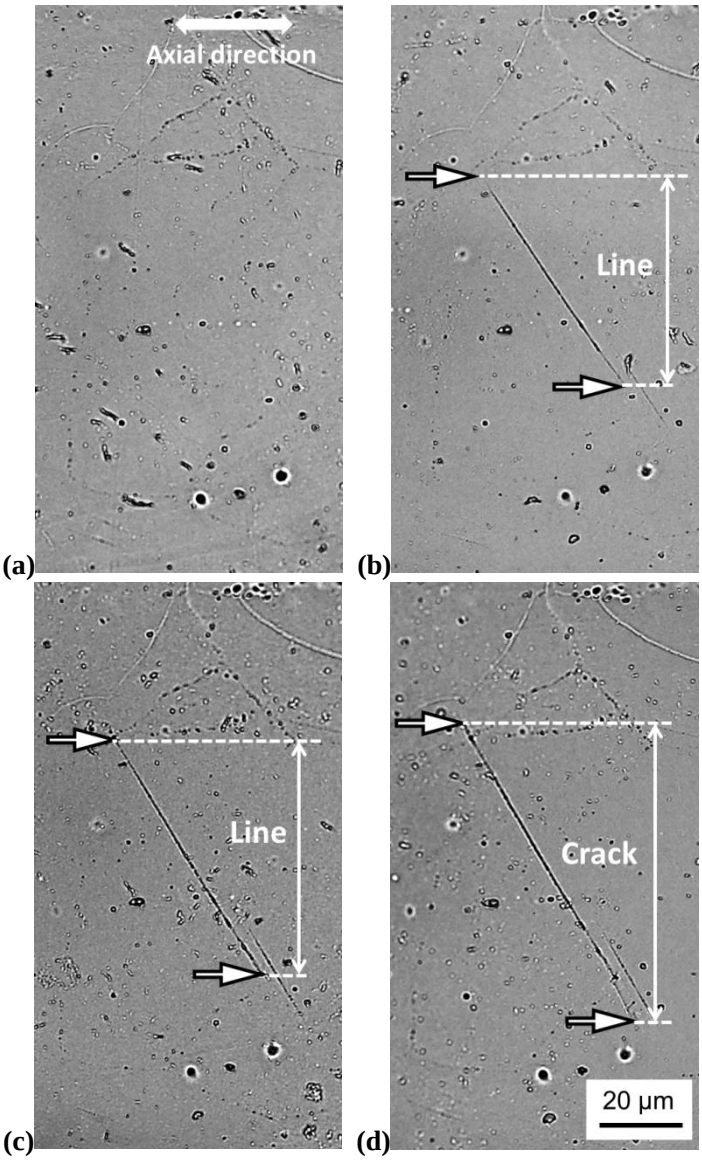

Fig. 10 Crack initiation behavior of uncharged specimen (the arrows indicate the crack tips) (σ_a = 230 MPa): (a) N = 0; (b) N = 4.0 × 10^5 cycles; (c) N = 1.0 × 10^6 cycles; (d) N = 1.2 × 10^6 cycles.

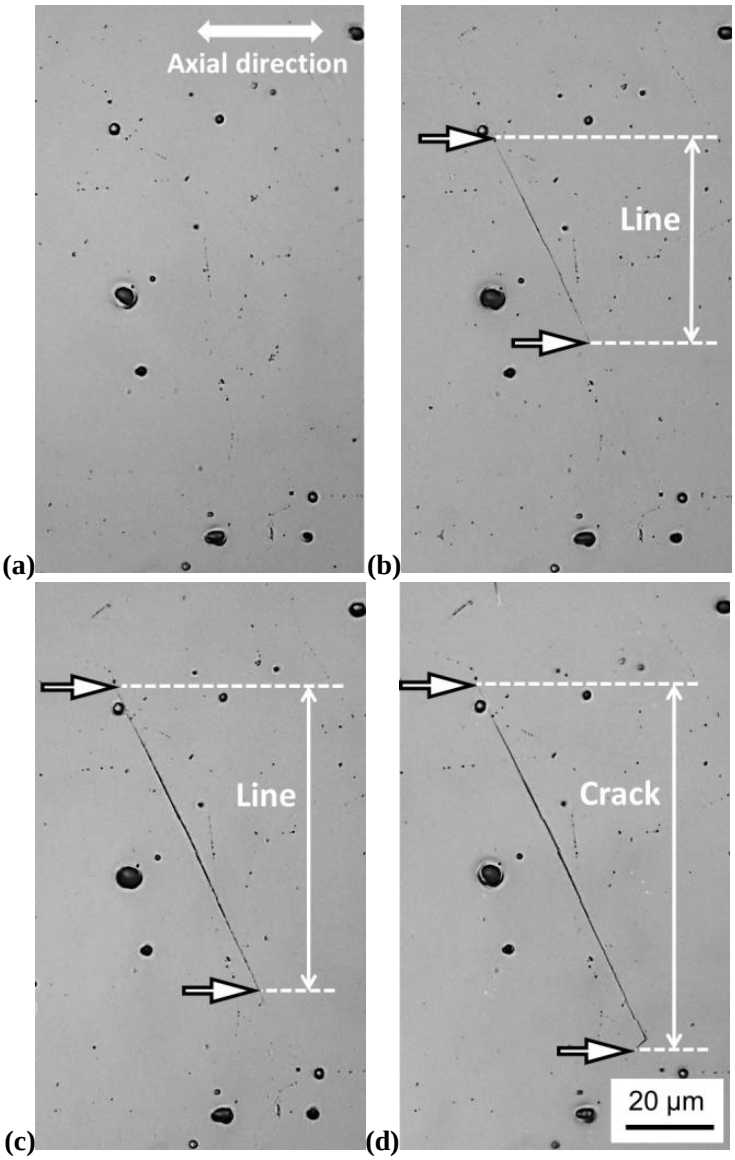

Fig. 11 Crack initiation behavior of hydrogen-charged specimen (the arrows indicate the crack tips) (σ_a = 260 MPa): (a) N = 0; (b) N = 1.0 × 10^6 cycles; (c) N = 2.0 × 10^6 cycles; (d) N = 3.0 × 10^6 cycles.

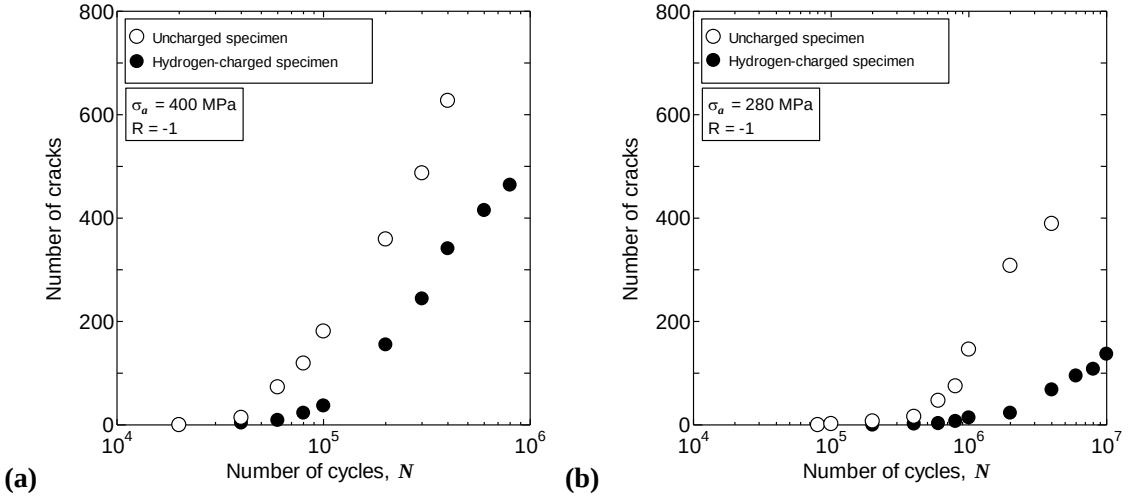

Fig. 12 *N*-*N* diagram of SUH660 steel at 400 and 280 MPa: (a) growth trend for number of cracks at 400 MPa; (b) growth trend for number of cracks at 280 MPa.

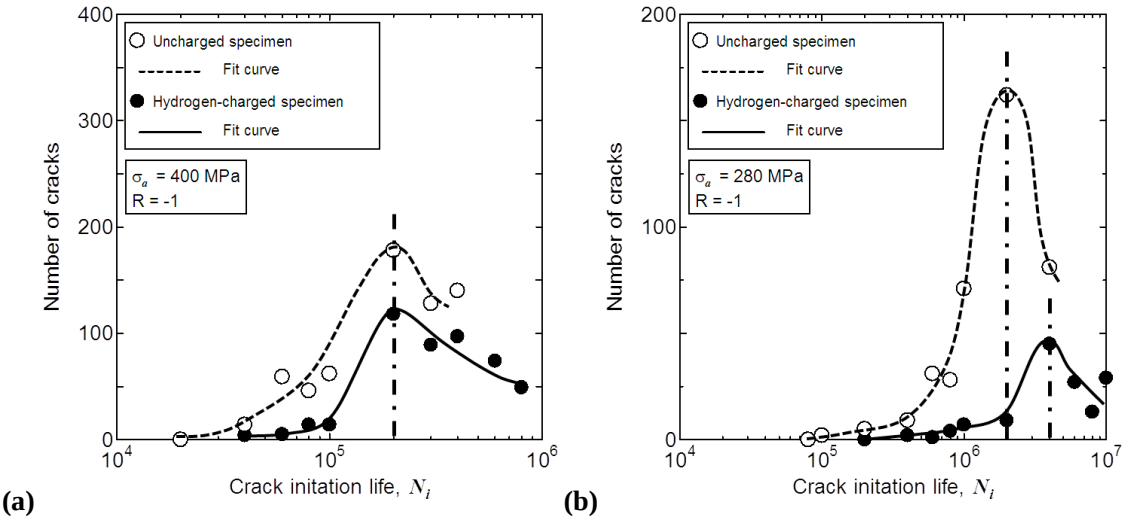

Fig. 13 Crack initiation life distribution at 400 and 280 MPa: (a) σ_a = 400 MPa; (b) σ_a = 280 MPa.

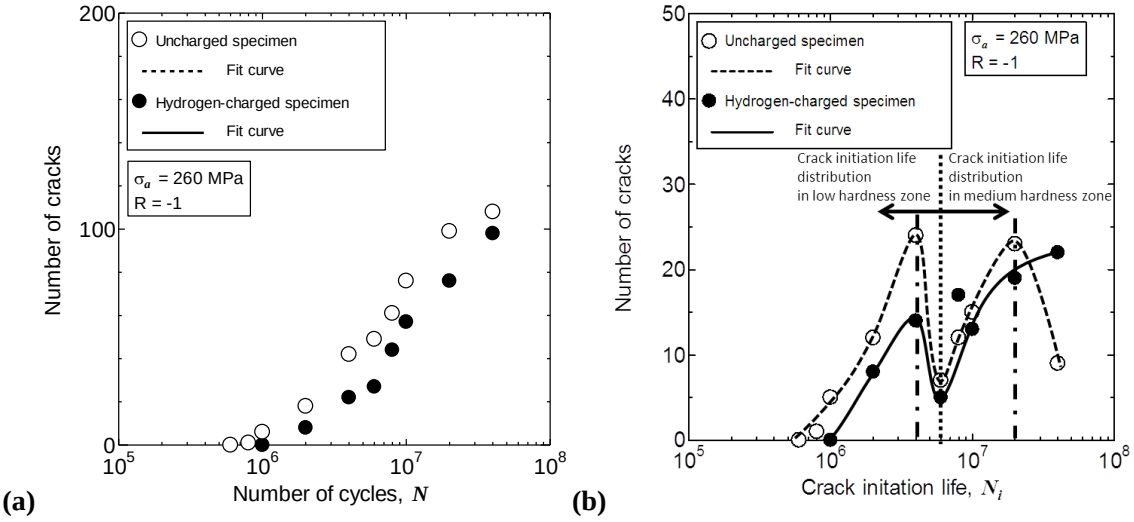

Fig. 14 *N*-*N* diagram and crack initiation life distribution at 260 MPa: (a) *N*-*N* diagram;

(b) crack initiation life distribution.

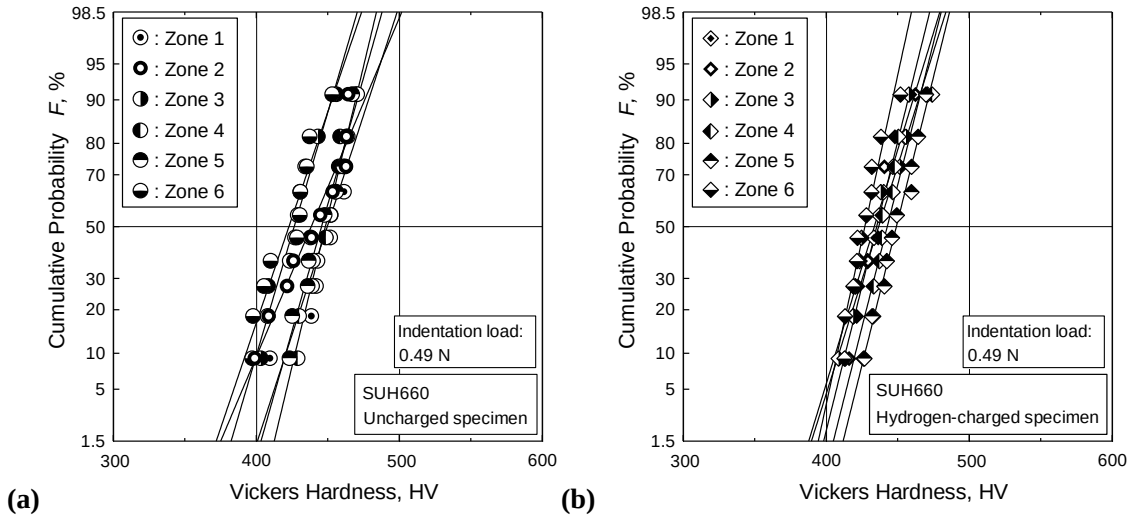

Fig. 15 Normal distribution of Vickers Hardness in SUH660 steel: (a) uncharged specimen;

(b) hydrogen-charged specimen.

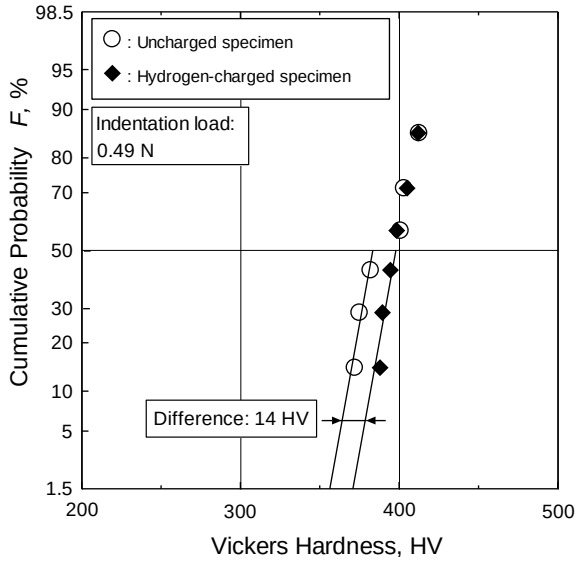

Fig. 16 Normal distribution of hardness in SUH660 steel.

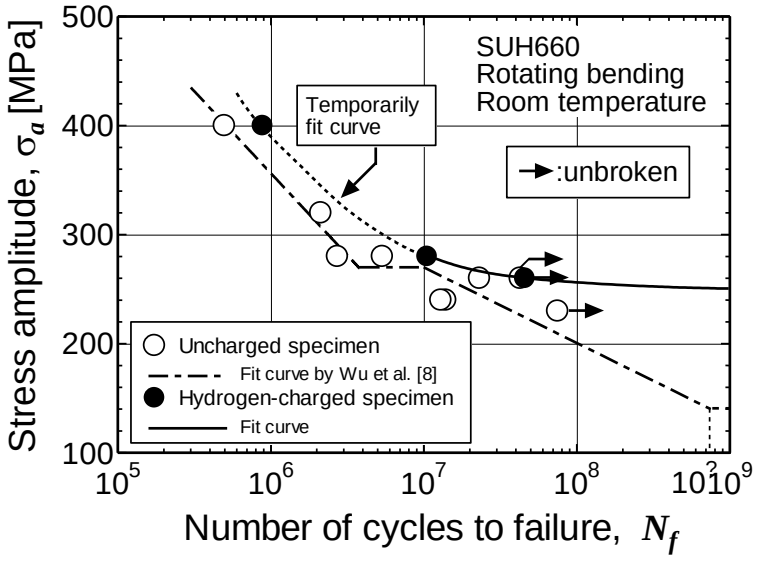

Fig. 17 *S-N* curve for hydrogen-charged SUH660 steel specimen.

CHAPTER 4 GENERAL CONCLUSIONS

The following results were obtained.

SUH660 steel exhibits two types of crack propagation behaviors: (1) cracks propagate monotonously at high stress amplitudes; (2) crack propagates intermittently at low stress amplitudes, wherein the crack is temporarily arrested, and after a large number of cycles, a new crack is initiated near the tip of the arrested crack and coalesces with it, leading to re-propagation of the temporarily arrested cracks. Based on the crack propagation behaviors, it is considered that the *S-N* diagram for SUH660 steel consists of two "fatigue limits". Fatigue Limit I is the fatigue strength at 10^7 cycles, which is not the true fatigue limit of SUH660 steel. Fatigue Limit II is the true fatigue limit and is considered to be the threshold of either PSB crack propagation or PSB crack initiation. The hardness variability of SUH660 steel results in low fatigue strength because fatigue cracks are initiated and propagate more easily in the low hardness zones. That causes SUH660 steel having a lower fatigue strength ratio than general steel. (Chapter 2.1)

To predict the fatigue limit of an inhomogeneous FCC metal, the difference between the intrinsic hardness and the Vickers hardness and the relationship between hardness and fatigue behavior were discussed. Vickers hardness and intrinsic hardness are both variable in an inhomogeneous FCC metal, and Vickers hardness is more variable in FCC metal than in BCC metal. The mean *HV* affect the level of residual stress leads to crack closure, and cracks initiate and propagate easily in the softest zone of an inhomogeneous FCC metal; therefore, the mean *HV* value of the softest zone can be used to predict the fatigue limit by Murakami's approach for an inhomogeneous FCC metal. Using the mean value of the Vickers hardness distribution in the softest

zone, the fatigue strength at 10^7 cycles of a plain specimen of SUH660 stainless steel, which is an inhomogeneous FCC metal, can be predicted by Murakami's approach. (Chapter 2.2)

The effect of pre-strain on the fatigue strength characteristics of an SUH660 plain specimen was investigated. The unusual fatigue behavior of crack growth acceleration due to pre-strain is observed at high stress amplitude, and we consider it is related to precipitate cutting. Based on the increases of crack growth rate due to pre-strain, we propose a dislocation accumulation model at the crack tip for precipitation-strengthened material. According to the model, the different fatigue characteristics for the pre-strained and non-strained specimens of SUH660 steel are caused by different locations of dislocation accumulation at the crack tip. The fatigue tests using buff –polished specimens were added to investigate the effect of local plastic deformation on fatigue behavior. Buff-polish treatment causes cutting of precipitates and residual stress in the work-hardened layer. At high stress amplitude loading, the cutting of precipitates accelerates crack growth in the specimen surface, and thus enhances crack growth inside of the specimen. At low stress amplitude loading, residual stress due to local plastic deformation enhances the plasticity-induced crack closure and the occurrence of temporary crack non-propagation. (Chapter 2.3)

All cracks were used instead of primary crack that leads fatigue failure to investigate the effect of internal hydrogen on the crack initiation of SUH660 steel. Hydrogen inhibits the number of crack initiation, but do not change the fatigue strength at 10^7 cycles. Above the fatigue strength at 10^7 cycles, hydrogen accelerates the increment of the crack initiation lives in low hardness zone with the stress decreasing. Below the fatigue strength at 10^7 cycles, the hydrogen accelerates the increment of the crack initiation lives in medium hardness zone with the stress decreasing. This is considered to be related with the hardness of hydrogen-charged specimen 14 *HV* higher than uncharged specimen

in medium and low hardness zones. The scatter of the new crack initiation lives is considered following the distribution of crack initiation life in medium hardness zone. Therefore, the fatigue life of hydrogen-charged specimen is much longer than uncharged specimen below the fatigue strength at 10^7 cycles. (Chapter 3)

ACKNOWLEDGEMENTS

The present work has been carried out during my tenure of a doctoral course at the Faculty of Engineering, Graduate school, Kyushu University under the supervision of *Prof.* **Hiroshi NOGUCHI**.

I would like to show my greatest appreciation to *Prof.* **Hiroshi NOGUCHI** and for his support and guidance in this research. I am deeply grateful to *Prof.* **Kaneaki TSUZAKI** and *Prof.* **Hiroyuki TODA** for the valuable guidance and advice. And I special wish to express my sincere gratitude to *Assoc. Prof.* **Shigeru HAMADA** for invaluable assistance, supports and guidance. Beside I am also grateful to *Research Fellow* **Yasuji ODA** for his helpful discussion.

I am indebted to all the members of Solid Mechanics Laboratory for their kind co-operation and assistance.

I received generous support from *Assoc. Prof.* **Yuuta AONO** of Kurume National College of Technology.

Finally, I would like to express my gratitude to my father, **Zhicheng WU**, and my mother, **Xiaoping LIN**, for their constant support and warm encouragement.